

**3-D ELECTRICAL RESISTIVITY TOMOGRAPHY FOR CLIFF STABILITY
ASSESSMENT AT POINTE DU HOC IN NORMANDY, FRANCE**

A Dissertation

by

SUWIMON UDPHUAY

Submitted to the Office of Graduate Studies of
Texas A&M University
in partial fulfillment of the requirements for the degree of

DOCTOR OF PHILOSOPHY

December 2008

Major Subject: Geophysics

**3-D ELECTRICAL RESISTIVITY TOMOGRAPHY FOR CLIFF STABILITY
ASSESSMENT AT POINTE DU HOC IN NORMANDY, FRANCE**

A Dissertation

by

SUWIMON UDPHUAY

Submitted to the Office of Graduate Studies of
Texas A&M University
in partial fulfillment of the requirements for the degree of

DOCTOR OF PHILOSOPHY

Approved by:

Chair of Committee,
Committee Members,

Mark E. Everett
Jean-Louis Briaud
Richard L. Carlson
Benchun Duan
Robert R. Warden
Andreas Kronenberg

Head of Department,

December 2008

Major Subject: Geophysics

ABSTRACT

3–D Electrical Resistivity Tomography for Cliff Stability Assessment at Pointe du Hoc
in Normandy, France. (December 2008)

Suwimon Udphuay, B.S., Chiang Mai University;

M.S., Chiang Mai University; M.S., Boise State University

Chair of Advisory Committee: Dr. Mark E. Everett

Pointe du Hoc overlooking the English Channel in Normandy, France was host to one of the most important military engagements of World War II. While the site is a valuable historic cultural resource, it is vulnerable to cliff collapses that already have endangered the observation post and Rudder’s command post. The observation post has been closed to visitors for some time due to safety concerns.

Geophysical techniques have been used increasingly in recent years for slope stability investigation purposes. The objective of this study is to apply advanced 3–D resistivity tomography toward a detailed site stability assessment with special attention to the two at-risk buildings. 3–D resistivity tomography datasets at Pointe du Hoc in the presence of extreme topography and dense cultural clutter have been successfully acquired, inverted, and interpreted. The cliff stability in the areas around the two at-risk buildings has been analyzed. A hazard assessment scheme has been designed in which regions of high resistivity are interpreted as zones of open, dry fractures with a moderate mass movement potential. Regions of low resistivity are zones of wet, clay-filled fractures with a high mass movement potential. The observation post tomography results indicate that the highest mass movement hazard appears to be associated with the marine caverns at the base of the cliff that are positioned at the point of strongest wave attack. These caverns likely occupy the future site of development of a sea arch which will definitely threaten the observation post building. A high probability of a soil wedge

failure is on the east-facing cliff edge close to the observation post that could damage or destroy the building. The mass movement potential at the Rudder's command post area is low to moderate. The greatest risk is associated with soil wedge failures at the top of the cliffs.

The resistivity geophysical data add great value to the natural geohazard assessment at Pointe du Hoc and constitute an integral component of an interdisciplinary approach to the problem of cultural resource preservation at the site. Geophysics is a non-invasive and relatively inexpensive technology that provides unique constraints which are unobtainable using traditional engineering geology methods for site characterization. However, the technology is difficult to master and the inherent limitations must be carefully understood to ensure a reliable geotechnical interpretation.

ACKNOWLEDGEMENTS

Foremost on the list of acknowledgements is my committee chair, Dr. Everett. I sincerely thank him for all of his support, guidance, and advice. Without him success would not be possible. In addition I am very grateful to my committee members, Prof. Warden, Dr. Briaud, Dr. Carlson, and Dr. Duan, for their valuable time and guidance through out the course of this research.

I appreciate Dr. Thomas Günther for his kind support and assistance setting up the inversion code and for helping through steps of the inversion.

Many thanks for several Texas A&M University faculty members and staff, especially those in the Department of Geology and Geophysics for their support and assistance through out my study.

Without the following people, field data acquisition would not have been possible: Carl Pierce, Dax Soule, Josh Gowen, and Jason Kurten.

Financial support through out my study at Texas A&M University is from the Ministry of Science and Technology, Royal Thai Government, the American Battle Monuments Commission, and the Department of Geology and Geophysics. Without their funding, I would not have made it this far.

Lastly, I greatly thank my parents, family members, and friends especially those from Texas A&M Thai Student Association for their encouragement and support.

TABLE OF CONTENTS

	Page
ABSTRACT	iii
ACKNOWLEDGEMENTS	v
TABLE OF CONTENTS	vi
LIST OF FIGURES.....	viii
LIST OF TABLES	xii
CHAPTER	
I INTRODUCTION.....	1
Literature Review	3
Study Area.....	9
Purposes of the Study.....	12
Study Scope.....	13
II SITE DESCRIPTION	18
Location.....	18
Site History.....	18
Geological Overview.....	21
Site Hydrogeology.....	28
Cliff Instability	29
III ELECTRICAL RESISTIVITY SURVEY PRINCIPLES.....	33
Fundamental Resistivity Theory	33
Multi-Electrode DC Resistivity Field Survey	37
Forward Modeling.....	42
Inversion Method	45
Electrical Resistivity of Earth Materials	48

CHAPTER	Page
IV DATA ACQUISITION AND ANALYSIS.....	55
Data Acquisition.....	55
Data Analysis	65
V DATA INTERPRETATION.....	81
Interpretation of 2006 Data	83
Interpretation of 2008 OP Data	87
Interpretation of 2008 RCP Data.....	101
VI DISCUSSION AND CONCLUSIONS.....	106
Discussion	106
Conclusions	111
REFERENCES	113
APPENDIX A	119
APPENDIX B	122
APPENDIX C	124
APPENDIX D.....	131
VITA	138

LIST OF FIGURES

FIGURE	Page
1.1 Outline map showing the location of Pointe du Hoc in Normandy, France	10
1.2 An aerial view of the Pointe du Hoc site	11
1.3 Rock collapses on the western side of the point	11
1.4 Basal wave-cut caverns at the western side of the point under the observation post	12
1.5 Groundwater cliff seepage	13
2.1 Location of Pointe du Hoc in Normandy, France	19
2.2 The battlefield landscape of Pointe du Hoc	20
2.3 Photos of the two at-risk buildings.....	21
2.4 Jurassic outcrops in the region between the Paris Basin and the Armorican Massif	24
2.5 The middle Jurassic succession of the Normandy reference section	25
2.6 Pointe du Hoc middle Jurassic formations showing the approximate interface between the lower Bathonian Marnes du Port formation and the middle Bathonian Calcaires de St. Pierre du Mont.	26
2.7 Exposed by a recent soil-wedge failure is the Quaternary soil cover at Pointe du Hoc, underlain by layered calcarenite and marls of possible Plio-Pleistocene origin.....	27
2.8 Pointe du Hoc cliff stratigraphy based on borehole information acquired by Texas A&M geotechnical team	27
2.9 The leeward beach east of Pointe du Hoc	29

FIGURE	Page
2.10 Groundwater seepage from cliff face at the top of the Marnes de Port marl	30
2.11 Rock collapses and marine basal notching	32
3.1 Electrical current flow diagrams	35
3.2 Common arrays used in resistivity surveys and their geometric factors....	37
3.3 The arrangement of electrodes for a 2–D electrical survey and the sequence of measurements used to build up a pseudosection	39
3.4 The arrangement of the electrodes for a conventional 3–D survey.....	41
3.5 Three dimensional grids used for dc resistivity forward modeling.....	43
3.6 The three meshes used in the inversion algorithm.	46
3.7 Typical ranges of electrical resistivities of Earth materials	50
3.8 Classification of intergranular texture in carbonate rocks.....	52
3.9 Classification of vuggy texture in carbonate rocks	53
4.1 Equipment set up	56
4.2 Cliffside electrode installation	57
4.3 Pointe du Hoc reconnaissance-phase 2006 geophysical site map showing approximate locations of topside resistivity lines, cliffside resistivity lines and observation post resistivity lines, and borehole locations	59
4.4 Assumed 4:1 slope geometry of the 2006 electrodes installed in the cliff face	61
4.5 Total-station temporary control point network used for locating electrode positions in the 2008 data acquisition phase	63
4.6 Pointe du Hoc 2008 OP geophysical site map showing locations of topside resistivity lines , cliffside resistivity lines and other lines that required roped access at the OP area.....	64

FIGURE	Page
4.7 Pointe du Hoc 2008 RCP geophysical site map showing locations of topside resistivity lines, cliffside resistivity lines and other lines that required roped access at the RCP area	65
4.8 Apparent resistivity pseudosections from Schlumberger and dipole-dipole electrode configuration.....	67
4.9 Resistivity pseudosections and 2–D inversion section with extreme topography of CLF–1 profile using AGI <i>EarthImager 2D</i> inversion software	68
4.10 Resistivity pseudosections and 2–D inversion section with extreme topography of CLF–1 profile using BERT 2–D inversion program	69
4.11 Resistivity pseudosections and 2–D inversion section of the 2008 dataset line OP–9 using BERT 2–D inversion program and plotting by postBERT2d MATLAB package	73
4.12 Laser scanning cloud points and electrode points	76
4.13 3–D surface topographic model and mesh for 2006 dataset	78
4.14 3–D surface topographic model and mesh for 2008 OP dataset	78
4.15 3–D surface topographic model and mesh for 2008 RCP dataset	79
5.1 Photos of a fractured calcarenite core segment from the Calcaire de St. Pierre du Mont formation of Pointe du Hoc.....	82
5.2 The 3–D resistivity tomogram produced from the 2006 dataset	84
5.3 Top view of the 2006 3–D resistivity tomogram with resistivity lines on the site aerial photo	85
5.4 Fence diagram showing a perspective assembly of all 2–D subsurface distributions based on complete set of 2–D resistivity lines of the 2006 dataset.....	87
5.5 2–D resistivity inversion profiles of some topside lines of 2006 dataset...	88
5.6 Cliffside 2–D resistivity inversion profiles of 2006 dataset.....	89

FIGURE	Page
5.7 The 3–D resistivity tomogram produced from the 2008 OP dataset, viewed from the northeast.....	90
5.8 The 3–D resistivity tomogram produced from the 2008 OP dataset, viewed from the northwest	91
5.9 Top view of the 2008 OP 3–D resistivity tomogram with resistivity lines on the OP aerial photo.....	92
5.10 The 2008 OP resistivity tomogram combined with terrestrial laser scanning data	95
5.11 Formation of a sea arch and stack	96
5.12 Horizontal slices through the 2008 OP 3–D resistivity tomogram	98
5.13 Vertical slices through the 2008 OP tomogram	99
5.14 The 3–D resistivity tomogram produced from the 2008 RCP dataset	102
5.15 Top view of the 2008 RCP 3-D tomogram with resistivity lines on the RCP aerial photo	103
5.16 Vertical slices through the 2008 RCP tomogram.....	104
5.17 Horizontal slices through the 2008 RCP 3–D resistivity tomogram.....	105

LIST OF TABLES

TABLE	Page
3.1 Cementation exponent m values as a function of carbonate porosity type, Pointe du Hoc sequence	54
4.1 Acquisition geometry for 2006 reconnaissance-phase dataset.....	60
4.2 X-y boundary and number of terrain points used for digital topographic models	76
4.3 Number of parameters used for full 3-D inversion in BERT	80
5.1 Resistivity tomography interpretation scheme	83

CHAPTER I

INTRODUCTION

Landslides including cliff collapses and other mass movements affect all geological materials and on steep slopes can constitute a significant geohazard. Mass movements are triggered by diverse causes such as heavy rains, marine wave attack at coastal locations, freeze–thaw cycles, soil creep, tectonic activity including earthquakes, and human activities such as water and vegetation management, construction and excavation, traffic, and loud noises such as explosions. Naturally occurring mass movements in many countries are a critical problem in both financial and human terms, both directly by death and damage to property and indirectly by disruption of transport and communications networks. Such a problem often affects civil engineering structures and consequently causes an expensive remediation cost.

A detailed geohazard assessment may require a large area of investigation and is best carried out using a multidisciplinary approach incorporating geophysical, geological and geomorphological mapping, and geotechnical techniques. The latter techniques, which typically include boreholes, penetration tests (when possible) and trenching, allow a detailed geological description and failure mechanism of the material. The geotechnical data can be used to define vertical boundary of a possible detachment and the parameters required for a slope stability analysis. These techniques however provide only restricted spatial information since the borehole provides only a single-point data source and their use is often limited by the difficulty and expense of drilling onto a steep and unstable slope.

Geophysical techniques have been used increasingly in recent years although relatively little of this work for slope stability investigation purposes has been documented in the peer–reviewed scientific literature. Advantages of geophysical techniques are that they are flexible, readily deployable on slopes, non–invasive, and

This dissertation follows the style of Geophysics.

provide spatially continuous parameters that are required for assessing landslide potential and activity. Geophysical techniques are particularly effective at the reconnaissance stage after a large landslide has occurred (McCann and Forster, 1990) since they provide rapid wide-area subsurface assessment. The recent emergence of 2-D and 3-D geophysical imaging techniques and the efforts of manufacturers to provide reliable and portable equipment have dramatically increased the interest of geophysical techniques for landslide applications. Geophysical techniques now are established tools, along with conventional geological and geotechnical techniques, to provide a reliable mass-movement potential interpretation. The research in this dissertation describes the application of a specific geophysical methodology, multi-electrode resistivity tomographic imaging, to a multidisciplinary cliff stabilization project at Pointe du Hoc.

The D-Day invasion historic site at Pointe du Hoc overlooking the English Channel in Normandy, France was host to one of the most important military engagements of World War II (WWII). Its significance is marked by the bravery of the 2nd Ranger Battalion led by Lieutenant Colonel James Earl Rudder who scaled the ~30 m cliffs to disable one of the strongest German defensive positions along the Atlantikwall. That effort and its subsequent aid to the overall Allied success on D-Day turned the tide of the war and have resulted in Pointe du Hoc becoming one of the most popular WWII tourist sites in France.

While the site is a valuable historic cultural resource, it is vulnerable to mass movements, e.g. cliff collapses that already have endangered the forward observation post building. The U.S. Ranger memorial stands atop the observation post. This structure, located perilously close to the cliff's edge near the point, is the most significant cultural object at Pointe du Hoc. A second important structure is the eastern anti-aircraft building, which became Col. Rudder's command post in the hours and days following the invasion. The anti-aircraft east building is located on the cliff edge about 200 m east of the observation post. The observation post and the memorial have been closed to tourists for some time due to safety concerns. As a result, a Texas A&M University multidisciplinary team of historical architects (led by Prof. Robert Warden),

geotechnical engineers (led by Prof. Jean-Louis Briaud), and geophysicists (led by Prof. Mark Everett) was tasked by the American Battle Monuments Commission (ABMC) to perform a cliff stability study. The overall goal of the study is to investigate the mass movement potential as it might impact the observation post and anti-aircraft east buildings. A further study objective is to suggest possible remediation or hazard-reduction schemes.

A steeply sloping surface where elevated land meets the shoreline is referred to as a coastal cliff. Coastal cliffs are a geomorphic feature of first-order significance, occurring along about 80 percent of the world's shorelines (Emery and Kuhn, 1982). Like almost all landforms, modern coastal cliffs are continually acted upon by a broad assortment of offshore and terrestrial processes that cause them to change form and location through time e.g. coastal cliff retreat (Hampton et al., 2004). Cliff retreat has caused damage to structures located along a coastal cliff. Pointe du Hoc is among other coastal cliffs, that has been jeopardized by cliff collapses and the important WWII historical structures sitting on top of the cliffs can be naturally destroyed if they are without protection.

LITERATURE REVIEW

Coastal Cliff Study

The evolution of a coastal cliff from stability toward failure depends on the spatial variability of the rock mass (lithology, fracture pattern), and hydrogeological processes acting within the rock mass (degree of water saturation, water movement). External subaerial and marine factors, along with groundwater infiltration, lead to the enlargement of pre-existing fractures (originating from tectonic stress relief and long-term climate changes) and the subsequent deterioration of the rock material. Groundwater interactions, in particular, result in chemical alteration via carbonate dissolution. Physical breakdown through freeze-thaw or salt crystallization can also be significant (Duperret et al., 2005).

A European scientific project, ROCC (Risk Of Cliff Collapse) was launched in order to identify the critical parameters leading to coastal cliff collapses in chalk weak rock, and to evaluate the impact of those parameters and their interaction in such rock mass movements. The ROCC project is focused on Upper Normandy and Picardy regions in France and on East- Sussex in the UK. The chalk cliffs exposed along either side of the English Channel have suffered numerous collapses. Long term erosion rates of coastal chalk cliffs of the English Channel are roughly similar in France and UK, with 0.23 m/year on the French coast and 0.27 m/year on the East Sussex coast. However, the erosion is not constant over time, but occurs by sudden collapses that may induce cliff retreats 10-20 m deep in one event (Duperret et al., 2002). Although the ROCC project has a limited applicability to our project since the cliffs at Pointe du Hoc are not chalk but they are a mixed siliciclastic-carbonate lithology, it provides useful relevant assessment of cliff stability study.

In the Duperret et al. (2004) report, more than 50 significant collapses were recorded along 120 km of the French chalk coastline located in Upper-Normandy and Picardy over a period from October 1998 to September 2001. They suggest that groundwater within the poorly fractured chalk is the major contributor of cliff collapses. Heavy rainfall is a key collapse triggering factor. They also conclude that marine parameters which produce basal notching on the cliffs appear to play an important role in the cliff collapses. This is also supported by the study of Brossard and Duperret (2004) which reports that the marine erosion of the shore platform does not appear to be the main cause of the Normandy coastal cliff erosion. Nevertheless, a large number of authors (e.g. Emery and Kuhn, 1982; and Sunamara 1982) propose that marine storm-surge attack at the cliff base is responsible for undercutting the cliff, establishing the necessary conditions for subsequent soil wedge failures and other kinds of mass movements originating at the top of the cliff.

The chalk cliff failure mechanism discussed above is similar to the failure mechanism of the Point du Hoc cliffs as suggested by Briaud et al. (2007). At Pointe du Hoc heavy rains can cause wedge failures in the top soil cover. The rainwater, especially

in the exposed scars, readily infiltrates through joint networks in the underlying strata, enlarging fractures via dissolution and emerging as seeps in the cliff face. The percolating fresh water also decreases the overall rock mass strength, causing rock blocks to behave individually rather than as a single mechanically coherent body. Furthermore, extended vertical cracks can develop due to frost heave or horizontal decompression forces associated with mass movement. Once the cliff has been structurally weakened by the aforementioned processes, wave action especially during storms can remove the rock blocks creating caverns at the base of the cliffs. The formation and enlargement of caverns eventually undermines the cliffs, creating a critical tensile stress that causes additional wedge failures at the cliff top.

In the general case of landslide stability analysis, Friedel et al. (2006) point out that rainfall-induced landslides are common in areas with slope angles steeper than the friction angle of the soil. Such slopes are only stable within a certain range of water saturation within which the effect of suction creates an apparent cohesion between the soil particles and enhances the shear resistance. Suction and shear resistance are reduced significantly if the water saturation rises above a critical value. Especially after heavy rainfalls, water saturation may exceed the critical limit in certain parts of the slope, initiating local failure leading to a landslide or debris flow. This discussion can apply to the topside soil wedge failures occurring at Pointe du Hoc but probably not to the larger rockfalls which follow a toppling mechanism triggered by basal cliff undercutting, as discussed by Briaud et al. (2007).

Geophysics for Slope Stability

Geophysics has been used in the investigation of slope stability and landslides for many years (Bogoslovsky and Ogilvy, 1977; McCann and Forster, 1990; Bruno and Marillier, 2000; Gallipoli et al., 2000; Hack, 2000; Mauritsch et al., 2000; Suzuki and Higashi, 2001; Bichler et al., 2004; Perrone et al., 2004; Lapenna et al., 2005; Meric et al., 2005; Drahur et al., 2006; Friedel et al., 2006; Godio, 2006; Jongmans and Garambois 2007). Geophysical methods applied to slope stability analysis and landslide

areas have been reviewed by McCann and Forster (1990), Hack (2000), and Jongmans and Garambois (2007).

McCann and Foster (1990), Hack (2000), and Jongmans and Garambois (2007) stated that in slope stability analyses, geophysical methods can be cost effective means to determine the internal structure and/or the properties of the soil or rock mass materials where boreholes or trenches are limited, not possible or impractical. The methods that are most frequently used in slope stability investigations are seismic, electrical resistivity; ground penetrating radar and gravity methods. They also discussed that none of the geophysical methods is better than another method. The success with which a method is applied fully depends on the circumstances at the site and on the subsurface materials.

Suzuki and Higashi (2001) over several days monitored using surface resistivity tomography the vadose-zone flow of groundwater after heavy rains at a hazardous landslide-slope area. They carried out tomography with electrodes positioned both on a surface profile and within a borehole. They used a smoothness-constrained least-squares 2-D inversion technique (Sasaki, 1992). Their results suggest a connection between temporal resistivity changes and infiltration of rainwater. In particular, a pronounced low-resistivity anomaly suggested a complicated groundwater flow pattern caused by heavy rain infiltration into the vadose zone. In addition, they discovered a relationship between 2-D resistivity and rainfall which depends on the permeability of the layer and the number of water infiltration events.

Bichler et al. (2004) applied electrical resistivity tomography (ERT) technique combined with other geophysical approaches for subsurface mapping in a landslide area. They collected data along several orthogonal profiles using a multi-electrode system. They identified electrical contrasts which provided information on the geometry of strata and depth extent of the mass movement. By combining various geophysical datasets, they were able to more certainly interpret the 3-D subsurface structure of the landslide.

Perrone et al. (2004) and Lapenna et al. (2005) carried out ERT and self-potential surveys to gain better knowledge of landslides in southern Italy. Several ERT

profiles were acquired using a multi-electrode system. Drahor et al. (2006) report another successful use of the multi-electrode ERT technique for investigation of landslides. The geometry and certain physical properties of landslide material as well as the boundaries of the water saturated zone were determined by the ERT.

Friedel et al. (2006) report an investigation of a slope endangered by rainfall-induced landslides using resistivity tomography and geotechnical testing. They applied high-resolution 2-D and 3-D ERT to derive a detailed subsurface image, which was validated by direct penetration tests and boreholes. The combined ERT and geotechnical survey helped to optimize the design of the monitoring experiment and may be used as a guideline for the investigation of similar slope conditions elsewhere.

Electrical Resistivity Tomography Methods

The ERT imaging technique, as previously mentioned, has recently been applied to investigate soil and groundwater conditions for slope stability assessments. The ERT technique provides high spatial resolution capability, relatively fast and non-invasive data acquisition, and low cost. Furthermore, the development of innovative and robust inversion methods incorporating topography (Loke and Barker, 1996; Günther et al., 2006) permit accurate data interpretation for resolving complex geological problems, such as defining aspects of hidden underground structures (i.e. fractures, water accumulations, etc.) or studying the spatiotemporal evolution of groundwater flow relative to landslide phenomena.

The ERT method is the preferred geophysical technique for evaluating cliff stability at Pointe du Hoc since it responds well to the bulk hydrogeological parameters of rock formations. The method was successfully used by Ritzi and Andsolek (1992) to evaluate the principal directions of groundwater flow in a fractured carbonate rock formation. Skinner and Heinson (2004) confirmed that resistivity methods can be used to determine the major hydraulic pathways in fractured rocks. Leucci (2007) detected fractures in soft calcarenite cliffs in Italy by combining resistivity tomography with seismic refraction and ground-penetrating radar (GPR). Deparis et al. (2008) combined

laser scanning, resistivity tomography and GPR to study the stability of Mesozoic limestone cliffs in the French Alps. The GPR was found to out-perform resistivity tomography for mapping subsurface fractures in that hard-rock environment. At Pointe du Hoc, GPR was used during the 2006 field season but this technology did not provide the required depth of penetration (~20–25 m) through the soft, conductive silty-clay overburden.

Bichler et al. (2004), Perrone et al. (2004), Lapenna et al. (2005), and Drahor et al. (2006) used the ERT technique, based on smoothness-constrained least-squares inversion, developed by Loke and Barker (1996a and 1996b). The algorithm is based on the Jacobian matrix of partial derivative values of apparent resistivity for a homogeneous earth model for the first iteration, followed by a quasi-Newton optimization technique to estimate the Jacobian matrix in subsequent iterations. The subsurface model comprises several layers with each layer subdivided into a number of rectangular blocks, the number of which corresponds to the number of measured data. The optimization iteratively adjusts the resistivity model to minimize the root mean-squared (rms) error between the calculated and measured apparent resistivity values. Although Loke and Barker (1996) show that their inversion algorithm is much faster than a conventional least-squares method, their technique is limited to block-oriented rectangular meshes and the electrodes of the 3-D resistivity survey must be located on the nodes of a rectilinear grid.

Günther et al. (2006) have developed a novel 3-D inversion of dc resistivity data incorporating arbitrary surface topography. The approach involves a triple-grid inversion based on unstructured tetrahedral meshes and a finite-element forward calculation (Rüker et al., 2006). A Gauss-Newton algorithm with inexact line search is used to fit the data within error bounds. A global regularization scheme using smoothness constraints is applied. The regularization parameter which trades off between data misfit and model roughness is determined by an L-curve method and evaluated by the discrepancy principle. A least-squares technique is applied to efficiently solve the inverse subproblem. A stable solution is typically achieved after a

small number of iterations. The computer run time is greatly reduced by a singularity removal technique and use of fast, direct matrix solvers. Gunther et al. (2006) claim that their approach provides a resolution-dependent parameterization, which further saves computing time and memory. The approach is especially powerful for resistivity surveys with steep topography and for large-scale problems.

STUDY AREA

The study area is at Pointe du Hoc which is located on a cliff-top overlooking the English Channel along the coast of Normandy in the north of France (Figure 1.1). The site preserves many original aspects of the Atlantikwall fortifications built by the German during the WWII (Hakim, 1995; Kaufmann and Kaufmann, 2003). Two key examples of those fortifications are the observation post building located at the most northern part of the plateau; this is the closest building to the point; and the anti-aircraft building located about 200 m east of the observation post. Both buildings are perched perilously close, within a few m, to the cliff edge (Figure 1.2). The site also contains an impressive number of bomb craters which can be seen from the aerial photo in Figure 1.2. The cliff height varies from ~20 to ~30 m along the beach; it is ~21 m at the observation post location. Tentative cliff-retreat calculations based on photographs taken over the last 64 years (1944–2006) indicate that, at the most aggressive location, the Pointe du Hoc site has experienced ~10 m of erosion due to collapses. The long-term average cliff retreat is ~0.16 m/year (Briaud et. al, 2007).

Evidence of recent rock failures appearing as piles of rockfalls on the beach is observed, mainly on the west side of the cliff point (Figure 1.3). Fresh scars indicate recent soil wedge failures near the top of the cliff. Severe cliff basal erosion showing as wave-cut caverns is also observed especially on the western side of the point close to the sea stack (Figure 1.4). This may reflect the fact that the predominant wave and wind direction in the English Channel is from the west. The eastern side of the point is relatively protected from the Atlantic storms and consequently a significant gravel beach shingle has accumulated. There are significant basal caverns observed also on the

eastern side that are covered, during quiet periods, by the gravel shingle. However, large storms move the gravel offshore and expose these caverns. Note that Figure 1.2 was taken during a quiet period such that significant gravel has accumulated on the east side.

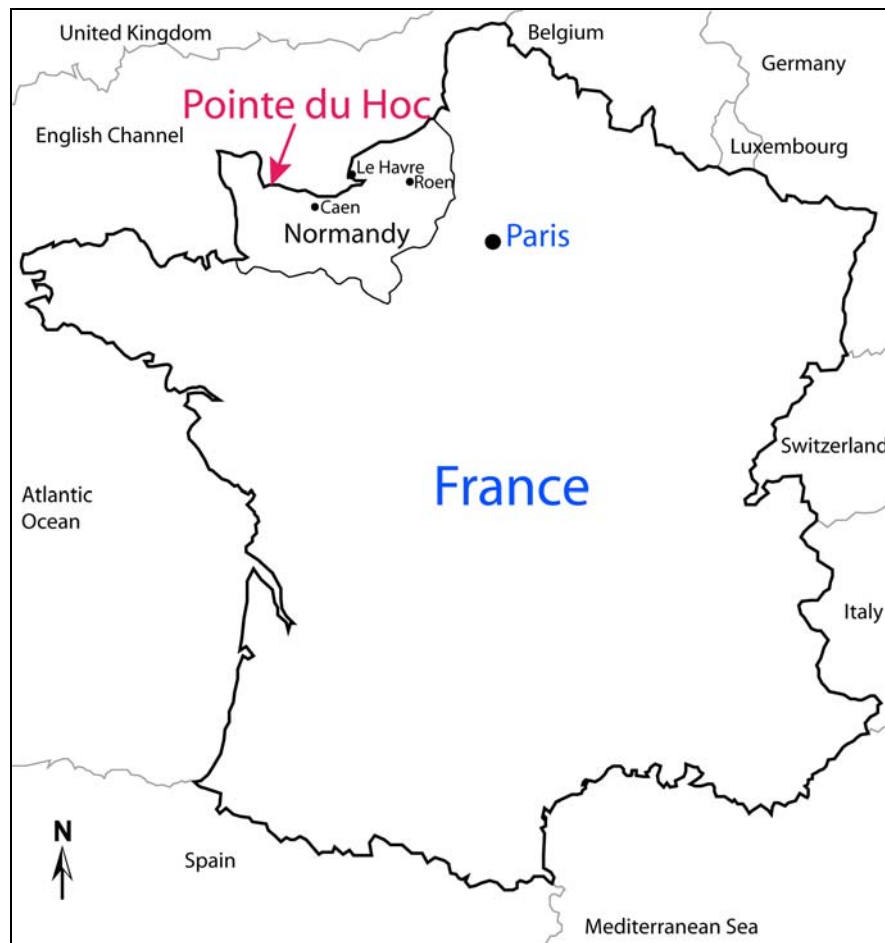


Figure 1.1. Outline map showing the location of Pointe du Hoc in Normandy, France.

Groundwater seepage from the cliff face is observed in several places especially along the western side of the point at a level of ~2–3 m above the cliff base or ~18–20 m from the top of the cliff. The groundwater seepage provides evidence of the hydraulic properties of the cliffs. Limestone dissolution enlarges the cracks, which were likely



Figure 1.2. An aerial view of the Pointe du Hoc site. Notice the extensive gravel shingle that accumulates on the east side during quiet periods between large storms.



Figure 1.3. Rock collapses on the western side of the point.



Figure 1.4. Basal wave-cut caverns at the western side of the point under the observation post.

formed in association with Mesozoic tectonic stress relief. Locations where groundwater seeps out of the cliff face are typically indicated by enhanced vegetation growth and areas of mineral precipitation. Figure 1.5 shows some of these areas.

PURPOSES OF THE STUDY

The main objective of the geophysical investigation at Pointe du Hoc is to apply an advanced resistivity tomographic imaging approach for mapping major subsurface fracture zones and void spaces that could indicate geological instability linked to possible accumulations and pathways of groundwater. Heavy rain causes wedge slope failures in Pointe du Hoc top soil cover. The rock mass at Pointe du Hoc cliffs is naturally fractured and well-drained. During heavy rainfalls, the water readily percolates through the joints network in the rock mass cleaning and weakening the soil-filled rock joints thereby tends to exfoliate sheets of the rock mass and weakens its strength. Once the cliff has been structurally weakened by groundwater processes, wave action especially during storms can dislodge the rock blocks enlarging caverns at the base of the cliffs. The caverns eventually undermine the cliffs, triggering rock falls and additional wedge failures at the cliff top.



Figure 1.5. Groundwater cliff seepage.

The geophysical survey was performed to provide a detailed site stability assessment with special attention to the most significant buildings, the observation post and the eastern anti-aircraft buildings, which are jeopardized by the potential of cliff collapse. The geophysical information obtained is essential to recommend geotechnical remediation options for stabilizing the at-risk buildings and their immediate environment, such that safe access can be provided for visitors.

STUDY SCOPE

Based on the main purpose and review of the state of the art in geophysical slope stability investigations, the ERT technique was selected as the most appropriate geophysical tool for contribution to the cliff stability study at Pointe du Hoc. The methodology comprising ERT data acquisition, analysis, and interpretation incorporating geological and geotechnical information is described as follows.

Data Acquisition

The geophysical field work was divided into 2006 reconnaissance and a 2008 high-resolution phases. Many of the data acquisition procedures such as number of data coverage, survey lines position by total-station navigation and cliff access were greatly improved by the 2008 field data acquisition phase.

2006 Phase

In June 2006, a reconnaissance ERT acquisition survey over the Pointe du Hoc area was performed using the multi-electrode resistivity system SuperSting R8/IP manufactured by Advanced Geosciences, Inc. (AGI). Ten electrical resistivity profiles on the top side of the site, two profiles at the observation post building area, and six profiles draped over the cliff edge with significant portions extending onto the near-vertical cliff face, were collected. Using a total station, the horizontal position and elevation of the electrodes along each profile was found using a land-surveying resection procedure involving known landmarks whose coordinates had been previously established. However, the elevations of the electrodes staked directly on the cliff face could not be determined due to lack of line-of-sight from the cliff top. Note that the installation of the electrodes on the cliff face requires roped access, which proved to be quite challenging from a logistics standpoint.

The ERT dataset acquired at the reconnaissance stage, combining all 2-D profiles, generated an overall 3-D resistivity tomogram of the site, which was the goal of the 2006 reconnaissance survey. However, the 3-D tomogram provides little high-resolution information of the detailed subsurface resistivity near the critical at-risk buildings since the spacing between 2-D resistivity lines is too coarse. This became the focus of the 2008 high-resolution survey.

2008 Phase

Therefore, based on experience gathered during the 2006 reconnaissance data acquisition stage, a comprehensive suite of high resolution measurements in March 2008

was acquired at the site. At this time the focus efforts was to the vicinities of the observation post and the eastern anti-aircraft buildings (Figure 1.2) which are located closest to the cliff edge and are at the most risk from future cliff collapses. The high-resolution 2008 survey was designed after discussion with the ABMC in which they indicated the critical need for high-resolution subsurface information near the two at-risk buildings.

Two high-resolution resistivity surveys were acquired in 2008 in the vicinities of the observation post and Rudder's command post (eastern anti-aircraft building), respectively. The resistivity data were acquired using the same SuperSting multi-electrode system with the same strategy placing electrodes both on the top-and-cliff side of the cliff but at substantially higher line-density than the 2006 data set. For the observation post area, 37 resistivity lines were acquired, of which 32 are topside lines and five are cliffside lines that required roped access. For the Rudder's command post area, 14 resistivity profiles were acquired, of which six are topside lines and eight are cliffside lines that required roped access.

The total station surveying instrument was again used to determine electrode elevations and horizontal locations, but to a much greater precision than was accomplished during the 2006 campaign. In addition, electrode (including the ones on the cliff face) topography and surrounding area positions were obtained using laser scanning data which were acquired by the historical study team. High-accuracy ERT 3-D tomograms based on the apparent resistivity measurements combined with the precise topographic information, were then produced.

2-D Data Analysis

The 2006 2-D resistivity profiles were originally processed and inverted using the *EarthImager 2D* software from AGI. The program is based on an inversion algorithm described by Loke and Barker (1996) and Yang (1999). The program works well for the top-side electrode profiles but struggles with the electrode profiles draped over the cliff edge, due to the extreme topography. The program treats the cliff-face in

the same manner as the surface topography, using a single terrain file, and hence the forward modeling finite–element mesh becomes heavily distorted at the cliff face.

A preferable inversion method permitting electrodes to be positioned atop arbitrary topographic variations has been developed by Günther et al. (2006). The program works well with the extreme topography of the cliffs at Pointe du Hoc. The program provides a powerful solution to a challenging geophysical problem, is open source, and available free of charge for academic research. Consequently, this inversion program was chosen to handle the top-side and the extreme terrain of the cliffside resistivity profiles for both data sets of 2006 and 2008.

3–D Data Analysis

Combining all 2–D profiles of each data sets, three 3–D resistivity data sets (2006, 2008 Observation Post, and 2008 Rudder’s Command Post datasets) were generated. The 3–D resistivity data plus the topographic data were then ready for the data inversion.

Due to the severe limitation of the conventional 3–D resistivity survey that electrodes have to be located on a regular perpendicular grid, the commercial EarthImager 3–D or Res3DInv inversion software packages could not be used for the Pointe du Hoc datasets since the electrode lines were located in an irregular pattern. Fortunately, the 3–D inversion program under active developed by Günther et al. (2006) available at <http://resistivity.net> can work very well with our data. This open–source software was use to invert our data and produce 3–D resistivity tomograms for the site. 3–D fence diagrams and depth slices can be constructed from the tomogram to present interior views of subsurface resistivity of the site.

Data Interpretation

2–D and 3–D electrical resistivity tomograms can be used as detailed subsurface images if data are acquired at sufficiently high spatial resolution. A geophysical image, by itself without other relevant information such as geological and geotechnical

information, is generally not sufficient to provide a realistic subsurface geological model for the site (Friedel et al. 2006). In this study therefore other information available at the site (borehole, geological, historical, and laser scanning data) was incorporated for interpreting the tomograms in order to obtain reliable information concerning site geological stability.

In this dissertation, further details of the site geology and description, and the resistivity method will be explained in Chapter II and III, respectively. In Chapter IV the data acquisition and analysis will be described. The data interpretation based on the resistivity tomograms will be explained in Chapter V. Finally, discussion and conclusions will be presented in Chapter VI.

CHAPTER II

SITE DESCRIPTION

In this chapter, a few details of the site at Pointe du Hoc including its location, history, geological overview, and hydrogeology are described. The present cliff stability of the site is also discussed at the end of the chapter.

LOCATION

Pointe du Hoc in western Normandy, France is located a few km to the east of the town of Grandcamp–Maisy near the communes of Cricqueville–en–Bessin and Saint–Pierre du Mont as shown in Figure 1.1 and 2.1. It lies ~ 12 km to the west of Normandy American Cemetery and Memorial, which overlooks Omaha Beach along the English Channel coastline.

SITE HISTORY

Pointe du Hoc provided the setting for one of the most important World War II battles when on D–Day, June 6, 1944, the US 2nd Ranger Battalion scaled its ~30 m cliffs to reach and destroy one of the strongest German defensive positions along Hitler’s formidable Atlantikwall. The Rangers were led by Lieutenant Colonel James Earl Rudder, later to become a president of Texas A&M University. Pointe du Hoc is strategically located between Utah and Omaha Beaches along the Normandy coast, and therefore an ideal centerpiece of the Allied plan of attack on D–Day. The Germans, aware of its importance in protecting the Atlantikwall, relied on its location high above the English Channel for protection from Allied attack by sea. German observations and firepower were directed seaward but their primary endeavors for protecting the site were directed inland. This philosophy led in part to the American decision to attack Pointe du Hoc by scaling the cliffs. That critical decision and the subsequent unfolding of the events in the days, weeks, and months after D–Day resulted in the transformation of

Pointe du Hoc from a standard German defensive strongholds into one of the most popular tourist destinations in France.

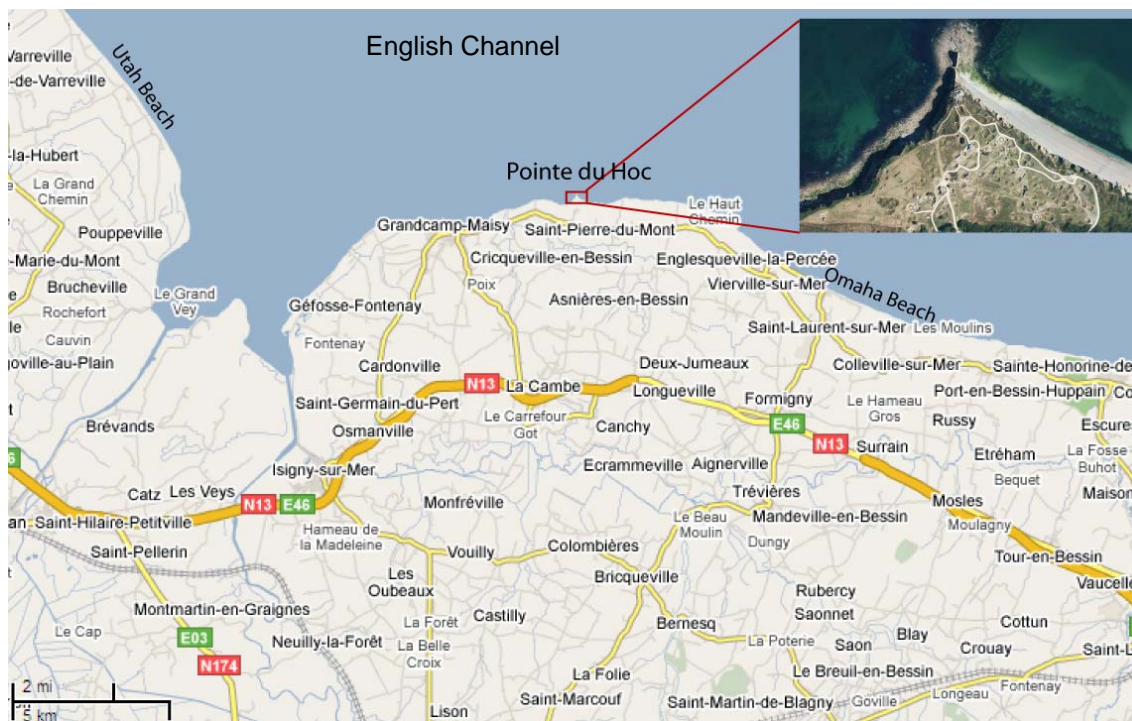


Figure 2.1. Location of Pointe du Hoc in Normandy, France. It is located ~ 75 km to the south–east of Cherbourg, ~60 km to the north–west of Caen, and ~ 300 km to the west of Paris.

Today, Pointe du Hoc remains a jumbled and chaotic landscape of concrete, steel and bomb craters (Figure 2.2). Massive chunks of reinforced concrete studded with corroded steel I–beams and reinforcing bars lie strewn around the site, thrown in some cases tens of meters by the force of an explosion. Hundreds of bomb and shell craters, up to 10 m in diameter and 4 m deep, survive from the aerial and naval bombardments. Many of the original fortifications have been left in place at the site. The most important example is the observation post building, on top of which the Ranger Monument has been in place since 1979 (Figure 2.3a). This building is perched at the most northern

position on the point with a commanding view of the Channel. The observation post however has been closed to visitors since 2001 due to significant cliff collapses in the vicinity and fears of additional mass movement. Another important fortification is the anti-aircraft building located to the east of the observation post which, like the observation post, is located just a few m away from the cliff edge (Figure 2.3b). Anti-aircraft east is also jeopardized by potential cliff collapses. This building served as Ranger leader Colonel Rudder's command post as the invasion unfolded.



Figure 2.2. The battlefield landscape of Pointe du Hoc.

The observation post, which constituted the German command center for the entire Pointe du Hoc battery, is of Wehrmacht construction type 636a and designated as

Leitstand für Heeresküstenbatterie (Warden et al., 2007). At 1250 m³ of reinforced concrete, it is the largest building on site. It was used by the Germans to observe ship activity in the Channel waters, to send and receive wireless communications, and other activities. The memorial was erected by the French to honor elements of the American Second Ranger Battalion. The monument consists of a simple granite pylon with tablets at its base inscribed in French and English.

The eastern anti-aircraft east building, or Rudder's command post, is of type L409a and designated as *Untertand mit aufgesetztem, Geschützstand für 2/3.7 cm Flak* (Warden et al., 2007). The two-storey building, containing 635 m³ of concrete, accommodated 40-mm guns in the upper storey with a crew room and aid station beneath.

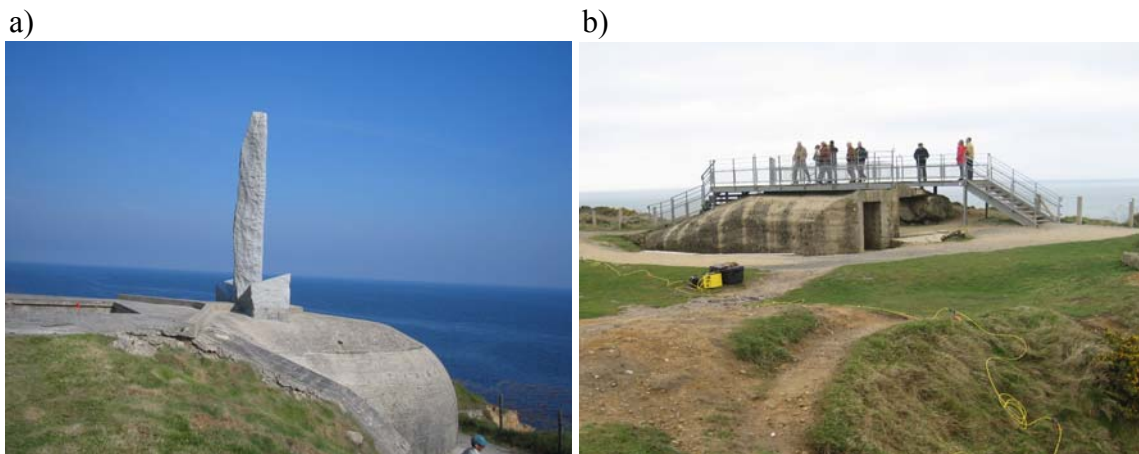


Figure 2.3. Photos of the two at-risk buildings. (a) The observation post with the U.S. Ranger memorial; (b) Rudder's command post.

GEOLOGICAL OVERVIEW

The English Channel area has experienced a complex geological history (Lagarde et al., 2003) which has shaped the current landscape and subsurface features that we are investigating. The overall structural framework is best understood in terms of

major deep crustal faults that developed during Paleoproterozoic continental collisions associated with the plate tectonic assembly of the Pangaea supercontinent.

The ancient thrust faults that developed in the Channel area were later reactivated during the Mesozoic era as Pangaea underwent a period of tectonic extension associated with the opening of the Atlantic Ocean. This extension led to rifting, thermal subsidence, and the consequent development of sedimentary basins. The widening of the nascent Mesozoic basins in response to continuing crustal extension and regional subsidence resulted in the Channel area shifting from a continental to a shallow marine environment.

In the shallow, warm marine environment during the middle Jurassic, reef-building and other marine organisms thrived. Accordingly, a platform carbonate was deposited in submerged Normandy. The area of maximum sediment accumulation is termed the Sillon Marneux Peri-Armoricain (Rioult et al., 1991) and forms an elongated depocenter that trends roughly E-W and stretches across the Baie de Seine to the Western Approaches trough off the northern Brittany coast. Further episodes of folding and faulting, trending roughly NNE, developed along the Normandy coastline during the late Bathonian and Oxfordian stages roughly 155–165 million years ago. This deformation of the carbonate platform is the likely origin of many of the folds and fractures that are evident in the cliffs today.

The continuing structural evolution of the Channel area throughout the Cenozoic has been controlled by two important plate boundaries: the divergent mid-Atlantic ridge which includes the Iceland mantle plume to the north and west, and the Alpine convergent zone to the south. The opening of the Atlantic combined with Iceland hotspot magmatism, coupled with the Alpine convergence, serves to compress and uplift the Channel area, and has led to inversion of the Mesozoic basins with normal faults converting to reverse faults (Lake and Karner, 1987).

The slow tectonic movements associated with the Cenozoic uplift were accompanied in the Plio-Pleistocene by a series of eustatic sea level changes which periodically exposed and submerged the coast of northern France. This is evident by the

marine transgressive–regressive cycles observed in sedimentary basins of the Cotentin peninsula (Dugue, 2003) and in the marine sands and gravels that often overlie indurated Mesozoic formations (Bates et al., 2003).

The Normandy landscape today bears the further imprint of a Pleistocene periglacial environment. The Quaternary sediment cover throughout the region is typically a quartz–calcareous, homogeneous loess with low iron (<2 %), very low organic carbon (<0.2 %) and moderate clay (<20%) contents (Antoine et al., 2003). Much of the loess accumulation, normally 2–8 m thick throughout the region, is attributed to the Weichsel glaciations between 15–25 thousands of years ago. During this time of low sea–level, in which glacial ice covered most of Britain except its extreme southern portions, northern France experienced a dry steppe–tundra climate. Large quantities of silt reworked from calcareous detrital sediments lying on the exposed floor of the English Channel were blown into the region by prevailing northwest winds.

The outcrops at the Pointe du Hoc cliffs (Figure 2.4) are mixed carbonate and siliciclastic rocks of mainly Jurassic period that lie between the western margin of the Paris Basin and the eastern margin of the Armorican massif. The rocks occupy the lower to middle Bathonian stage of the Normandy reference section (Figure 2.5) which has been developed by the long efforts of geologists on the basis of outcrop studies, micropaleontological analyses and the identification of ammonite fauna (Riout et al., 1991). The basal unit of the Pointe du Hoc cliff section, exposed ~2–3 m above the beach, is the Marnes de Port formation which is a fine clastic alteration of marls and limestones. The overlying bedrock formation is the Calcaire de Creully (also known as Calcaire de St. Pierre du Mont) which is a ~16–m thick system of fractured limestones alternating with hard sandstones (Figure 2.6). The limestone formation has a carbonate content of 30–80%. The formation also contains some quartz, silt, and clay minerals composed of smectite and some illite (Briaud et al., 2007).

Tracing the dark gray layer of Marnes de Port marl formation along the beach of Pointe du Hoc indicates that the rock beds dip northward at ~5°. This explains why the gray marl does not appear beneath the observation post but is found at the location of

Rudder's command post. The regional dip of the rock strata also explains why the cliffs are not as high at the observation post (~ 18 m) as at Rudder's command post (~ 24 m) (Briaud et al., 2007 and 2008).



Figure 2.4. Jurassic outcrops (outlined in red) in the region between the Paris Basin and the Armorican Massif. Edited from Rioult et al. (1991).

The extent of Plio–Pleistocene deposition at Pointe du Hoc is unclear but, if present, would be represented by the prevailing calcarenite (cemented carbonate sand) and marly sandstones that reside beneath the soil cover. The Quaternary overburden consists of a ~8 m thick layer of ochre–brown silty clay with gravel (Figure 2.7).

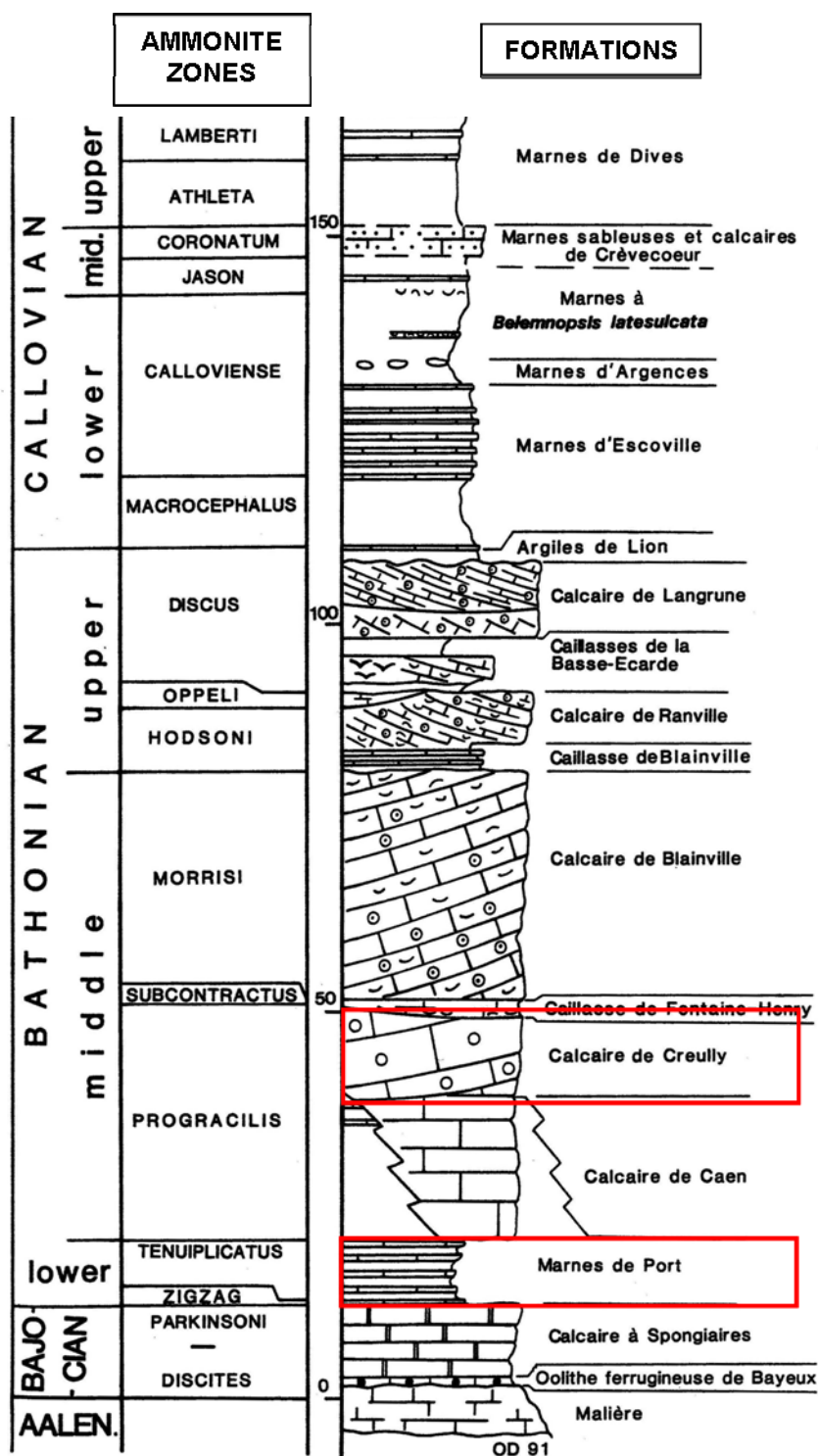


Figure 2.5. The middle Jurassic succession of the Normandy reference section. Outlined in red are the Bathonian formations found at Pointe du Hoc. Edited from Rioult et al. (1991).



Figure 2.6. Pointe du Hoc middle Jurassic formations showing the approximate interface between the lower Bathonian Marnes du Port formation and the middle Bathonian Calcaires de St. Pierre du Mont. The photo is the west side cliffs looking NW from the point.

The general stratigraphy at the site based on borehole information at the observation post area (Briaud et al., 2007) is shown in Figure 2.8. The top layer is an ~8– m–thick layer of unconsolidated Pleistocene silty clay soils (Quaternary sediments), Beneath the silty clay soil layer is a sequence of ~4–m–thick highly fractured limestone, 4–m thick hard sandstone, and ~9–m thick fractured limestone and sandstone. This sequence of limestones and sandstones corresponds to the middle Bathonian Calcaires de St. Pierre du Mont formation. The basal layer is a very stiff gray marl of the Bathonian Marnes de Port formation.



Figure 2.7. Exposed by a recent soil–wedge failure is the Quaternary soil cover at Pointe du Hoc (upper, dark layer), underlain by layered calcaenite and marls of possible Plio–Pleistocene origin.

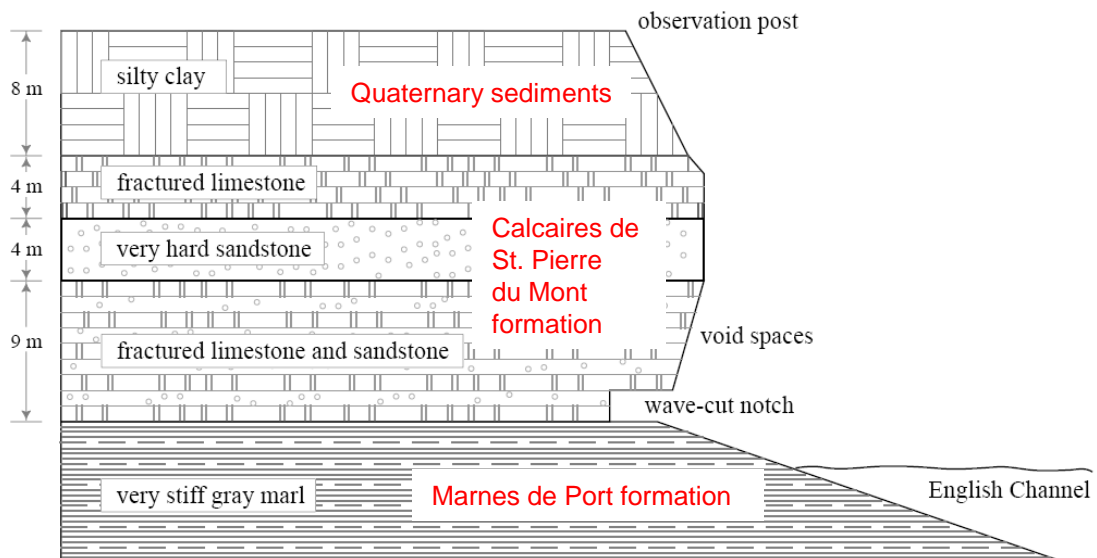


Figure 2.8. Pointe du Hoc cliff stratigraphy based on borehole information acquired by Texas A&M geotechnical team. After Briaud et al. (2007).

SITE HYDROGEOLOGY

The leeward beach east of Pointe du Hoc consists of sand overlain by re-worked gravel, cobbles and boulders that have eroded from the cliffs, while the windward beach to the west consists of wave-cut, rocky Marnes de Port terraces (Figure 2.9). Tidal currents are effective at removing sand from the beach, transporting it eastward where it accumulates either in the Seine estuary or in massive dunes on the north-trending coast between the Somme estuary and Boulogne (Anthony, 2002). The beach gravel, too large to be shifted by the tidal currents, is washed out to an offshore reservoir during large storms and is re-deposited on the beach face during quiet times (Antoine, et al., 2003).

The fractures in the Jurassic strata are likely associated with Bathonian and Oxfordian tectonic movements but many could be of later provenance and/or solution-enlarged by percolating groundwater. There are numerous fractures evident in the cliff face, some of which support vegetation and clearly transmit groundwater. The basal marl unit Marnes de Port, in particular, appears to restrict the vertical flow of groundwater as many of the seeps at the cliff face emanate from the top of this layer (Figure 2.10). The areas of heaviest vegetation on the Pointe du Hoc cliff face are associated with the groundwater seeps. The seepage is particularly noticeable during and after the heavy rain falls. The bomb craters, located in the top soil layers, do not retain standing water after storms except at the extreme western part of the site where the overlying soil layer thins considerably to less than 1 m. These observations suggests that the cliffs throughout much of the site are well-drained, with infiltrating water readily percolating though the fractures in the limestones and onto the beach, as shown in Figure 2.10. The rock mass is naturally fractured as a consequence of the slow tectonic forces described earlier. It is assumed that groundwater flow through the rock matrix is minimal; as in many other fractured rock systems dominated by fissure flow (e.g. Neuman, 2005). The top of Marnes de Port is also roughly the depth of the water table at the site, as measured by piezometers installed by the geotechnical engineering team (Briaud et al., 2007).

CLIFF INSTABILITY

The existence of the historic battlefield at Pointe du Hoc is jeopardized by the risk of potentially devastating cliff collapses. These frequently occur along the English Channel coasts of Britain and France (Mortimore and Dupperet, 2004). The stability of the Cretaceous chalk cliffs to the east of Pointe du Hoc area has been particularly well-studied. A number of important failure mechanisms have been identified (Mortimore et al., 2004).

a)



b)



Figure 2.9. The leeward beach east of Pointe du Hoc. (a) Looking west toward Pointe du Hoc after a large storm, March 2008. The sandy beach in the foreground is exposed after much of the gravel has been transported offshore, leaving only large cobbles and boulders. (b) Looking south, the rocky wave-cut terraces seen in the foreground extend to the west along the coastline.

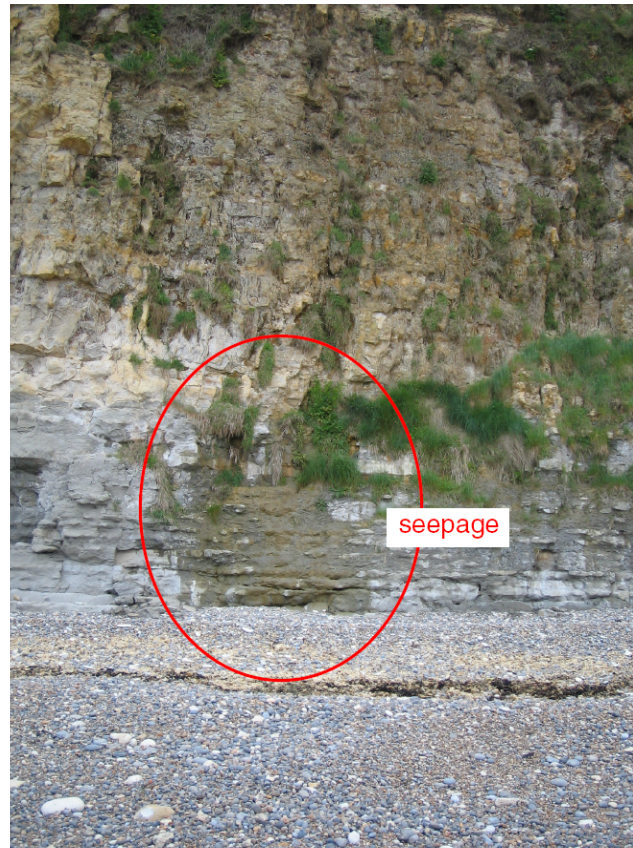


Figure 2.10. Groundwater seepage from cliff face at the top of the Marnes de Port marl.

The long-term cliff retreat rate between 1873–2001 along the English south coast between Eastbourne and Brighton has been estimated at ~ 0.35 m/yr based on an analysis of maps and aerial photos (Dornbusch et al., 2008). The cliff retreat rate appears to be decreasing slightly for unknown reasons over the past several decades, with spatial variations in the retreat rate being strongly linked to the local lithology. Chalk however, with its fine intergranular texture, has different strength properties compared to the mixed siliciclastic–carbonate geomaterials found at Pointe du Hoc, which are more likely to exhibit induration and vuggy textures. The extensive literature on chalk cliff stability and retreat rates therefore appears to have only limited applicability for our purposes.

There have been a number of large mass movement episodes at Pointe du Hoc in recent history as evidenced by numerous landslide scars near the cliff top, in addition to debris piles and wave-cut notches at the base of the cliffs (Figure 2.11). Briaud et al. (2007) stated that the rate of erosion of the cliffs from 1944 to 2006 was approximately 0.17 m/year. This number was confirmed by the work of Savouret (2007) who, after an extensive study of aerial photographs, reported that the rate of erosion of the cliffs from 1823 to 1944 was 0.18 m/year, from 1944 to 2002 was 0.15 m/year on the west side, and from 1944 to 2002 was 0.21 m/year on the east side. A detailed analysis by Warden et al. (2007) based on historical aerial photographs provides information on the differences since 1944 in the cliff line due to the bombing and shelling rather than erosion.

Briaud et al. (2007 and 2008) determined failure mechanisms of the cliffs at Pointe du Hoc. Their analysis shows that failures occur in two forms; slope failure in the top soil cover due to loss of suction after long periods of heavy rains and overhang collapse in the basal part of the rock cliffs due to sea wave attack. The rainwater percolates through the rock mass, which is naturally fractured and drains very well, weakening joint networks in the underlying strata, enlarging fractures via dissolution and emerging as seeps in the cliff face. The percolating fresh water also decreases the overall rock mass strength, causing rock blocks to behave individually rather than as a single mechanically coherent body. Furthermore, extended vertical cracks can develop due to frost heave or horizontal decompression forces associated with mass movement.

Once the cliff has been structurally weakened by the aforementioned processes, wave action especially during storms can dislodge the rock blocks creating caverns at the base of the cliffs. The formation and enlargement of caverns eventually undermines the cliffs, creating a critical tensile stress that causes additional wedge failures at the cliff top.

a)



b)



Figure 2.11. Rock collapses and marine basal notching. (a) A pair of recent collapses on the east side of Pointe du Hoc; note the persons at the top and bottom of the photo for scale; (b) marine basal notching at the bottom of the cliffs; note the rock climber for scale.

CHAPTER III

ELECTRICAL RESISTIVITY SURVEY PRINCIPLES

This chapter describes basic theoretical principles, field procedures, forward modeling and inversion techniques of the geophysical resistivity method. Electrical resistivity of the Earth materials, especially that of the carbonate rocks relevant to Pointe du Hoc resistivity data interpretation, is also discussed here.

FUNDAMENTAL RESISTIVITY THEORY

Electrical resistivity is an important physical property of Earth materials and is diagnostic of subsurface hydrogeological conditions. Electrical resistivity is a measure of how a material resists a steady electrical current flow. The electrical resistivity of a cylindrical sample of length L (m) and uniform cross-section area A (m^2), having resistance R between the end faces, is given by $\rho = RA/L$. The unit of resistivity ρ is ohm-meter (Ωm). The resistance R is given in terms of the electric potential V applied across the ends of the cylinder and the resultant current I flowing through it, by Ohm's law $R=V/I$. The units of R , V , and I are ohms (Ω), volts (V), and amperes (A) respectively.

An electrical resistivity survey is an electrical geophysical technique to investigate the subsurface resistivity distribution beneath an area of interest. In general, an electric current is injected into the ground, and the resulting voltage differences are measured at the surface of the Earth. From this voltage measurement, the true resistivity of the subsurface can be estimated. Anomalous conditions or inhomogeneities within the ground, such as relatively conducting or resistive zones, are inferred from the fact that they deflect the current and distort surface potential readings. The ground resistivity is related to various geological parameters such as the mineral and fluid content, porosity and degree of water saturation in the rock. Further discussion of resistivity surveys can be found in Ward (1990), Sharma (1997), Loke (2004) and Zonge et al. (2005).

The fundamental physical law upon which geophysical resistivity surveys are based is Ohm's law which governs the current flow in the ground. Ohm's law can be written in vector form as

$$\mathbf{J} = \sigma \mathbf{E}, \quad (3.1)$$

where \mathbf{J} is the current density, \mathbf{E} is the electric field intensity, and σ is the electrical conductivity, the reciprocal of resistivity ρ . In practice the electric potential V is measured. The relationship between the electric potential and the electric field intensity is given by

$$\mathbf{E} = -\mathbf{grad} V \quad (3.2)$$

Combining equations (3.1) and (3.2), we get

$$\mathbf{J} = -\sigma \mathbf{grad} V \quad (3.3)$$

The simplest approach to the theoretical study of the current flow in the ground is to consider first the case of a homogeneous isotropic subsurface and a single point current source on the ground surface (Figure 3.1a). In this case, the current flows radially away from the source. The equipotential surfaces develop into a hemispherical shape, with the current flow perpendicular to the equipotential surface. At some distance r from the current source, the hemispherical shell has surface area $2\pi r^2$, so the current density J is

$$J = I/2\pi r^2 \quad (3.4)$$

Note that \mathbf{J} is a vector pointing in the radial direction.

Since $\rho = 1/\sigma$ and using equation (3.4), then equation (3.1) can be written as

$$-\frac{\partial V}{\partial r} = \rho I / 2\pi r^2 \quad (3.5)$$

The potential V at distance r from the current source is given by integrating equation (3.5), the result of which is

$$V = \int_r^{\infty} (\rho I / 2\pi r^2) dr = I\rho / 2\pi r \quad (3.6)$$

This equation provides the fundamental relationship for electrical prospecting performed at the surface of a uniform isotropic earth.

In reality, a single electrode, by itself, cannot inject current into half-space; a return electrode is required such that the current flows into the ground via one (source) and exits via the other (sink) electrode, as in Figure 3.1b. The potential measured at passive electrode P_1 due to current entering and exiting via active electrodes C_1 and C_2 is

$$V_{P_1} = \frac{I\rho}{2\pi} \left[\frac{1}{r_{C_1P_1}} - \frac{1}{r_{C_2P_1}} \right], \quad (3.7)$$

where the minus sign in the second term of equation (3.7) recognizes the change in sign of the current at the source and sink electrodes C_1 and C_2 , and where $r_{C_1P_1}$ is the distance between P_1 and C_1 while $r_{C_2P_1}$ is the distance between P_1 and C_2 .

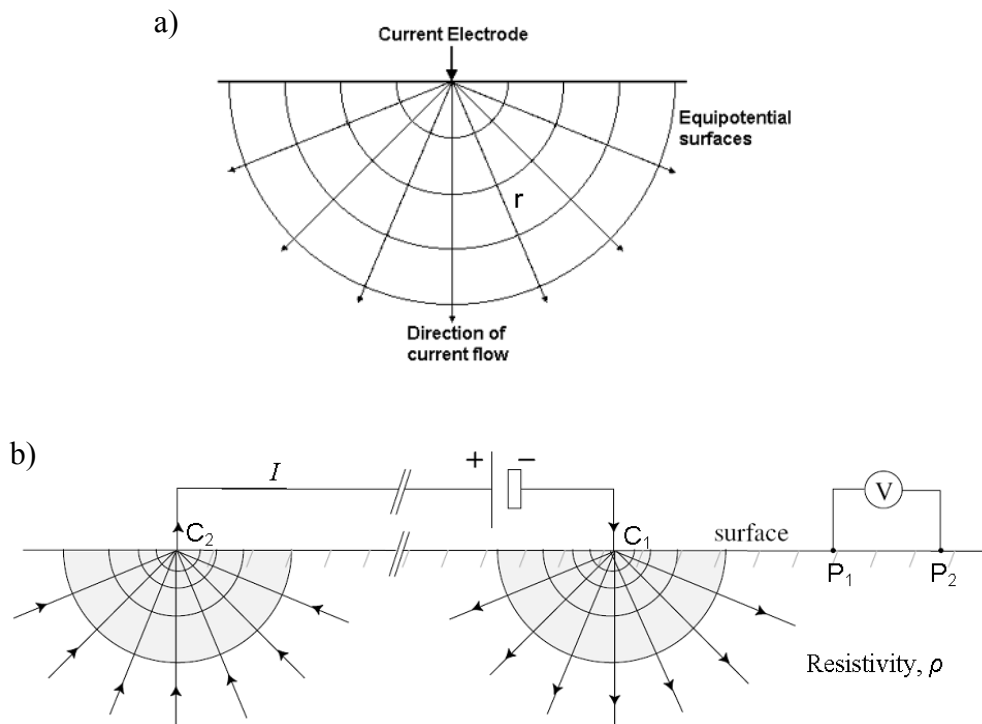


Figure 3.1. Electrical current flow diagrams. (a) The flow of current from a point current source into a homogeneous Earth and the resulting potential distribution. (b) Voltage measured between electrodes P_1 and P_2 for a point source C_1 and point sink C_2 of electric current.

In practice a potential difference between two points, rather than an absolute potential, is measured. The potential difference for a four electrode array is given by

$$\Delta V = \frac{I\rho}{2\pi} \left[\frac{1}{r_{C_1P_1}} - \frac{1}{r_{C_2P_1}} - \frac{1}{r_{C_1P_2}} + \frac{1}{r_{C_2P_2}} \right], \quad (3.8)$$

where $r_{C_1P_2}$ is the distance between P₂ and C₁ while $r_{C_2P_2}$ is the distance between P₂ and C₂.

The resistivity of a half-space is then given by solving (3.8) for ρ , that is,

$$\rho = k \frac{\Delta V}{I}, \quad (3.9)$$

where k is called the geometric factor which depends on the specific configuration of current and potential electrodes. Figure 3.2 shows the common electrode arrays used in resistivity surveys, along with their geometric factors. Note that in this study, a combination of dipole-dipole and Schlumberger arrays was used in the data acquisition. The details of the data acquisition will be explained in the next chapter.

Equation (3.9) gives the true resistivity that would be calculated from potential measurement over a homogeneous half-space with the 4-electrodes configuration. The resistivity so obtained is constant and independent of both the electrode configuration and the surface location of the electrodes. For an inhomogeneous earth the resistivity ρ , computed from equation (3.9), will vary according to the geometric arrangement of the electrodes or on the horizontal location of the array. The resistivity obtained from equation (3.9) for an inhomogeneous subsurface is, therefore, properly viewed as an *apparent resistivity*, written as

$$\rho_a = k \frac{\Delta V}{I}. \quad (3.10)$$

The apparent resistivity should not be considered as some kind of a spatially averaged resistivity of the homogeneous subsurface formation. It is the resistivity that the potential readings would assign to the ground if it were homogeneous. The apparent resistivity concept is very useful in practical applications. To determine the true subsurface resistivity from the measured apparent resistivity values is the “inversion”

problem. Methods to carry out inversion will be discussed in more detail in a later section of this chapter.

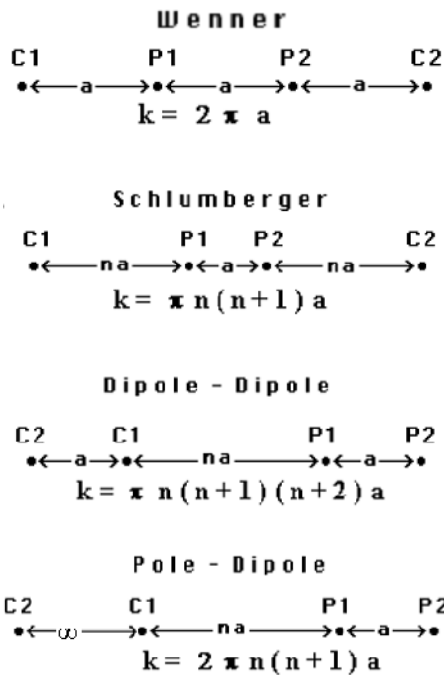


Figure 3.2. Common arrays used in resistivity surveys and their geometric factors. Note that the dipole–dipole, pole–dipole and Schlumberger arrays have two parameters, the dipole length “a” and the dipole separation factor “n”. While the “n” factor is commonly an integer value, non–integer values can also be used. k is the geometric factor. Edited from Loke (2004).

MULTI-ELECTRODE DC RESISTIVITY FIELD SURVEY

Classical dc electrical resistivity surveys are carried out with simple equipment consisting of a high voltage battery pack as the source of current, four metal stakes as electrodes, an ammeter, a volt–meter, and four reels of insulated cable. However a problem in such surveys is the practical difficulty of moving electrodes with large spreads of wire attached. This requirement makes the field work slow and expensive, particularly in rugged, swampy or heavily vegetated terrains. Moreover the classical

survey technique is limited to simple 1-D subsurface resistivity model interpretation, while in reality the subsurface is more complex.

2-D Resistivity Surveys

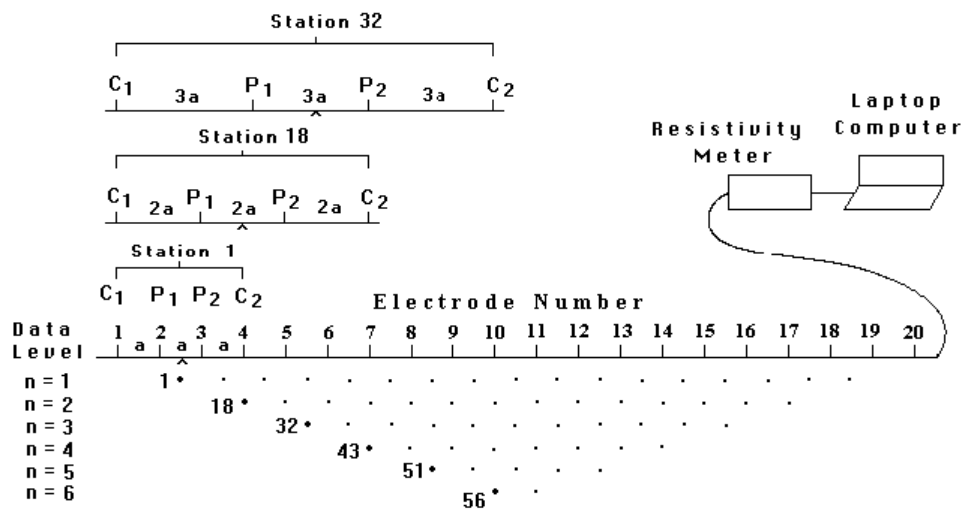
A 2-D subsurface resistivity model provides more accurate subsurface imaging. The resistivity varies in both the vertical direction and the horizontal direction along the survey line. In the 2-D case, it is assumed that subsurface resistivity does not change in the direction perpendicular to the survey line. In theory, a fully 3-D resistivity survey and interpretation should be even more accurate. However, 2-D surveys are the most practical economic compromise between obtaining accurate images and keeping the survey costs down (Dahlin, 1996).

2-D electrical resistivity surveys are widely used to map areas with moderately complex geology where the classical 1-D resistivity soundings and profiling do not provide sufficiently accurate results. Such surveys are usually carried out using a large number of electrodes connected to a multi-core cable. A laptop computer together with an electronic switching unit is used to automatically select the four electrodes for each measurement. In recent years, field techniques and the equipment to carry out efficient 2-D resistivity surveys have become fairly well developed. The necessary field equipment is commercially available from a number of international companies e.g. AGI (<http://www.agiusa.com>), Geometrics (<http://www.geometrics.com>), etc. Note that, for the Pointe du Hoc survey, an AGI multi-electrode resistivity system was used. Details of the data acquisition are presented in the next chapter.

The typical setup for a 2-D survey with a number of electrodes arrayed along a straight line and attached to a multi-core cable is shown in Figure 3.3 (Loke and Barker, 1996a). Generally a constant spacing between adjacent electrodes is used. The multi-core cable is attached to an electronic switching unit which is connected to a laptop computer or has a built-in computer. The sequence of measurements to take, the type of electrode array to use, and other survey parameters is programmed into the computer. After reading the control file, the system automatically selects the appropriate sequence

of electrodes to complete the measurements. Most of the fieldwork is involved in laying out the cable and electrodes. After that, the measurements are taken automatically and stored in the computer. A significant amount of the survey time is spent waiting for the resistivity meter to complete the set of measurements.

The roll-along survey technique is now widely used in resistivity surveys to extend horizontally data coverage, particularly for a resistivity system with a limited number of cables and electrodes. After completing the initial sequence of measurements, the cable is moved past one end of the line by several unit electrode spacings. All the measurements which involve the electrodes on the part of the cable which does not overlap the original end of the survey line are then repeated.



Sequence of measurements to build up a pseudosection

Figure 3.3. The arrangement of electrodes for a 2-D electrical survey and the sequence of measurements used to build up a pseudosection. From Loke and Barker (1996a).

Pseudosection Data Plotting Method

Pseudosections are normally used to display apparent resistivity data from a 2-D resistivity survey. A horizontal location is defined as the mid-point of the electrode

array used to make a given apparent resistivity measurement. A vertical location is defined to be some distance that is proportional to the separation between the electrodes (Loke, 2004). For the dipole–dipole array, for example, apparent resistivity data are plotted at the intersection of the two lines drawn at a 45° angle to the horizon from the center of the current (C_1 – C_2) and the potential (P_1 – P_2) dipole pairs. Figure 3.3 shows an example of apparent–resistivity pseudosection plotting.

Pseudosections give very approximate pictures of the subsurface resistivity distribution beneath the survey lines; however they provide only a distorted picture of the subsurface because the shape of the contours depends on the type of array (Loke, 2004). These data have to be modeled or inverted to convert the pseudosections into a 2–D resistivity section that is ready for geological interpretation. The main use today of the pseudosection is for data quality analysis. Poor–quality apparent resistivity measurements, which normally stand out as extreme values on the pseudosections, are readily identified and removed. Note that the measured pseudosection is simply a convenient way of presenting the raw field data. The calculated apparent resistivity pseudosection based on the 2–D inversion result is normally also shown to demonstrate pictorially the goodness–of–fit achieved by the inversion process. Ideally, the calculated pseudosection should closely match the measured pseudosection.

3–D Resistivity Surveys

Since all realistic geological structures are 3–D in nature, a fully 3–D resistivity survey and inversion provide the most accurate subsurface imaging (Loke and Barker, 1996b). 3–D surveys have not been used as routinely as the 2–D surveys. The main reason is that the survey cost is comparatively high for large survey areas since data acquisition time increases greatly. Fast computers are now able to handle with relative ease the inversion of large data sets.

In conventional 3–D resistivity surveys, electrodes must be located on the nodes of a regular perpendicular grid (Figure 3.4). In this case, commercial inversion software packages such as *RES3DINV* (<http://www.goelectrical.com>) and *EarthImager 3D*

(<http://www.agiusa.com>), which typically use a smoothness-constrained least-squares method, are used to invert the data in terms of a 3-D resistivity model. In some cases, a 3-D data set can be built up from a number of parallel 2-D lines. The data from each 2-D survey line is initially inverted independently to give 2-D resistivity inversion profile. The whole data set is finally combined into a 3-D dataset and inverted to give a fully 3-D resistivity image/tomogram. The quality of the 3-D model is expected to be poorer than that produced with an arbitrary 3-D survey featuring many crossing profiles. However such a 3-D resistivity image could still reveal major resistivity anomalies across the survey lines. This provides an alternative cost-effective solution in some cases.

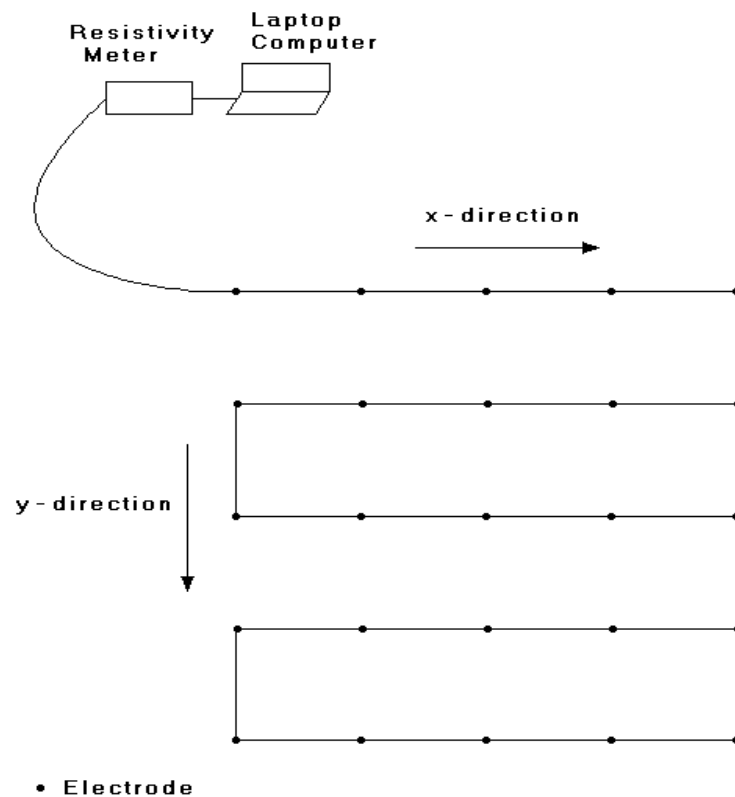


Figure 3.4. The arrangement of the electrodes for a conventional 3-D survey. From Loke and Barker (1996b).

A more general approach to obtain a 3-D subsurface resistivity tomography is to combine several 2-D survey lines arranged in an irregular patterned grid, into a single 3-D dataset and to invert the data using non-commercial inversion software. The program BERT (<http://resistivity.net>) is based on the 3-D forward modeling and inversion algorithms described in Rücker et al. (2006) and Günther et al. (2006). For this study this strategy was utilized to acquire resistivity data and invert them to obtain high-resolution 3-D subsurface resistivity images beneath the Pointe du Hoc site. The forward modeling and inversion algorithms are briefly described in the following sections of this chapter.

FORWARD MODELING

Forward modeling of dc resistivity data has progressed considerably from early integral equation, finite element (FE) and finite difference (FD) approaches. A useful technique is to decompose the electric potential into background and secondary components, a technique known as *singularity removal*. A limitation of the FD method is the requirement of regular, structured grids which do not conform to irregular conductor boundaries. This limitation is overcome by the increasingly popular FE method. Early 2-D FE codes incorporated crude representations of topography but used essentially regular grids. We have used a FE approach (Rücker et al., 2006) that is based on a completely unstructured tetrahedral grid (see Figure 3.5), resulting in great flexibility in modeling 3-D structures.

There are many advantages to using unstructured meshes. The model geometry and the electrode layout can be described flexibly. Electrode positions may be arbitrarily assigned to predetermined nodes. The mesh can be locally refined in the vicinity of electrodes or sharp conductivity contrasts. Coarse grids can be used toward the outer mesh boundaries to save computational resources.

The essential computational step in forward modeling is solution of a sparse system of linear equations, one for each electrode configuration. Both indirect and direct matrix solutions techniques have advantages. Node re-ordering is performed to reduce the computational burden. Accuracy in the FE solution may be increased by grid

refinement and the use of higher-order basis functions. The governing boundary value problem is

$$\mathbf{div} \cdot (\sigma \mathbf{grad} u) = -\mathbf{div} \cdot \mathbf{j} \quad (\text{inside the modeling domain}); \quad (3.11)$$

subject to

$$\sigma (\partial u / \partial n + \alpha u) = \mathbf{j} \cdot \mathbf{n} \quad (\text{on the boundaries}); \quad (3.12)$$

where $\sigma = \sigma(x, y, z)$ is a 3-D subsurface conductivity distribution and \mathbf{j} is the source current density. The electric potential is $u = u(x, y, z)$ and \mathbf{n} denotes the outward normal. It is assumed that a current I is injected either through a point-like electrode at Earth's surface or within the interior of the modeling domain.

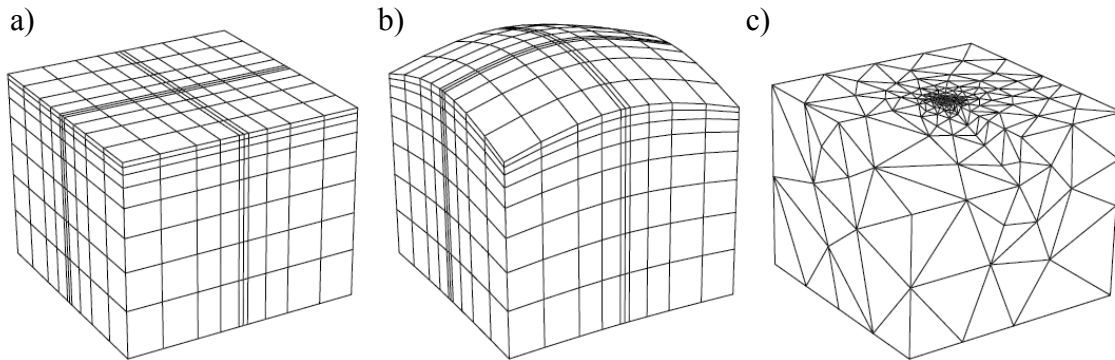


Figure 3.5. Three dimensional grids used for dc resistivity forward modeling. (a) Structured grid, (b) block-oriented grid, and (c) unstructured tetrahedral grid. From Rucker et al. (2006).

Suppose an electrode is located at the position $\mathbf{r}_s = (x_s, y_s, z_s)$, then the source term in equation (3.11) becomes $\mathbf{div} \cdot \mathbf{j} = I\delta(\mathbf{r} - \mathbf{r}_s)$. The boundary condition (equation 3.12) with $\alpha = 0$ indicates that current cannot flow out of the Earth's surface into the insulating atmosphere. On the other boundaries of the modeling domain, we apply $\alpha = \mathbf{n} \cdot \mathbf{r} / |\mathbf{r}|^2$ which accurately models the fall-off in electric potential beyond the outer boundaries.

The modeling domain is completely tiled by non-overlapping tetrahedra. This leads to a system of equations $\mathbf{A}\mathbf{u} = \mathbf{b}$ which is positive-definite, symmetric and sparse, and of dimension N , the number of nodes. The vector \mathbf{u} contains the nodal potential values and \mathbf{b} is the source vector.

The Dirac delta function $\delta(\mathbf{r}-\mathbf{r}_s)$ yields a singular electric field, or potential gradient, value at the electrode position \mathbf{r}_s . Traditionally, this has meant that the electric field is computed inaccurately in the vicinity of electrodes. The singularity is removed by decomposing the potential u into primary and secondary parts, $u = u_p + u_s$. The matrix equation in the primary-secondary formulation becomes

$$\mathbf{A}^\sigma \mathbf{u}_s = \mathbf{A}^{\Delta\sigma} \mathbf{u}_p, \quad (3.13)$$

where $\Delta\sigma = \sigma - \sigma_p$ and σ_p is the conductivity in the direct vicinity of the electrodes. A system of equations $\mathbf{A}\mathbf{u}^l = \mathbf{b}^l$ has to be solved for each current source, $l = 1, 2, \dots, E$. The linear system in equation (3.13) therefore is required to be solved E times. It is most efficient to solve the system of equations for each single electrode acting as a source, and then to superimpose the potentials to simulate the response of any given source/sink configuration. The initial mesh design should include the electrode positions as fixed nodes. An additional refinement near the electrodes is required for accurate computation of the potentials at these locations.

The computed secondary potential u_s is transformed into an apparent resistivity ρ_a by means of the geometric factor k appropriate for the electrode configuration. The geometric factor k , defined such that ρ_a is equal to the resistivity of the equivalent uniform half-space, clearly depends on the surface topography. If the latter is non-trivially variable, the geometric factor k does not have an analytic form. We need to find a suitable approximation k_a which takes into account the surface geometry effect.

It is important to correctly interpret ρ_a as due to subsurface conductivity anomalies, rather than misinterpret the result because an incorrect geometric factor was used. In other words, we need to accurately assess the effects of topography on ρ_a . We define the *geometry effect* as

$$t = k_a/k. \quad (3.14)$$

A value of $t = 1$ indicates that the ρ_a measurement is unaffected by topography. The numerical geometric factor k_a in the presence of topography is computed using a subsurface resistivity of $\rho_a = 1 \text{ } \Omega\text{m}$, in which case $k_a = I\rho/\Delta u$. An example based on resistivity data from Merapi volcano in Indonesia is given in R ucker et al. (2006).

INVERSION METHOD

The purpose of an inversion is to reconstruct the subsurface resistivity distribution $\rho(\mathbf{r})$ based on a measured apparent resistivity pseudosection. The inverse dc resistivity problem is generally ill-posed since a large number of different resistivity distributions can be found each of which are consistent with a given pseudosection. The inverse problem is also non-linear so that the normal procedure is to adjust the resistivity model $\rho(\mathbf{r})$ in an iterative process starting from an initial guess $\rho_0(\mathbf{r})$. The finite element forward solver of R ucker et al. (2006), as previously described, is used to compute a pseudosection at each step. The model adjustment is determined based on the goodness of fit between the computed and the measured pseudosections. In this study the inversion approach of G unther et al. (2006) was used.

One of the challenges of the inverse problem is to efficiently transform between the forward problem, which requires a fine discretization of the subsurface, and the resistivity structure, which is defined on a coarser mesh. Accordingly, there are three different meshes associated with the inversion, as indicated in Figure 3.6. A model parameter mesh (Figure 3.6a) divides the subsurface into coarse cells, each of which can be assigned a uniform resistivity. A secondary potential mesh on which u_s is computed is shown in Figure 3.6b; it is similar to the parameter mesh but extends to greater lateral distances and depths in order to satisfy the far-field boundary conditions. At Figure 3.6c, we have the finely discretized mesh on which the primary potential u_p is computed. Note that the primary mesh is highly refined in the vicinity of the electrodes, which are marked by the arrows. The primary potential u_p needs to be computed only once at the start of the inversion, which is an advantage since a forward solution is expensive to obtain on such a large mesh.

The resolution of the dc resistivity inverse problem has been investigated by many authors (e.g. Friedel, 2003). Resolution is a measure of the minimum separation between two resistivity bodies such that they can be distinguished as two separate bodies in the reconstructed image. Günther et al. (2006) has broadly suggested that the lateral resolution at the surface of a resistivity dataset is roughly 0.5–1.0 times the electrode spacing. The spatial resolution degrades exponentially with depth, until the maximum depth penetration which is typically several times the electrode spacing. A sensitivity analysis can be carried out after an inversion to gauge the spatial resolution of particular features of interest within a reconstructed image.

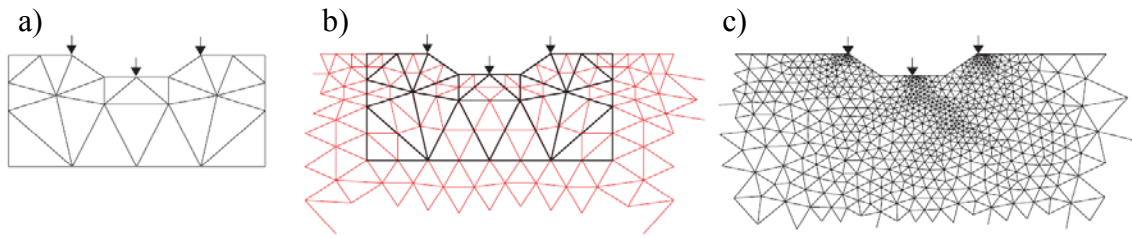


Figure 3.6. The three meshes used in the inversion algorithm. (a) The model parameter mesh; (b) the secondary field mesh; (c) the primary field mesh. The arrows indicate electrode locations. From Günther et al. (2006).

A Gauss–Newton regularized optimization technique is used in this study to construct the resistivity tomograms. In this approach, one of the goals is to reduce the misfit Φ_d between the model response $\mathbf{F}(\mathbf{m})$ and the data vector \mathbf{d} . The misfit is defined as

$$\Phi_d(\mathbf{m}) = \sum_{i=1}^N |(d_i - F_i(\mathbf{m})) / \varepsilon_i|^2, \quad (3.15)$$

where the M –dimensional model vector $\mathbf{m} = (m_1, m_2, \dots, m_M)^T$ is defined with $m_j = \log \rho_j$, the logarithm of the resistivity of the j –th cell in the model parameter mesh. The superscript T denotes vector transpose. Logarithms are used to ensure the positivity of the model parameters, which helps to stabilize the inversion. The N –dimensional data

vector is defined as $\mathbf{d} = (d_1, d_2, \dots, d_N)^T$ with $d_i = \log(\rho_a)_i$, the logarithm of the i -th measured apparent resistivity. The data error vector is defined as $\boldsymbol{\varepsilon} = (\varepsilon_1, \varepsilon_2, \dots, \varepsilon_N)^T$. The model response $\mathbf{F}(\mathbf{m})$ in equation (3.15) is the predicted dataset computed using the forward solver for model \mathbf{m} .

Simply minimizing the data misfit Φ_d to its lowest possible value is intuitively appealing, but this strategy does not generate an acceptable tomographic image of the subsurface resistivity distribution. The reason is that the data become grossly over-fit, introducing spurious subsurface structure that serves only to accommodate data errors, and renders the imaging procedure unstable. Some type of *regularization* procedure is typically used to ensure that the tomogram remains stable while the misfit is reduced. The philosophy of regularized inversion is described in Constable et al. (1987); the objective is to minimize a composite function

$$\Phi(\mathbf{m}) = \Phi_d(\mathbf{m}) + \lambda\Phi_m(\mathbf{m}), \quad (3.16)$$

where Φ_m is a regularizing function such as

$$\Phi_m = \|\mathbf{C}(\mathbf{m} - \mathbf{m}^0)\|^2. \quad (3.17)$$

In equation (3.17), the vector \mathbf{m}^0 is a reference model while the matrix \mathbf{C} describes *a priori* constraints that are imposed by the user on the model. If the matrix \mathbf{C} is chosen to be the identity matrix, the regularizing function reduces to $\Phi_m = \|\mathbf{m} - \mathbf{m}^0\|^2$ and the reconstructed image \mathbf{m} will never become too different from the selected reference model \mathbf{m}^0 . The matrix \mathbf{C} can also be chosen to enforce smoothness constraints amongst the model parameters. In such a case, the reconstruction will be stable and the resulting image will always take on a smooth appearance. Smooth tomograms are constructed in this study.

The value of the regularization parameter λ in equation (3.16) governs the fundamental trade-off between the data misfit and the model smoothness. An excessively large value of λ favors very smooth models that do not fit the data well, while choosing λ too small generates an implausibly rough structure that over-fits the data. Neither of these alternatives provides an acceptable image that can be reliably

interpreted. The optimal choice of λ is somewhat subjective but should reflect a reasonable compromise between smoothness and data misfit.

The function $\Phi_d(\mathbf{m})$ is minimized using an iterative Gauss–Newton method. At the k -th iteration, the model is updated according to

$$\mathbf{m}^{k+1} = \mathbf{m}^k + \tau^k \Delta \mathbf{m}^k, \quad (3.18)$$

where τ^k is the step–size and $\Delta \mathbf{m}^k$ is the solution to the linear system of equations (Park and Van, 1991)

$$[\mathbf{S}^T \mathbf{D}^T \mathbf{D} \mathbf{S} + \lambda \mathbf{C}^T \mathbf{C}] \Delta \mathbf{m}^k = \mathbf{S}^T \mathbf{D}^T \mathbf{D} (\mathbf{d} - \mathbf{F}(\mathbf{m}^k)) - \lambda \mathbf{C}^T \mathbf{C} (\mathbf{m}^k - \mathbf{m}^0) \quad (3.19)$$

where \mathbf{S} is the Jacobian sensitivity matrix $S_{ij}(\mathbf{m}^k) = \partial F_i(\mathbf{m}) / \partial m_j$ and $\mathbf{D} = \text{diag}(1/\varepsilon_i)$ is a diagonal matrix that contains the reciprocals of the data errors. The linear system of equation (3.19) is solved using a conjugate gradient algorithm. The step size τ^k is found by minimizing $\Phi(\mathbf{m})$ along the current direction in model space. The inversion terminates when the model stops changing, that is $\Delta \mathbf{m}^k \rightarrow 0$, or when the misfit $\Phi_d(\mathbf{m})$ achieves some pre–determined tolerance.

ELECTRICAL RESISTIVITY OF EARTH MATERIALS

Electric conduction in most rocks is essentially electrolytic with ions in the pore fluids being the predominant charge carriers (Keller and Frischknecht, 1966). The solid matrix of grains is largely semi–conducting, with notable exceptions being metallic grains and the surface of certain clay minerals which are conducting. Groundwater filling the pore space of rocks is a natural electrolyte with a considerable amount of ions present to add to conductivity. As a rule, the more porous or fissured a rock and the more amount its groundwater content, the higher is the conductivity and the lower the resistivity.

If a water-bearing rock contains clay minerals, a relative large number of ions may be released from such minerals by ion exchange processes. The ions contributed by these processes add to normal ion content in pore water resulted in an increased conductivity. All rocks containing clay minerals (in wet state) exhibit abnormally high conductivity (Sharma, 1997).

Generally intact rocks are resistive, but many geological processes can alter a rock and significantly lower its resistivity. Dissolutions, faulting, shearing, columnar jointing, weathering, and hydrothermal alteration usually increase porosity and fluid permeability, and hence lower the resistivity. In contrast, precipitation of calcium carbonate or silica reduces porosity and hence increases the resistivity. Hardening of a rock by compaction and/or metamorphism will reduce porosity and permeability, and therefore increase the resistivity.

Resistivity is, therefore, an extremely variable parameter, not only from formation to formation but within a particular formation. As a result, knowledge of typical resistivity values for different types of subsurface materials and the geology of the area surveyed is important to interpret resistivity tomograms obtained from resistivity surveys. The resistivity of common rocks and soil materials (Keller and Frischknecht, 1966; Daniels and Albery, 1966; Telford et al., 1990) is shown in Figure 3.7.

From a geophysical perspective, the Pointe du Hoc site contains a great amount of cultural clutter in the form of steel, concrete and void spaces associated with craters and tunnels, bunkers, etc. The presence of these cultural features complicates reliable geological interpretation of the resistivity profiles and renders electrical geophysics a challenging prospect. Nevertheless, resistivity tomography remains the most appropriate geophysical technique for studying geological cliff stability at Pointe du Hoc.

Resistivity tomography, as described above, provides a smoothed image of the distribution of bulk electrical resistivity $\rho(\mathbf{r})$ beneath the survey site. Electrical resistivity is of interest to geological stability studies since it provides an important indication of lithology and bulk physical properties of rock formations such as porosity and fracture density. These quantities also control the bulk strength of the rock formation and hence the mass movement potential. Resistivity tomograms also respond to variations in groundwater salinity (Singha and Gorelick, 2005) which leads to ambiguities since salinity and rock strength are not strongly coupled. A reliable geotechnical interpretation

of the resistivity tomograms is challenging since it requires a good understanding of how to convert electrical resistivity into the bulk properties that affect the cliff stability.

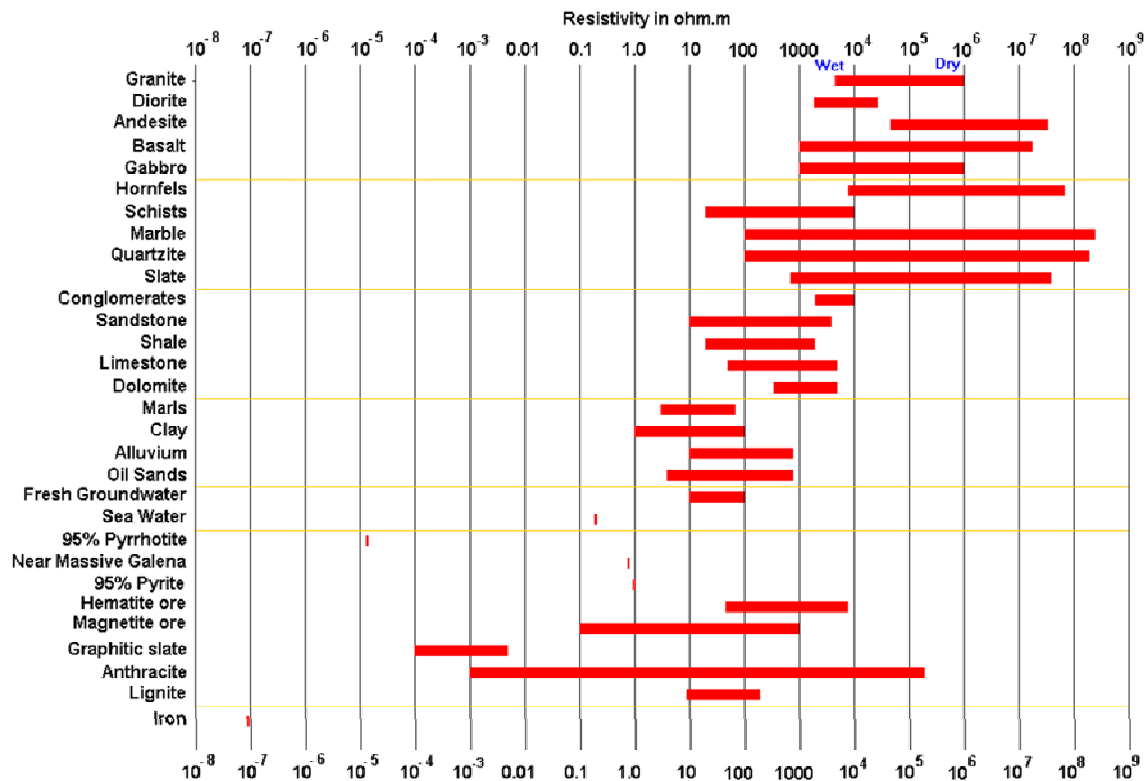


Figure 3.7. Typical ranges of electrical resistivities of Earth materials. From Loke (2004).

Resistivity of Carbonate Rocks

Geotechnical interpretation of resistivity tomograms is more problematic in carbonate terrains than in sandstones. Purely siliciclastic rock units such as clean, unfractured sandstones typically exhibit a fairly regular intergranular, or primary, porosity that developed as the original sediment compacted and lithified. The pore space in such rocks usually forms an interconnected network with open intergranular spaces that are connected by clear throats. A well-sorted sandstone of this type has a high permeability.

In clean unfractured sandstones characterized by water saturation S_w and porosity ϕ , the traditional Archie's law (Archie, 1942)

$$\sigma = \sigma_w S_w^n \phi^m \quad (3.20)$$

has long been used by petrophysicists within the petroleum industry to reliably describe the bulk electrical conductivity σ , using exponents $m = n = 2$. The constant n is referred to as saturation exponent and m is a constant for a particular rock type and usually referred to as the cementation factor. The quantity $\sigma_w \sim 0.3\text{--}1.0$ S/m (Keller and Frischknecht, 1966) is the electrical conductivity of the pore (connate) water, which is controlled by the salinity, or more generally the total dissolved solids. Commonly in petrophysics, the formation factor $F = \sigma_w / \sigma$ for a fully water-saturated ($S_w^n = 1$) rock unit is defined. Since pore fluids are electrically conductive relative to the solid rock matrix, we have $\sigma_w > \sigma$ and hence $F > 1$, that is, the formation factor is greater than one. From Archie's law (equation (3.20)), for a fully-saturated rock we see that the formation factor is related to porosity by $F \sim \phi^{-m}$.

Clay minerals originating from secondary diagenetic processes can coat the sand grains and clog the pore throats, reducing the permeability. In marly, or shaly, sandstones that have significant clay content, Waxman and Smits (1968) provide an important modification to Archie's formula for predicting bulk conductivity. Clay minerals have an inherent negative surface charge which contributes an additional electrical conduction pathway that is not found in clean sandstones. Thus, clay-bearing formations generally have a considerably higher bulk electrical conductivity than clean sandstones.

Carbonate rock units commonly exhibit secondary porosity, such as moldic vugs caused by anhydrite dissolution of fossil remains, which develop after the rock is formed. The secondary porosity can carry a considerable fraction of the permeability. The bulk permeability depends strongly on whether the vugs are separate or touching each other (Lucia, 1983). It is very difficult to make an assessment from studying outcrops and drilled core samples about the role of vugs in shaping the bulk hydrogeological behavior of a carbonate formation. Furthermore, the range of

intergranular textures found in carbonate rocks varies greatly from coarser grain-dominated to finer mud-dominated fabrics. Representative examples of intergranular and vuggy carbonate textures are shown in Figure 3.8 and Figure 3.9, respectively.

In carbonates, the relationship between electrical resistivity and porosity is quite complicated (Summers, 2006). Archie's law has limited predictive value in carbonates as the m value can vary widely (Sen et al., 1997) and it is difficult to ascertain for a given formation (Focke and Munn, 1987). Cementation exponent values as high as $m \sim 4-7$ have been observed in Middle East oil reservoirs. Asquith (1995) has noted that large values of m are associated with higher separate-vug porosities, while a lower m value is associated with touching-vug porosity, such as fractures.

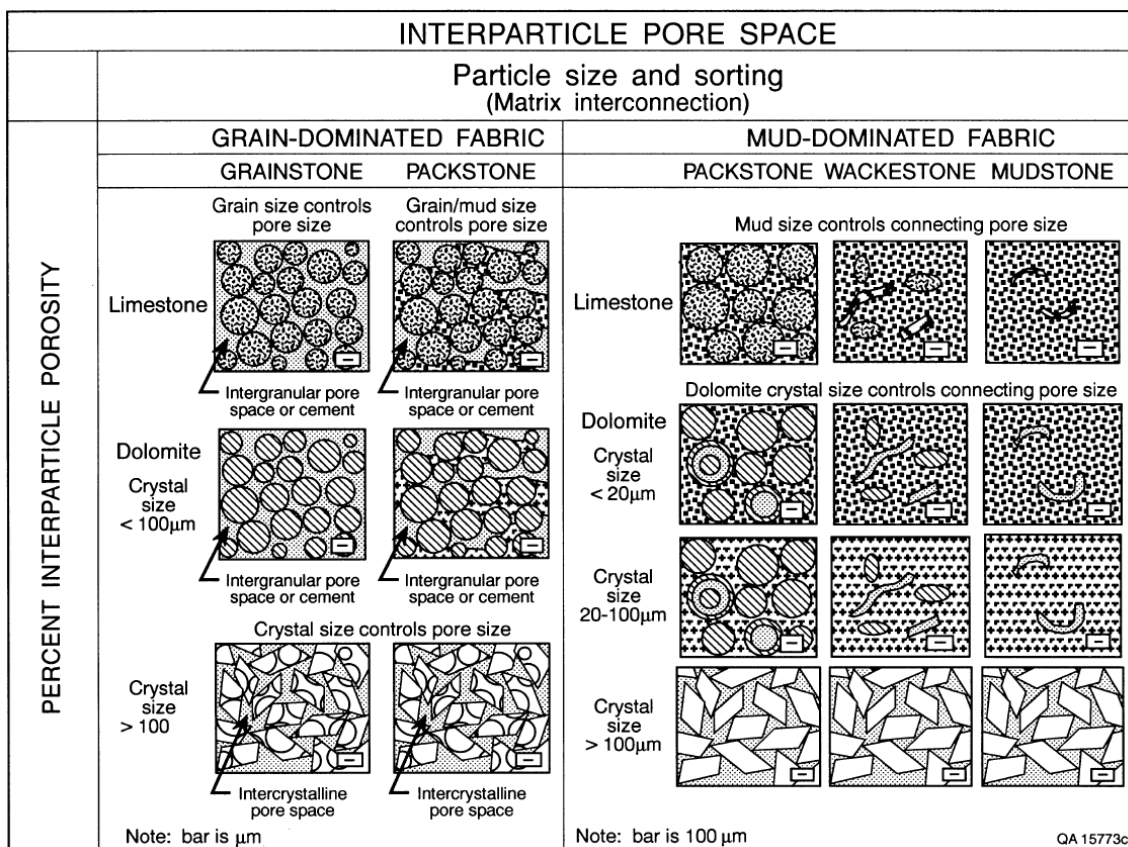


Figure 3.8. Classification of intergranular texture in carbonate rocks. From Lucia (1995).




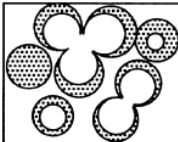
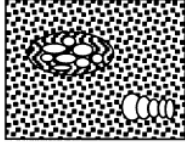
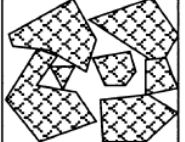
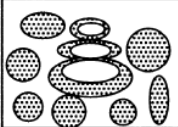

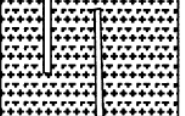
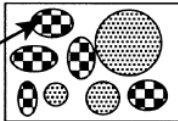

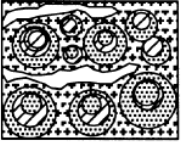
VUGGY PORE SPACE			
SEPARATE-VUG PORES (VUG-TO-MATRIX-TO-VUG CONNECTION)			TOUCHING-VUG PORES (VUG-TO-VUG CONNECTION)
PERCENT SEPARATE-VUG POROSITY	GRAIN-DOMINATED FABRIC	MUD-DOMINATED FABRIC	GRAIN- AND MUD-DOMINATED FABRICS
	EXAMPLE TYPES	EXAMPLE TYPES	EXAMPLE TYPES
	<p>Moldic pores</p> 	<p>Moldic pores</p> 	<p>Cavernous</p> 
	<p>Composite moldic pores</p> 	<p>Intrafossil pores</p> 	<p>Breccia</p> 
	<p>Intrafossil pores</p> 	<p>Shelter pores</p> 	<p>Fractures</p> 
	<p>Intragranular microporosity</p> 		<p>Solution-enlarged fractures</p> 
			<p>Fenestral</p> 

Figure 3.9. Classification of vuggy texture in carbonate rocks. From Lucia (1995).

Much effort has been spent in the petroleum industry applying Archie's law to reservoir rocks. Keller and Frischknecht (1966) report formation factors of $F \sim 0.6 \phi^{-2.0}$ for clean sandstones and $F \sim 1.7 \phi^{-1.6}$ for shaly sandstones. However, for oolitic (bioclastic) limestones, the formation factor varies wildly. Petrophysicists working in the petroleum industry are mainly interested in primary porosity since potential hydrocarbons reside in

the primary pore space. However, from our geotechnical perspective, we are more interested in the secondary porosity of the carbonate formations at Pointe du Hoc since touching vugs and fractures largely control the bulk strength of the cliffs.

The stratigraphy at Pointe du Hoc beneath the Quaternary cover shows calcarenite, possibly Plio–Pleistocene in origin, above the Jurassic unit of fractured limestone and hard sandstones (Chapter II). The basal unit is the grey marly limestone. The calcarenite at the top of the Calcaire de St. Pierre du Mont formation is likely to be somewhat indurated due to its subaerial exposure during the Plio–Pleistocene as the carbonate platform episodically emerged above and submerged below sea level. The resulting mixed carbonate–siliciclastic system likely has predominantly an intergranular porosity which is appropriately described by $m = 2$.

Beneath the calcarenite–dominated strata, there are Bathonian layers of fractured limestone and hard sandstones. The hard sandstones, unless fractured, can also be described by an Archie cementation exponent of $m = 2$. The limestones are classed as bioclastic (Riout et al., 1991) which implies that they are constructed of fossil debris and probably contain isolated moldic vugs so that $m > 2$. Fractured limestone, on the other hand, is characterized by a secondary porosity that falls into the category of touching vugs, and hence $m < 2$ is appropriate. In general, for the purposes of this study we assign the m values recommended by Asquith (1995) for the various units found in the Pointe du Hoc stratigraphic sequence. These are indicated in Table 3.1.

Table 3.1. Cementation exponent m values as a function of carbonate porosity type, Pointe du Hoc sequence.

Porosity type	m value	Pointe du Hoc rock type
intergranular	$m = 2$	calcarenite; hard sandstone; marl; loess
isolated vugs	$m > 2$	unfractured bioclastic limestone
fractures	$m < 2$	fractured bioclastic limestone

CHAPTER IV

DATA ACQUISITION AND ANALYSIS

This chapter describes the details of ERT data acquisition and analysis used in this study. The ERT data comprise a network of electrode profiles acquired at the 2006 reconnaissance and the 2008 high-resolution phases. The data analysis comprises 2-D and 3-D tomographic inversions in the presence of extreme topography and dense cultural clutter.

DATA ACQUISITION

The 2006 and 2008 data were collected using the multi-electrode resistivity system, SUPER STING™ R8 IP Earth Resistivity/IP Meter manufactured by Advanced Geosciences, Inc. (<http://www.agiusa.com>) (Figure 4.1). The system permits simultaneous deployment of up to hundreds of electrodes, with unlimited roll-along capability to add 14 additional electrodes at a time to a single profile. Switching the electrodes to serve as current or voltage pairs is done automatically in the computer interface to the resistivity system. Any or all sequences and combinations can be pre-programmed by the system operator prior to field data acquisition. The SUPER STING™ instrument permits specification of the Schlumberger and dipole-dipole arrays, for example, plus less conventional user-defined configurations. We found good results by programming the manufacturer-suggested hybrid dipole-dipole-Schlumberger array measurement protocol which combines the good depth of penetration of the Schlumberger array with the superior lateral resolution of the dipole-dipole array.

A general 2-D profile acquisition of the resistivity data is fairly straightforward. The stainless steel electrodes are driven into the ground with a small sledgehammer at a regular interval. Electrode locations are established by a tape measure draped across the field topography. The staked-in electrodes are then connected via spring assemblies to take-outs located along special-purpose cable segments joined end to end. Each cable segment can accommodate 14 electrodes. The fully assembled cable is then connected to

the console which is plugged in to a 12-volt dc marine battery. Figure 4.1 shows electrode and cable installation for a 2-D resistivity data acquisition.

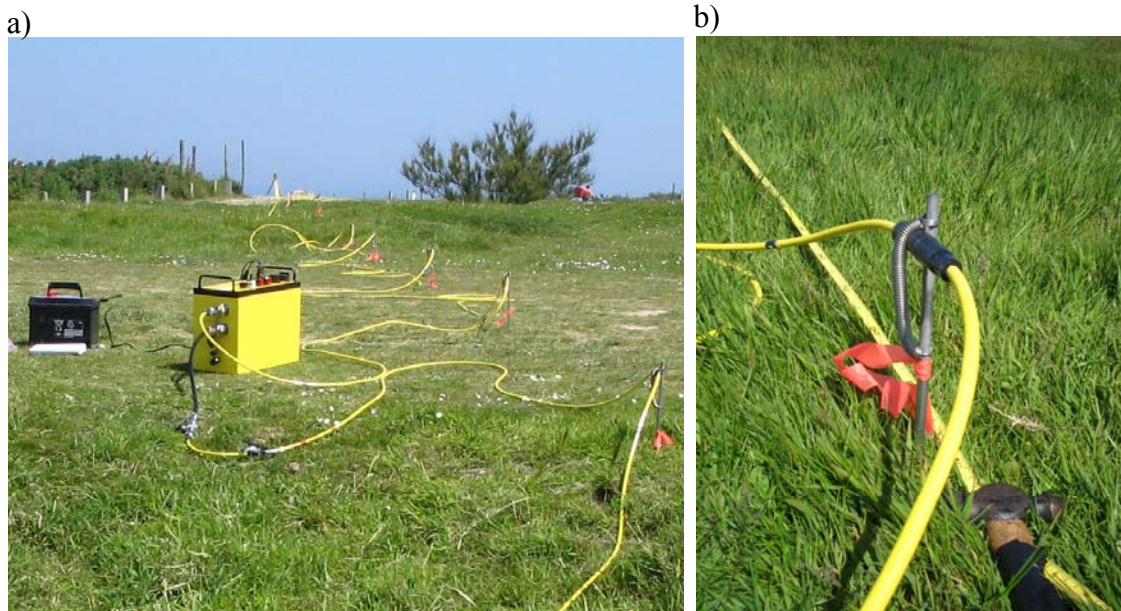


Figure 4.1. Equipment set up. (a) Multi-electrode resistivity SUPER STING™ R8 IP meter connected to a 12-volts battery, electrodes, and cables. (b) A close-up view of an electrode connected to a cable take out.

The horizontal electrode interval distance is significantly different than the tape-measure value if the resistivity survey line is draped over irregular terrain such as the steep cliffs, bomb craters, or an outcropping concrete fortification. A Topcon GTS-313 total station surveying instrument was used to measure the electrode horizontal distance, with respect to the start of the line, as well as the elevation of each electrode. The Topcon system was also used to position each resistivity line within the Pointe du Hoc coordinate system.

The extreme topography of the site required special access to the Pointe du Hoc cliffside. This was facilitated by setting up a releasable rappel system utilizing existing fence posts, historical concrete fragments and installing equalized pickets as anchors. The benefit of a releasable rappel system being used rather than a single fixed

line for the researcher to rappel on is that if an accident were to happen or if it were necessary for a rescuer or a second person to descend, the primary researcher could be lowered to the beach or a second person could rappel down to provide assistance. The techniques and technology utilized in this system are common practice in the high angle rescue and recreational climbing guiding fields. Jason Kurten, a professional member of the Texas A&M University staff, and the Indoor Climbing Facility Manager at the Department of Recreational Sports, oversaw the setup and use of all roped activities and cliffside work. Figure 4.2 shows a sample of the cliffside electrode installation that required roped access. The cable, electrodes, and tape measured were brought down with the rock climber during the first time of descending, and then the electrodes were staked in the cliff face and hooked up to the cable on the way up. Once the rock climber ascended up to the top side, the other portion of the electrode line on the topside was then set up and ready for the console to take the data measurement. The rock climber had to descend again to recover the electrodes once the measurement was complete, and the console was switched off.

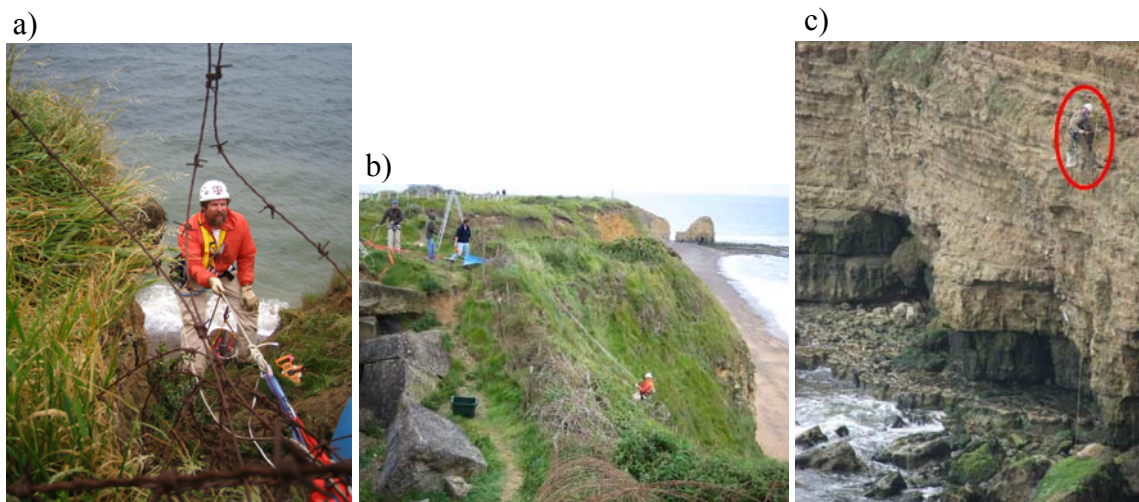


Figure 4.2. Cliffside electrode installation. (a) Rock-climbing researcher preparing to descend; the orange cords in the foreground are connected to a triply-redundant anchoring system; (b) and (c) cliffside electrode installation using the releasable rappel rope-climbing apparatus. Note that the electrodes are kept in the white work bucket which can be seen in all photos.

The cliffside electrodes are extremely valuable since they permit some of the current injection and collection points to be located on a vertical boundary of the solution domain. This situation is very rarely attained in geophysics. Conventionally, electrodes can be deployed only on the top surface of the site to be characterized. The cliffside injection points therefore allow unique electric current pathways through the subsurface. In general, electric current pathways from surface-deployed electrodes originate and terminate at the surface. With cliffside electrodes, the pathways may originate and/or terminate on lower strata within the geological section and in such cases hence the electric current is not as affected by surficial structure such as the Quaternary soil cover. These pathways therefore provide an opportunity for the direct energization of the Mesozoic rocks without having to go through a “Quaternary soil filter.”

The objective of the 2006 reconnaissance data acquisition stage was to obtain overall subsurface information at the site while in the 2008 phase the details stability data at the two at-risk buildings (the Observation and the Rudder’s Command Posts) were acquired. Although both 2006 and 2008 phases of the data acquisition used the same acquisition strategy as described above, some acquisition parameters were slightly different. The details of the data acquisition are described as follows.

2006 Reconnaissance Dataset

In June 2006, during the reconnaissance ERT data acquisition stage, 18 electrical resistivity profiles over the Pointe du Hoc site were collected. Ten profiles, enumerated TOP-1 through TOP-10 were on the top side of the site; two profiles, enumerated OBS-1 and OBS-2 were at the observation post building area; and six profiles, enumerated CLF-1 through CLF-6 were draped over the cliff edge with significant portions extending onto the near-vertical cliff face. Figure 4.3 shows a sketch of these survey lines over the aerial view of the site.

At this stage 56 electrodes connected to 4 cables were employed with the roll-along technique. Data acquisition parameters used for the 2006 datasets, number of electrodes, electrode spacing, and number of roll-along are provided in Table 4.1. Using

the hybrid dipole-dipole-Schlumberger electrode array for 56 electrodes, the data measurement time takes ~ 1.5 h plus another ~ 45 min for a roll-along. This time does not include electrodes and cables laying out time which is ~ 1 h plus ~ 20 min for moving and reinstalling an electrode cable for a roll-along measurement. This is for each topside line. The cliffside lines which require rope access take considerably longer.

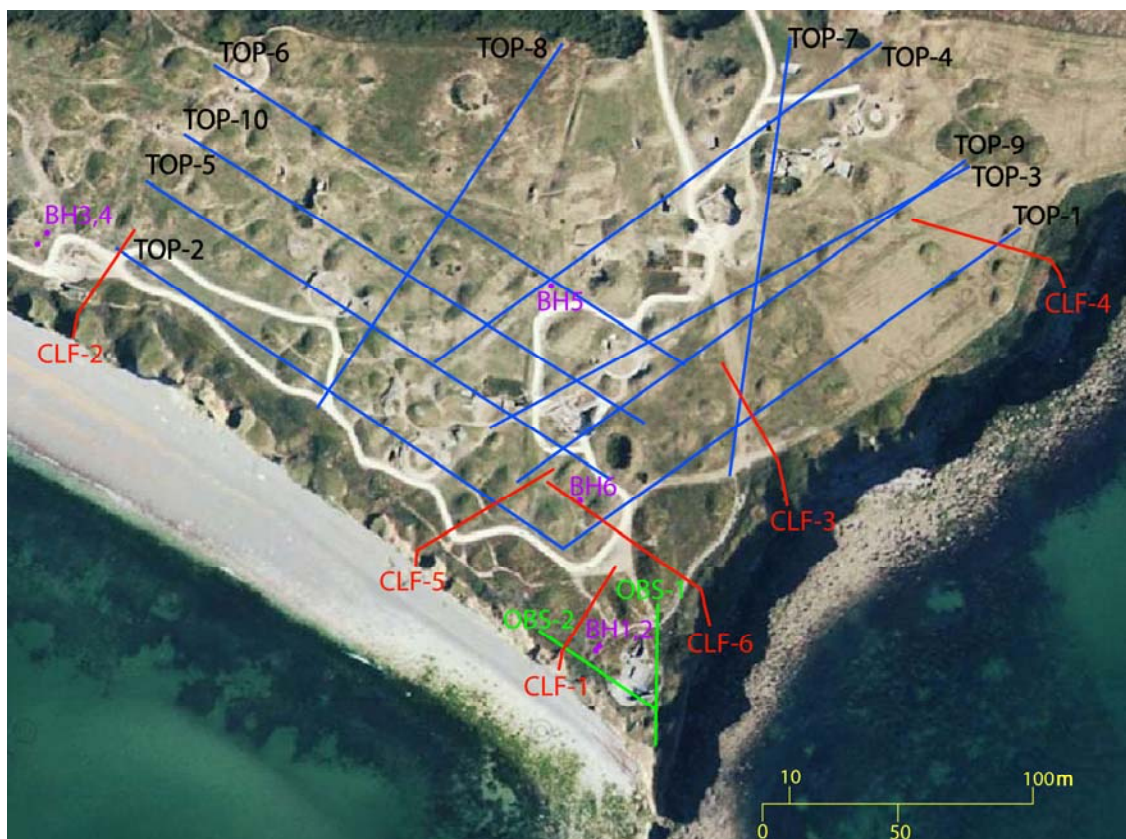


Figure 4.3. Pointe du Hoc reconnaissance-phase 2006 geophysical site map showing approximate locations of topside resistivity lines (blue), cliffside resistivity lines (red) and observation post resistivity lines (green), and borehole locations (purple dots). The start of each top side and observation post line are not marked, while the end of each line is marked by its line name. The start of the cliffside line is marked by its line name but the end of each line is not marked.

Table 4.1. Acquisition geometry for 2006 reconnaissance-phase dataset.

2-D survey line	Electrode spacing (m)	No. of electrodes	No. of roll-along
TOP-1	3.0	70	1
TOP-2	3.0	70	1
TOP-3	3.0	70	1
TOP-4	3.0	70	1
TOP-5	3.0	84	2
TOP-6	3.0	70	1
TOP-7	3.0	56	0
TOP-8	3.0	56	0
TOP-9	3.0	70	1
TOP-10	3.0	70	1
CLF-1	1.0	56	0
CLF-2	1.0	56	0
CLF-3	1.0	70	1
CLF-4	1.0	70	1
CLF-5	1.0	84	2
CLF-6	1.0	98	3
OBS-1	1.0	56	0
OBS -2	1.0	56	0

The electrode positioning technique was crude in the 2006 stage. Using the Topcon system, the horizontal position and elevation of the electrodes along each profile was found by triangulating between the total station and at least three known control points whose coordinates had been previously established by traversing. However, the elevations of the electrodes staked directly on the cliff face could not be determined due to lack of line-of-sight from the cliff top since the total station were not lowered to the beach. At this stage, it was assumed that the slope of the cliff face was constant 4:1 (see Figure 4.4) and that the electrodes were planted along the same azimuth as the topside portion of the profile and at 1.0 m uniform tape-measure distance from each other. This assumption however led to systematic error for later data analysis since the electrode positions were somewhat mislocated. As a consequence, electrodes positioned in the cliff face of the data acquired in the 2008 high resolution phase were determined with a greatly improved technique.

Note that the spacing between 2-D resistivity lines of the 2006 dataset is too coarse for the size of the survey area, which when combined into a 3-D dataset resulted in a 3-D resistivity tomogram which provides poor horizontal resolution information of the detailed subsurface resistivity near the critical at-risk buildings. This became the focus of the 2008 high-resolution survey. Nevertheless the 2006 dataset was very useful for overall rapid site assessment.

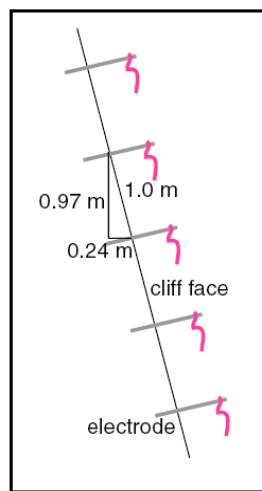


Figure 4.4. Assumed 4:1 slope geometry of the 2006 electrodes installed in the cliff face.

2008 High Resolution Dataset

Based on experience gathered during the 2006 reconnaissance data acquisition stage, a comprehensive suite of high resolution measurements in March 2008 was acquired at the site. Two high-resolution resistivity surveys were acquired in 2008 in the vicinities of the Observation Post and Rudder's Command Post (eastern anti-aircraft building), respectively. The resistivity data were acquired using the same multi-electrode system with the same strategy placing electrodes both on the topside and over the cliff edge and with an irregular line pattern. The 2008 datasets have substantially higher line-density (~3-4 m line spacing) than the 2006 dataset. A total number of 42 electrodes with 2 m spacing attached to 3 cables for each resistivity line without a roll-

along were employed. Only 3-cable electrode lines were sufficiently to cover the smaller subsurface area of the two at-risk buildings. Unlike in 2006, longer lines were needed in order to cover the overall site. Using the hybrid dipole-dipole-Schlumberger electrode array for 42 electrodes, the data measurement time takes ~ 70 min. The electrodes and cables laying out time is ~ 45 min for each topside line. The cliffside lines, of course, require much longer time.

The Topcon total station surveying instrument was employed again in 2008 to determine electrode elevations and horizontal locations, but to a much greater precision than was accomplished during the 2006 campaign. Using this navigation technology, electrode positions and heights were determined to ~ 0.2 m precision. In order to achieve this level of accuracy, 5 control points over the site were first established by traversing. Another 16 resection points were later added up during the survey. As a result a temporary control network of 21 points was established (Figure 4.5). The control points, some of which were located on the beach, were distributed around the site so that every point on the site could be seen by at least one of the control points. The positions of the control points, relative to each other, were accurately determined by traversing and resection of the network. This is a standard land surveying procedure. Total station navigation of the electrode locations is preferred to GPS or other navigation approaches because of its high accuracy and simplicity.

At the Observation Post (OP) area, we acquired 37 resistivity lines, enumerated OP-4 through OP-41, of which 32 are topside lines while five are cliffside lines that required roped access. The location of the OP resistivity lines is shown in Figure 4.6. The resistivity lines cover the area around, behind, and in front of the OP as well as the surrounding cliff faces. Some of the lines, for example OP-37 and OP-38, are bent around the OP so as to be very sensitive to the geological structure directly underneath it. In general, an excellent spatial coverage of the target area has been achieved. The resulting tomographic images provide valuable constraints on the underlying subsurface resistivity distribution. Note that Cliffside lines OP-40 and OP-41 have certain electrode points in common. The two lines fan out topside from a shared string of electrodes

draped over the cliff. The fan geometry, using shared electrodes, was utilized to take best advantage of the time-consuming cliffside electrode deployment.

At the Rudder's Command Post (RCP) area, we acquired 14 resistivity profiles, enumerated RCP-1 through RCP-14, of which six are topside lines and eight are cliffside lines that required roped access. The location of the RCP resistivity lines is shown in Figure 4.7. Note that some of the cliffside resistivity lines also fan out from shared electrode points draped over the cliff. The tomographic coverage at RCP is not as complete as the OP survey due to the fact that OP was identified as the highest-priority structure; nevertheless a good spatial coverage of the RCP target area has been achieved.



Figure 4.5. Total-station temporary control point network used for locating electrode positions in the 2008 data acquisition phase. Overall site control points are in red while additional control points for the Observation Post and Rudder's Command Post areas are in green.



Figure 4.6. Pointe du Hoc 2008 OP geophysical site map showing locations of topside resistivity lines (red), cliffside resistivity lines and other lines that required roped access (yellow) at the OP area. Green dots are borehole locations acquired in 2008 by the geotechnical team. The start of each line is marked by the blue numbers, while the end of each line is marked by the black numbers.

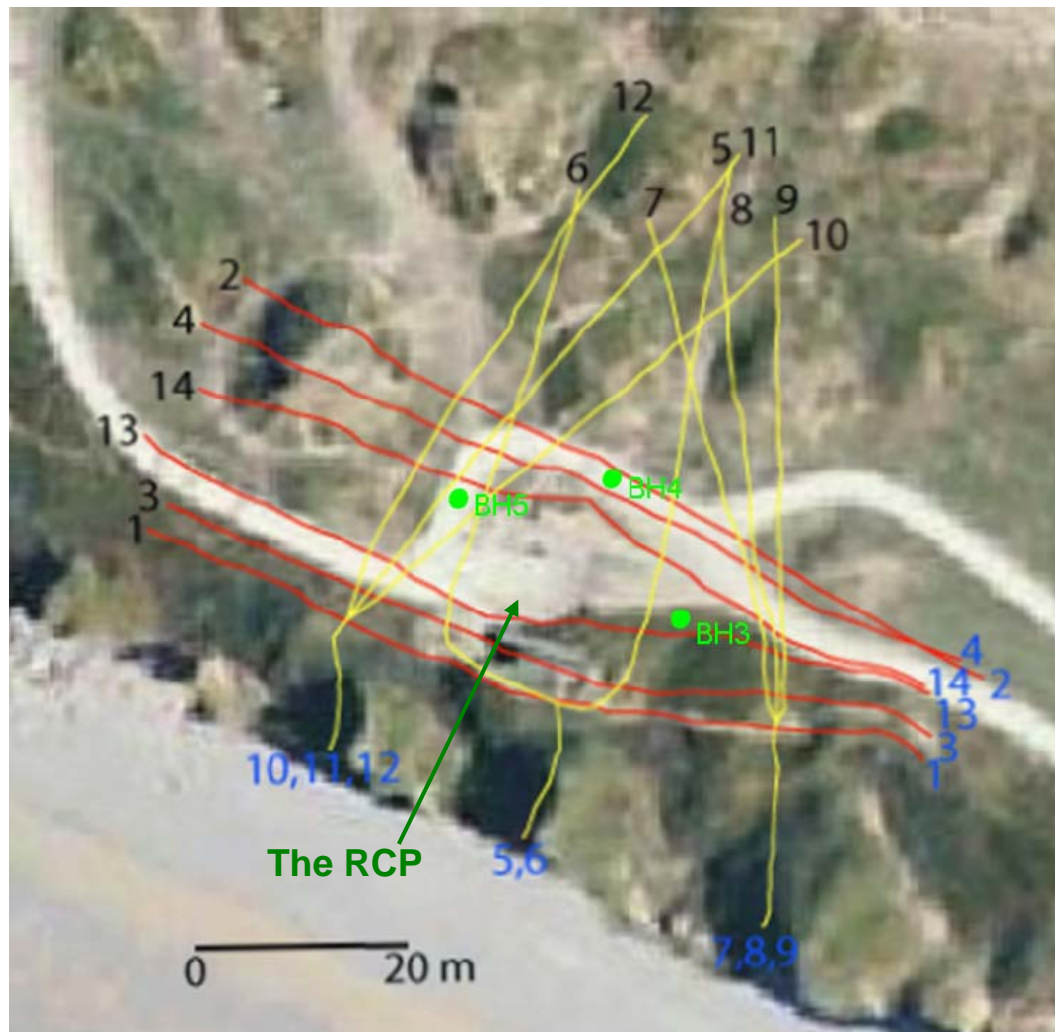


Figure 4.7. Pointe du Hoc 2008 RCP geophysical site map showing locations of topside resistivity lines (red), cliffside resistivity lines and other lines that required roped access (yellow) at the RCP area. Green dots are borehole locations acquired in 2008 by the geotechnical team. The start of each line is marked by the blue numbers, while the end of each line is marked by the black numbers.

DATA ANALYSIS

2-D Analysis

The 2-D data analysis, in this study was needed to be done prior to the 3-D analysis due to the data were acquired in a 2-D approach. Data quality control such as pseudosection plotting to remove bad data points and data format preparation was done

in the 2–D analysis stage before combining to a 3–D dataset. 2–D resistivity inversion profiles are important to constrain subsurface information on the vertical planes under the survey lines and provide overall subsurface resistivity distribution of the site along with the 3–D inversion result.

The initial step of 2–D electrical resistivity data analysis is to establish a digital terrain model of each survey profile. The terrain file is needed for construction of 2–D resistivity tomograms that incorporate topography. The horizontal distance and elevation of each electrode from the total station survey is needed. From this information, the total horizontal length of each profile is determined. The next step is to perform quality control on the measured apparent resistivity data by pseudosection plotting. Bad data points normally stand out as points with unusually high or low or negative values on the pseudosection and they must be removed. A poor quality datum may be caused by a number of factors such as poor ground coupling of an electrode, faulty connections of cables/electrodes, excessive windy or rainy conditions, or low battery. Figure 4.8 shows examples of poor and high quality data. Note that for the 2008 OP dataset, line OP13 was discarded and not considered further in the geophysical analysis due to very poor data quality. After the apparent resistivity data have been edited, data with its digital terrain file is inverted to generate a 2–D resistivity tomogram.

For 2006 data, the AGI *EarthImager 2D* inversion software was initially used for pseudosection plotting, data editing, and inversion. However as the CLF–1 profile was inverted, it was found that the *EarthImager 2D* software did not handle well the extreme terrain associated with the cliff–draped electrodes. Figure 4.9 shows the CLF–1 pseudosection and inversion as determined by the *EarthImager 2D* program. As can be seen in Figure 4.9c, the software treats the cliff–face in the same manner as the surface topography, using a single terrain file, and hence the forward modeling finite–element mesh becomes heavily distorted at the cliff face. The AGI software cannot handle greater than 45° slopes on the terrain.

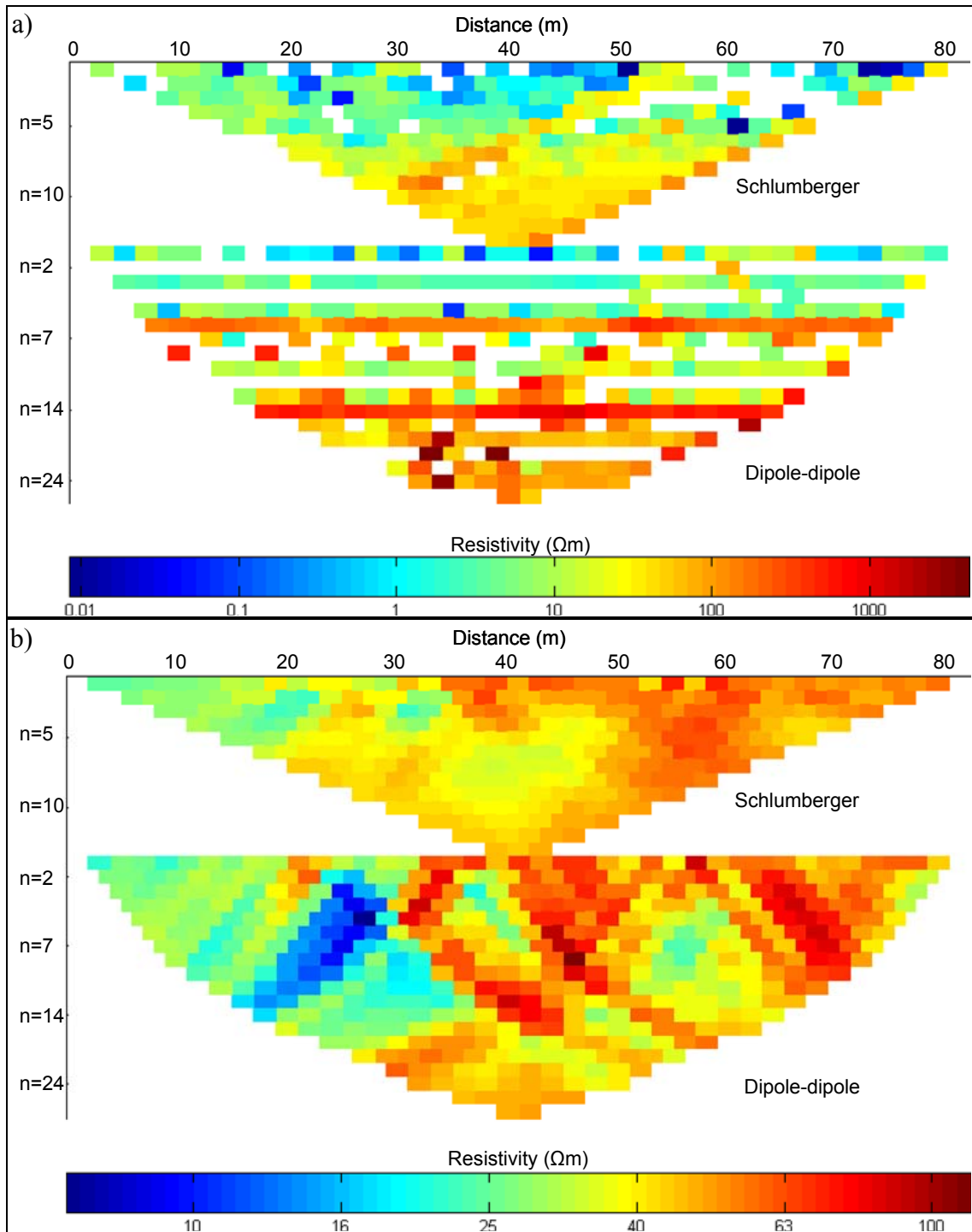


Figure 4.8. Apparent resistivity pseudosections from Schlumberger and dipole-dipole electrode configuration. (a) Example of poor data quality; line OP-13. Note that blank spots are negative apparent resistivity data points that have been removed. (b) Example of high data quality; line OP-25.

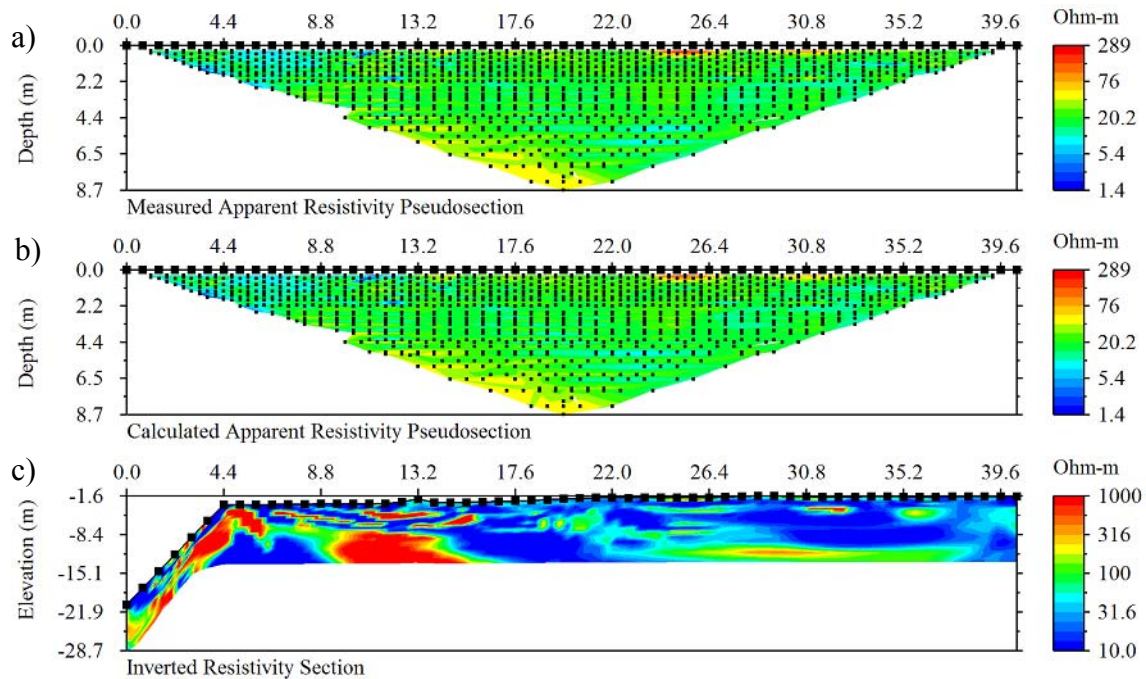


Figure 4.9. Resistivity pseudosections and 2-D inversion section with extreme topography of CLF-1 profile using AGI *EarthImager 2D* inversion software. (a) Measured apparent resistivity pseudosection, (b) calculated apparent resistivity pseudosection, and (c) inverted resistivity section.

A more powerful software package, BERT (Boundless Electrical Resistivity Tomography) based on the inversion method described in Günther et al. (2006) and the finite element modeling techniques described in Rücker et al. (2006) works well with the extreme topography of the cliffs at Pointe du Hoc. The program is under development, open source, and available free of charge for academic research (<http://resistivity.net>). BERT is a 3-D program which contains a 2-D module which is used for data inversion in this study. Figure 4.10 shows the CLF-1 pseudosections (measured and calculated) and the inversion result using BERT program. As can be seen in Figure 4.10c the inverted data from BERT program provides a far better 2-D resistivity tomographic image of the extreme cliff topography of the CLF-1 profile (compare to Figure 4.9c). Consequently, the BERT program was chosen to invert the topside and the extreme terrain of the cliff-face resistivity profiles for both datasets of 2006 and 2008.

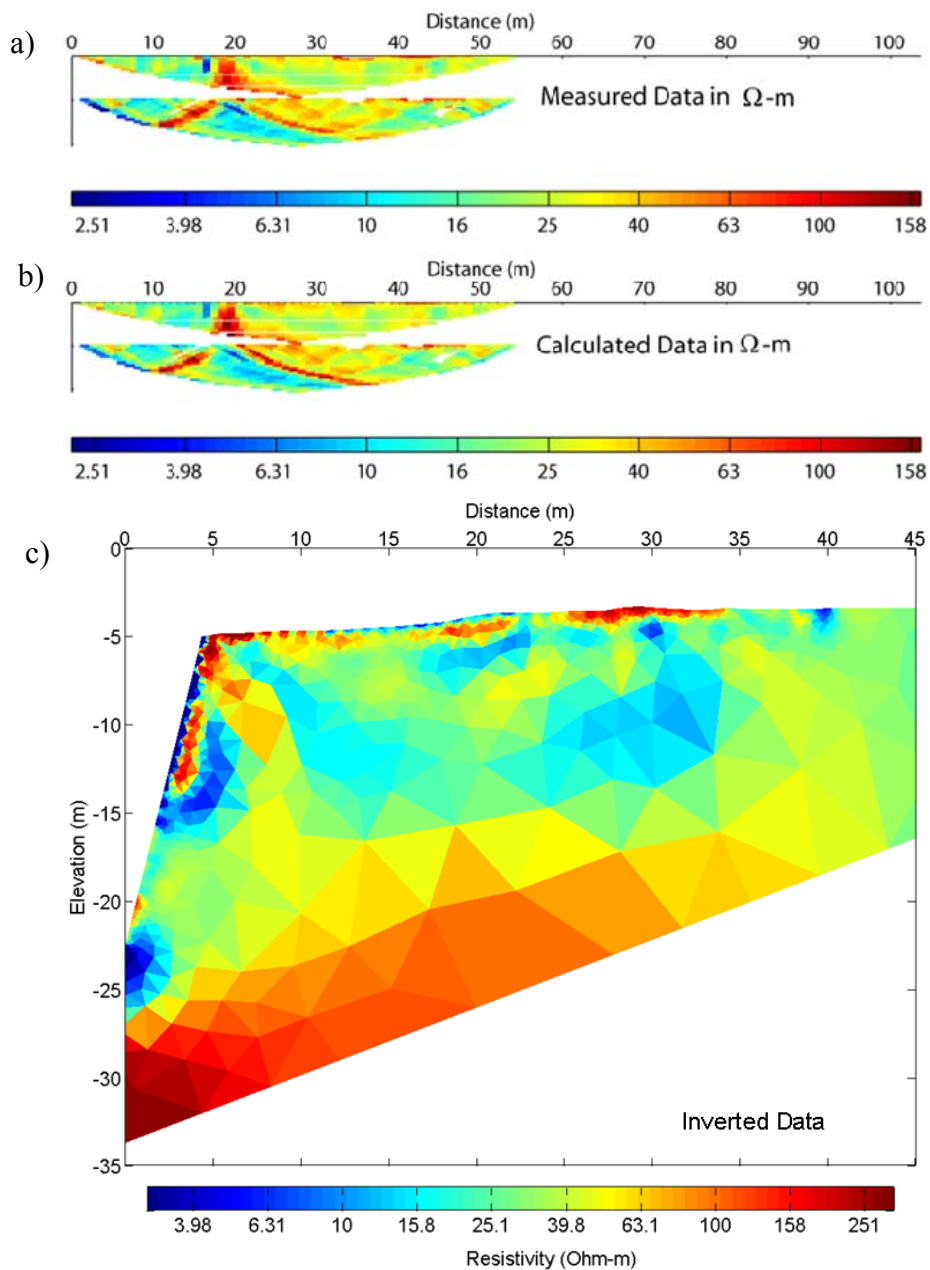


Figure 4.10. Resistivity pseudosections and 2-D inversion section with extreme topography of CLF-1 profile using BERT 2-D inversion program. (a) Measured apparent resistivity pseudosection, (b) calculated apparent resistivity pseudosection, and (c) inverted resistivity section. Note that the top panel of each pseudosection is of Schlumberger array, and the bottom one is of dipole-dipole array.

BERT is a part of the software library DCFEMLib – Direct Current Finite Element Method Library. It is currently under developed and will be incorporated into GIMLi – Generalized Inversion and Modeling Library. The latter is a much more general approach for arbitrary tomographic methods. As its functionality expands, BERT migrate to GIMLi. DCFEMLib is licensed under the LGPL (Lesser General Public License). BERT is aimed to be used among academic research community with no charge. As a research-grade package under development, it is not just a simple click and run tool like AGI EarthImager or other commercial inversion software packages. The complete package comprises executables for ERT modeling and inversion, tools for generating mesh input (the so-called poly-tools) and tools for applying the mesh generator.

BERT is available under Linux and Windows operating system, either from pre-compiled binaries or self-compiled code. See <http://resistivity.net> for information about how to obtain the binaries/codes or to compile the code. Since BERT is controlled on the command line, Windows users need a shell environment as well. It is recommended that MSYS – Minimal SYStem (<http://www.mingw.org>) which is a very small but nice Linux-like system is used. MSYS provides a POSIX (Portable Open Source Interface) compatible Bourne shell environment, with a small collection of UNIX command line tools. It is primarily developed as a means to execute the configure scripts and Makefiles used to build Open Source software, but also useful as a general purpose command line interface to replace Windows cmd.exe.

For the 2-D data inversion in this study, BERT was installed on Windows under the Linux-like environment system, Cygwin (<http://cygwin.com>) with the help of Dr. Thomas Günther of the Leibniz Institute of Applied Geosciences in Hannover, Germany one of the authors of the BERT program. The 2-D inversion problem in this study is relatively small so that it ran smoothly on a PC Windows system with 4GB RAM, and an Intel[®] CPU T2400 dual-core processor of 1.83 GHz. The numbers of input apparent resistivity data points using the Schlumberger-dipole-dipole protocol for 98, 84, 70, 56,

and 42-electrode profiles are ~4600, ~3600, ~ 2800, ~2000, and ~1200, respectively. An average CPU run time for each 2-D inversion profile is ~10 minutes.

Before using BERT it is required that the data file is converted from AGI STING format (filename.stg) to the unified resistivity.net format (filename.ohm) (see <http://resistivity.net?unidata>). This is easily done using DC2DInvRes (graphical FD-based inversion software also available on <http://resistivity.net>). The DC2dInvRes software is also used to plot apparent pseudosections and to remove bad data points. After data editing, the data file plus the terrain file together can be converted and saved to the required data format (filename.ohm) and input for 2-D data inversion program BERT.

To visualize the output resistivity models, inverted data, calculated data, topographic effects, corrected data, data misfits along, with the raw data, a MATLAB tool box (postBERT2d) is used. The MATLAB tool box is kindly supported by Dr. Thomas Günther. Figure 4.11 shows an example of output profiles plotted by postBERT2d. The data is from the 2008 dataset line OP-9. Figure 4.11a is the raw apparent resistivity pseudosection. Figure 4.11b is the topographic effect (t) to appraise geometry effects of each data point (equation (3.14)). $t = 1$ means the measurement is not affected by topography. $t > 1$ refers to increased apparent resistivity whereas $t < 1$ indicate a decrease. Figure 4.11c is the data corrected for the topographic effect. Figure 4.11d is the apparent pseudosection calculated from the inversion result by the forward modeling. Figure 4.11e is the data misfit in term of % difference between the corrected and the calculated data. Figure 4.11f is the inversion result.

The inversion result of each 2-D profile can be adjusted by changing parameters such as regularization and mesh quality parameters. The input parameters are written in an Ascii configuration file (inv.cfg) which it can be easily modified. After the configuration file is edited, BERT can be rerun with the new inversion parameters. In this study each 2-D profile of the 2006 dataset was inverted using the same regularization and mesh quality parameters but with slightly differences in lower and upper bounds of the model resistivity due to each profile contains different bound of

measured apparent resistivity values. For the 2008 dataset only selected approximately straight 2-D profiles were inverted using the same regularization and mesh quality parameters as those of the 2006 dataset. The bent resistivity lines were not inverted since by 2-D resistivity inversion theory, the survey line should be straight to yield ideal subsurface resistivity information under the vertical plane of the survey line. Nevertheless the bent profiles provide additional data coverage for the 3-D inversion. The inversion configuration file and values of each parameter for the 2-D data analysis is shown in Appendix A.

Note that the regularization parameter (λ) controls the strengths of the smoothness constraints and thus defines how smooth the inversion result will be. Lower values of λ produces models which better fit the data but yield small-scale resistivity structure that is not required by the data. On the other hand higher values of λ produces models with less fit the data but smoothes out necessary resistivity structure. Also note that generally, all meshes must be fine near the electrodes (to achieve high accuracy in the forward calculation and because the resolution is high there) and coarse at the boundaries. The higher the quality is, the more accurate are the results but with an increasing number of nodes and thus run-time. Thus a trade-off between accuracy and run-time has to be considered.

3-D Analysis

To construct a 3-D resistivity dataset from 2-D data, the edited 2-D profiles with bad data points removed must be combined together. In this study three 3-D resistivity datasets were obtained, namely the 2006, the 2008 OP, and the 2008 RCP datasets.

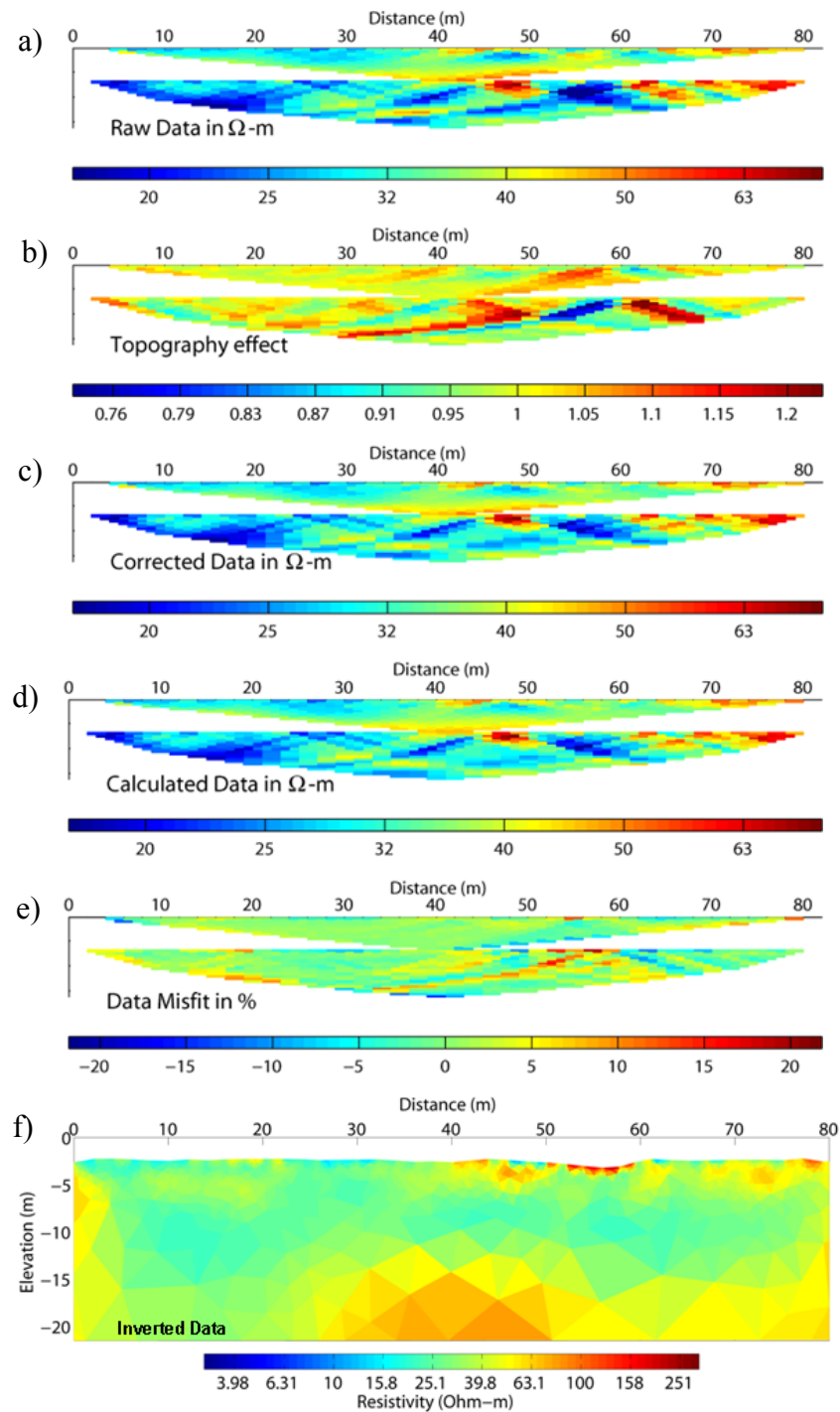


Figure 4.11. Resistivity pseudosections and 2-D inversion section of the 2008 dataset line OP-9 using BERT 2-D inversion program and plotting by postBERT2d MATLAB package. Note that the top panel of each pseudosection is of Schlumberger array, and the bottom one is of dipole-dipole array.

All the edited 2-D data files were obtained and converted into unified resistivity.net format (filename.ohm) by using DC2DInvRes as explained in the previous section, are combined using DC3DInvRes to get a 3-D data file for each survey area. Once the 3-D data files were obtained, the next step is to establish a fully 3-D digital topographic model of each survey area as it is needed for producing any 3-D resistivity tomograms. The digital topographic models for each datasets are achieved using the electrode positions obtained from the Topcon total-station navigation as previously described along with terrestrial laser-scanning data of the site acquired by the Texas A&M historical architecture team.

Laser scanning technique has been widely used to remotely record complex 3-D objects. The technique is referred to as LIDAR (Light Detection and Ranging) which emits pulses of laser light and measures the time difference between emission and reception of reflected signal. The result of each measurement is a 3-D coordinate point in space, much like the total station survey but with greater speed of acquisition time. A laser scanning instrument can gather thousands of points per second where a total station may gather only one point per second. As a result, the output for a laser scanner is a cloud of points so dense that a realistic, dimensionally-correct 3-D version of the object being measured can be visualized (Warden et al., 2007).

The laser scanning data obtained from the historical architecture team were acquired in 2006 and 2008 during the time of the geophysical surveys. The data were taken using a Riegl terrestrial laser scanner capable of recording 8,000 points of data per second, with 1 cm distance accuracy at distances to 800 m. These data were made available to us to be used for the 3-D resistivity inversion by Prof. Warden in the form of an (x, y, z) point cloud with the origin $(0, 0, 0)$ coordinate at the center of the site (Figure 4.12). This point cloud however contains not only ground surface points but also all scanned objects points above the ground such as buildings, people, trees, bushes, fences, and etc. These above ground points have to be removed since they will later cause unrealistic subsurface resistivity structure within the 3-D resistivity tomograms. Electrode positions (x_E, y_E, z_E) are obtained from the Topcon total station navigation as

described earlier. The horizontal electrode coordinates (x_E, y_E) are rotated into the same frame of reference used by the laser scanner. This is readily accomplished since there are typically some points in common between the laser scanner and the total station datasets. Once the electrode horizontal coordinates (x_E, y_E) have been brought into the laser-scanning frame, the vertical electrode coordinates z_E are then shifted to match the laser scanning data. Finally, the vertical coordinates z_E of electrodes require a final minor adjustment so that they are positioned on the topographic surface, instead of suspended in air or buried in the earth. This procedure was done separately for each 3-D dataset.

The laser scanner works on a line-of-sight principle, so overall site coverage depends on where the laser scanner has been set up. There may be certain areas of the site such as the bottom of deep bomb craters that do not have coverage. Fortunately, many of these bomb craters were occupied by resistivity lines so that the vertical coordinates z_E of the electrodes located inside the bomb craters are available from the total station data. These electrode heights are added to the digital topographic model to provide a rough indication of the topography in areas hidden from the laser scanner (Figure 4.12). The x-y boundary and number of topographic points used for the three 3-D datasets are presented in Table 4.2.

The 3-D data file of each survey area and its digital terrain model (containing 3 text columns of x, y, and z values) were input files for the inversion program BERT. In this 3-D case, the inverse problem is sufficiently large so that BERT cannot be used on the Windows PC. Instead the BERT program was installed and compiled on a more powerful Linux system consisting of 16 GB RAM, and 8 dual-core AMD Opteron™ 8218 processors each working at 2.6 GHz. The kind assistance of Dr. Thomas Günther was provided to set up the job.

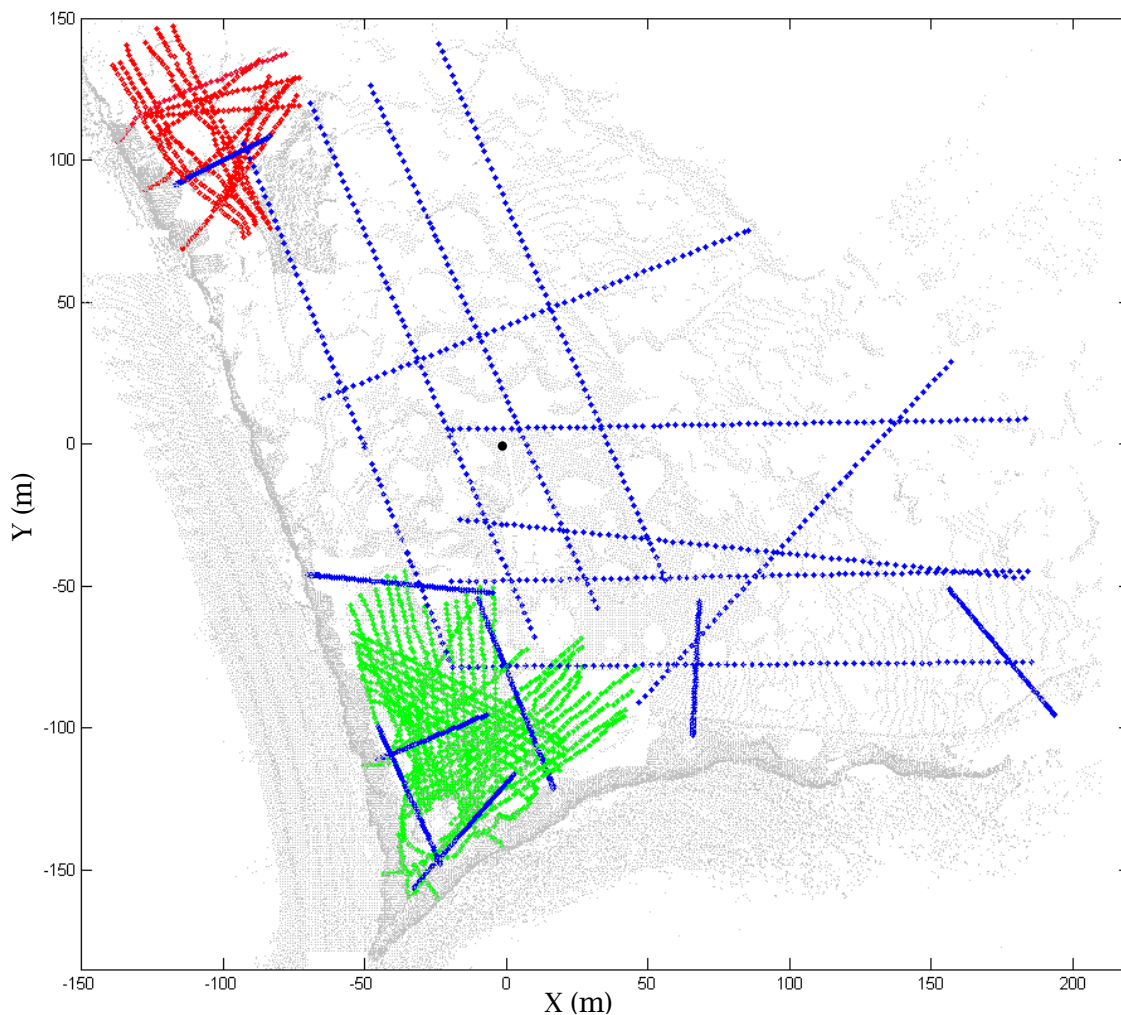


Figure 4.12. Laser scanning cloud points and electrode points. A selection of the horizontal (x, y) points from the over all Pointe du Hoc laser scans are shown in grey. Electrode locations of 2006 data are shown in blue. Electrode locations of 2008 OP data are shown in green. Electrode locations of 2008 RCP data are shown in red. The black dot is the coordinate origin $(0, 0, 0)$. The white blank areas are gaps in the laser-scanning coverage due to deep bomb craters or areas of above ground points that have been removed.

Table 4.2. X–y boundary and number of terrain points used for digital topographic models.

Dataset	x–boundary (m)	y–boundary (m)	No. of terrain points
2006	–150 to 210	–185 to 155	73,140
2008 OP	–70 to 50	–185 to –40	21,932
2008 RCP	–165 to –60	60 to 150	11,863

The first step in BERT is mesh generation. The general procedure is first to create a surface mesh; next to interpolate heights from topographic model; then to make a small (inversion mesh) and a large (forward modeling mesh) box around it with a refinement, if necessary; and finally to create the tetrahedral mesh using Tetgen (a module in BERT), a free and versatile mesh generator as described in Rucker et al. (2006).

For specifying topography, there are two different approaches; (i) the electrodes in the data file have an elevation and all other points are interpolated; (ii) or a digital elevation model or at least a list of measured points is used. Whereas the first case is sufficient for smooth topography and/or dense electrode coverage, the latter is more general. The topographic points, being assembled in a 3-column file containing x , y , and z , are Delaunay triangulated (Shewchuk, 2002) such that no point is inside the circumcircle of any triangle in the mesh system. For every point of the meshes, also the electrodes, the elevation is linearly interpolated. Therefore electrodes with measured elevations should be included in the digital terrain file as well to make sure their z values lie on the final topographic surface.

Once the mesh has been generated and adjusted, it can be viewed using ParaView (<http://www.paraview.org>), a sophisticated free tool for 3-D (and 2-D) visualization. Figure 4.13, 4.14, and 4.15 show the final meshes used for data inversion of the 3-D datasets.

Due to the great complexity of the computations, to reduce wasted effort it is advisable to perform a few trial runs on a coarse mesh to make sure all input parameters are correctly specified, before making a final production run on the full mesh. The higher mesh quality may be used. However as noted in 2-D analysis, the higher the quality is, the more accurate are the results but with an increasing number of nodes and thus run-time. Thus a trade-off between accuracy and run-time has to be considered.

Once the optimized mesh is obtained, the next step in BERT is to run the full inversion with default input parameters applied. The result is a 3-D inversion tomogram which can be visualized using ParaView. From this step, it may become obvious that the

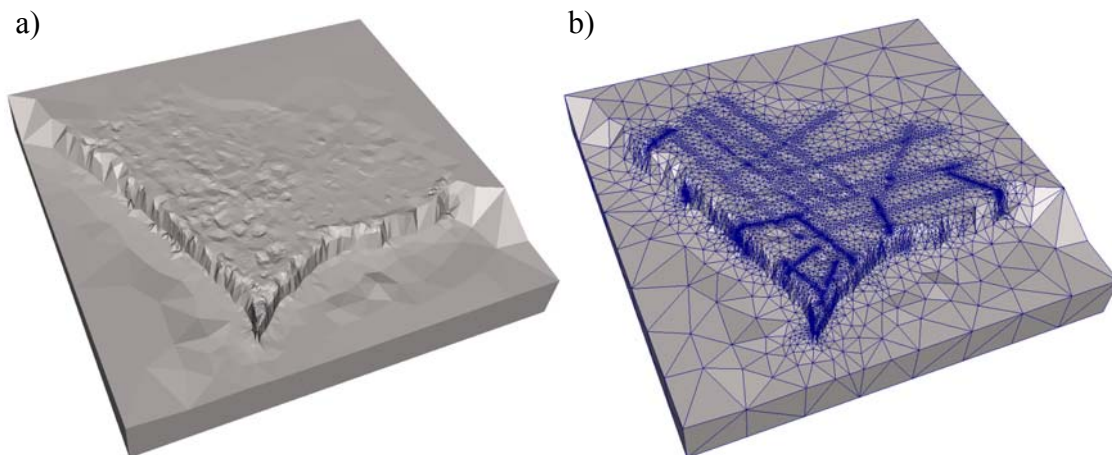


Figure 4.13. 3–D surface topographic model and mesh for 2006 dataset. (a) Overall surface topographic model of Pointe du Hoc area and (b) mesh over the topographic model. Note finer mesh in the vicinity of electrode locations.

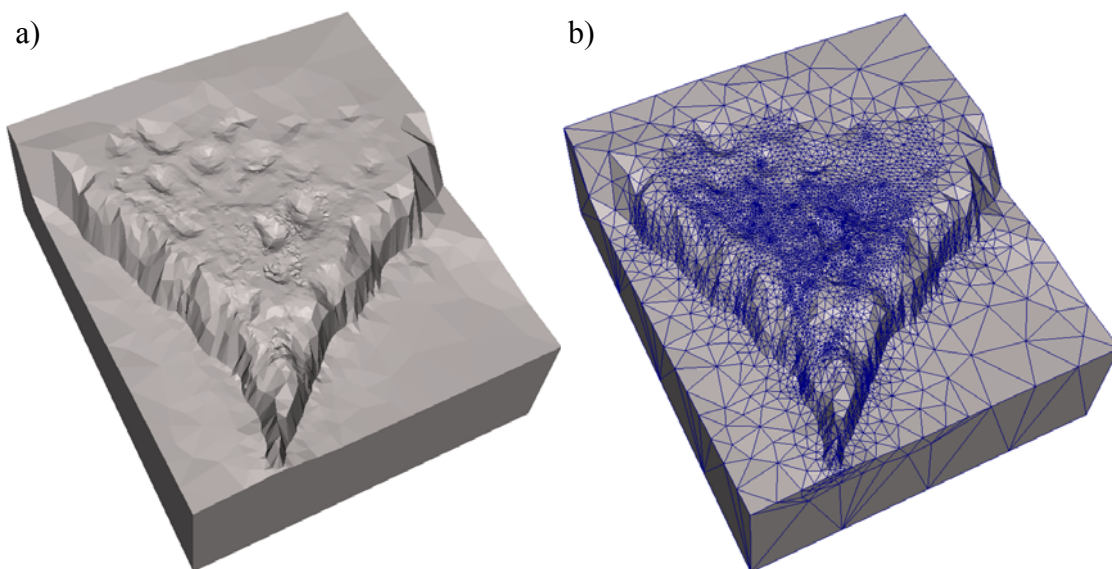


Figure 4.14. 3–D surface topographic model and mesh for 2008 OP dataset. (a) Surface topographic model around the OP and (b) mesh over the topographic model. Note very fine mesh on the top of the cliff due to good electrode coverage.

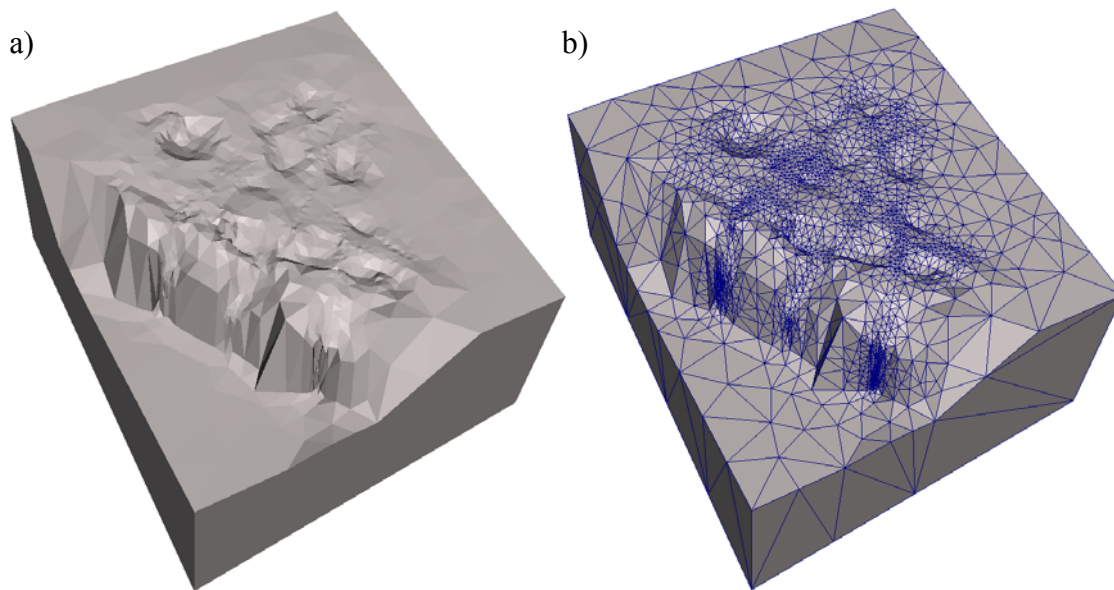


Figure 4.15. 3–D surface topographic model and mesh for 2008 RCP dataset. (a) Surface topographic model around the RCP and (b) mesh over the topographic model. Note finer mesh in the vicinity of electrode locations.

regularization parameter λ requires some adjustment in order to smooth out unwarranted irregularities in the image. This is a standard but somewhat subjective procedure in geophysical inversion. After increasing or decreasing λ , the BERT code is then run again. Choosing a value for λ that is too large will result in a tomogram that is excessively smooth such that potentially important geological details are lost. Rough models with low λ tend to fit the data better than smooth models with large λ , but that is because rough models try to fit the scatter, as opposed to accommodating useful information. The amount of smoothing which should be applied is always a subjective choice but typically there is a wide range of acceptable values of λ for which the structure shown in the tomogram is robust and interpretable from a geological standpoint.

The 3–D inversion parameters used in BERT can be written as a text configuration file (`inv.cfg`). Such information for each dataset is shown in Appendix B. To be consistent all 3–D datasets were inverted using the same inversion parameters but may be different in only the upper bound and lower bound of resistivity models since

each datasets contained different measured apparent resistivity range. Numbers of data points, number of mesh nodes and computer run time of inversion for each dataset are summarized in Table 4.3.

Once BERT has completed the inversion, to the appropriate smoothness level, the resulting tomographic images of the subsurface resistivity distribution $\rho(\mathbf{r})$ are ready for detailed visualization and graphical post-processing. ParaView was used for 3-D visualization and examining 2-D horizontal and vertical slices. The ParaView software contains powerful tools for rotating, slicing, overlaying other data such as the laser scans, and performing numerous other graphical operations on the 3-D data volume. It is found that these tools are very useful for interpreting the resistivity tomograms in terms of cliff geostability since they enable us to look at the data from multiple perspectives and to cut away selected portions of the data volume in order to peer beneath the surface.

Table 4.3. Number of parameters used for full 3-D inversion in BERT.

Dataset	No. of profiles	No. of electrodes	No. of data points	No. of mesh nodes	CPU run time
2006	18	1,231	43,685	131, 719	~33 h
2008 OP	36	1,542	49,749	83,543	~28.5 h
2008 RCP	14	515	15,427	36,732	~13.5 h

I worked closely with Dr. Thomas Günther from the beginning of setting up and compiling the BERT code, preparing the data files until getting the inversion results done. At some points if there were any problems that the code could not work, Dr. Günther would kindly help remove the bugs and thus the code has been greatly improved. This is a contribution of BERT development.

CHAPTER V

DATA INTERPRETATION

In this chapter, the 3–D resistivity inversion results, e.g. resistivity tomograms, are presented and discussed. A geological interpretation is provided which is based on the 3–D tomograms that are constructed using the 2006, 2008 OP, and 2008 RCP datasets and incorporating borehole information.

From the discussion in Chapter III, it is clear that interpretation of resistivity tomograms in terms of mass movement hazard at Pointe du Hoc is challenging, especially in view of the strong lithological variations (loess, calcarenite, bioclastic limestone, marl, etc.) and dense cultural clutter that exist at the site. The geophysical data nonetheless provide important information about bulk subsurface resistivity which, as stated in Chapter III, is diagnostic of porosity, clay content, and water content. Resistivity tomography is worthwhile because this type of non–invasive, spatially contiguous subsurface information is difficult, if not impossible, to obtain in any other way.

The bulk resistivity information contained within the tomographic images is ambiguous relative to an interpretation of the mass movement hazard. For example, a low resistivity zone could be caused by the presence of either clay or groundwater, assuming that the measurements are not greatly affected by the near–surface cultural clutter such as reinforced concrete slabs. Fortunately, the ambiguity is lessened since both clay and groundwater contribute to a weakening of a rock mass as they are both commonly found within fractures and joints. On the other hand, a high resistivity zone in a tomogram could be caused by either an open vug, such as a fracture or a cavern, or a mass of intact rock. The former is associated with weak rock but the latter is characteristic of high strength.

The inherent ambiguities of resistivity tomogram interpretation must be kept in mind when a mass movement hazard assessment is attempted. Incorporation of auxiliary data, such as drill core or geophysical logs, can greatly reduce the inherent uncertainty

although these data are typically available at only one or a few discrete points. Several cores were taken by the Texas A&M geotechnical engineering team led by Prof. Jean-Louis Briaud during drilling at the site in June 2006 and March 2008. These cores provide important clues as to the nature of the fractures and the Earth materials filling the fractures.

A cursory inspection of a fractured calcarenite core segment from the Calcaire de St. Pierre du Mont formation (Figure 5.1) reveals the presence of two distinct types of fractures. One kind of fracture is open, dry, and contains weathered surfaces. The presence of weathering suggests that water is not being transmitted through this type of fracture. The other type of fracture is wet and filled with a yellowish-ochre clay; suggestive of active groundwater processes. These observations suggest that groundwater infiltration and circulation bypasses some of the fractures, leaving them open and dry. Much of the groundwater appears to flow preferentially within the wet, clay-filled fractures.

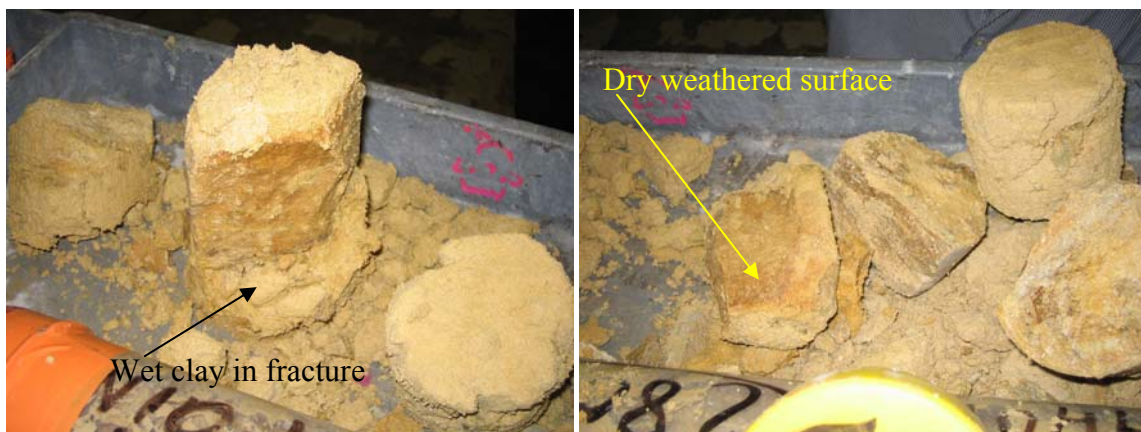


Figure 5.1. Photos of a fractured calcarenite core segment from the Calcaire de St. Pierre du Mont formation of Pointe du Hoc.

The overall strength of the cliff, and its susceptibility to failure, is affected by both types of fracture. It is known that major wedge failures at the top of the cliffs occur

after periods of heavy rainfall. The infiltration of precipitation and circulation of groundwater adds a dynamic loading to the wet, clay-filled fractures that can trigger their failure. In contrast, the open, dry fractures appear to be passive mechanical elements that respond to the slowly-changing, overall stress distribution within the cliff. The stress state of the cliff is largely unknown. The open, dry fractures do not participate in the active groundwater processes and consequently their failure is less predictable, but could occur at any time in the form of a catastrophic topple or rock fall. Nevertheless, for the purposes of this study we assume that the wet, clay-filled fractures are more likely to fail before the open, dry fractures. This is consistent with the general conclusions of Briaud et al. (2007, 2008) who emphasize the role of groundwater in the cliff failure mechanisms.

Accordingly, a simple conceptual basis for the geohazard interpretation of the resistivity tomograms, in which resistive zones are colored red and conductive zones are colored blue, is provided in Table 5.1.

Table 5.1. Resistivity tomography interpretation scheme.

Zone	Fracture regime	Mass movement potential
resistive (red)	dry, open	moderate
intermediate	intact rock mass	low
conductive (blue)	wet, clay-filled	high

INTERPRETATION OF 2006 DATA

The 3-D resistivity tomogram at the Pointe du Hoc site, based on all available 18 2-D profiles acquired in 2006 is shown in Figure 5.2. As shown by the color scale, the range of the resistivity values extends from $\log_{10} \rho = 0.00$ ($\rho = 1 \text{ } \Omega\text{m}$, shown in blue) to $\log_{10} \rho = 2.48$ ($\rho = 300 \text{ } \Omega\text{m}$, shown in red). Notice that much of the resistivity spatial variation seen in the tomogram is concentrated along the electrode lines (Figure 5.3). The resistivity of the intervening spaces between electrode lines is not well constrained by the tomographic image. This reflects the fact that the 3-D electrode line spacing was,

by necessity, too coarse for the size of the survey area. It would not have been feasible in a month field campaign to have acquired a sufficiently dense grid of measurements to completely span the site leaving no gaps in the tomogram. The root-mean-square (rms) error of the inversion result is $\sim 30\%$ which is relatively very high.

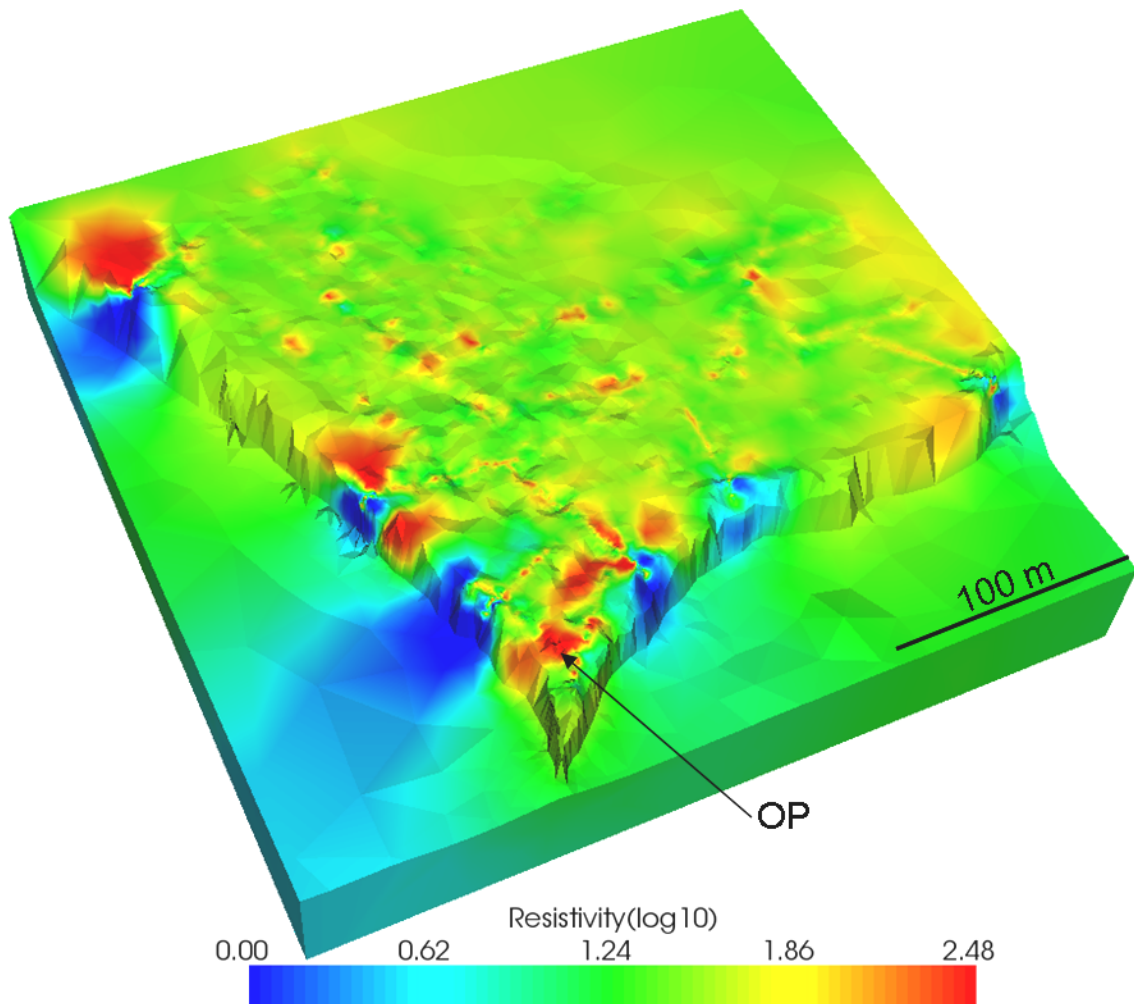


Figure 5.2. The 3-D resistivity tomogram produced from the 2006 dataset.

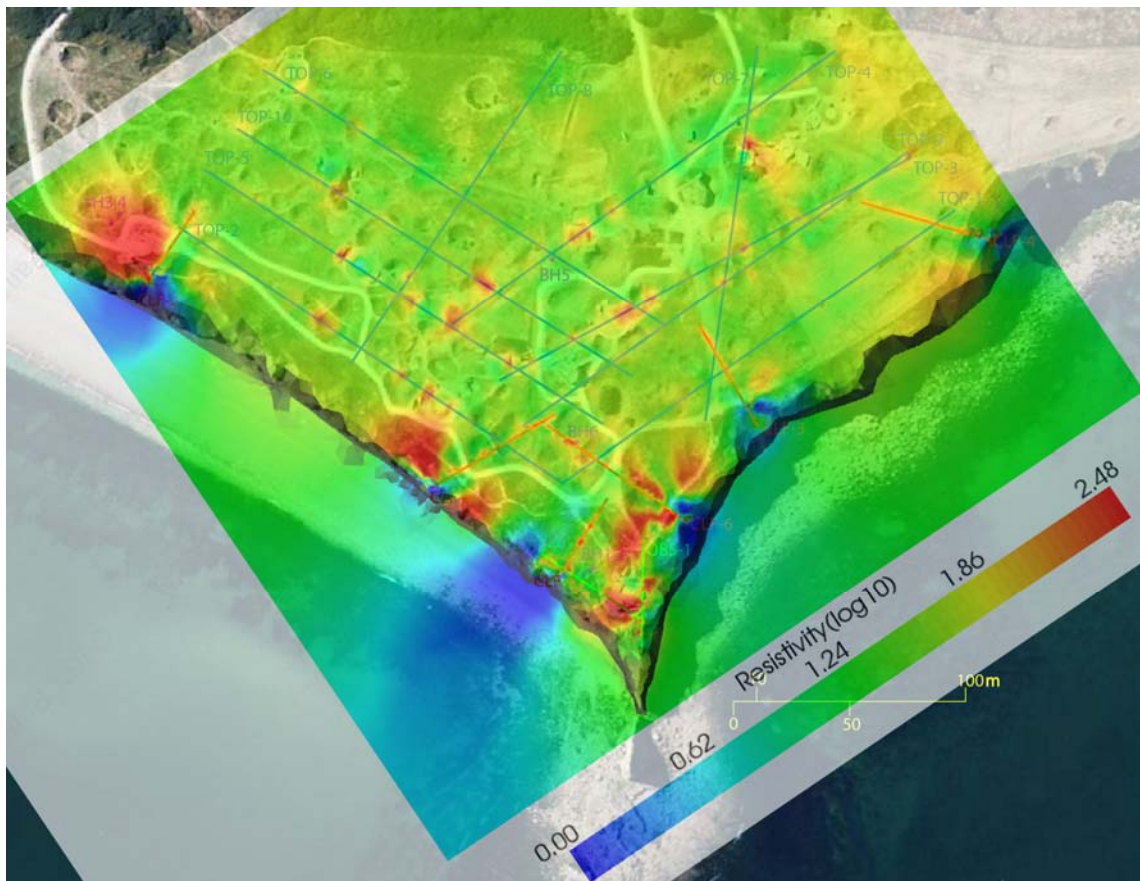


Figure 5.3. Top view of the 2006 3–D resistivity tomogram with resistivity lines on the site aerial photo.

Despite the large areas of the tomographic image that contain little resistivity information, there appear to be extreme subsurface resistivity anomalies that have been reliably imaged, especially in the proximity of the cliff edges. Foremost is the resistive (red region) zone in the vicinity of the observation post. This is likely caused by the cliffside OP building itself and dry, open fractures within the nearby rock mass. Notice that very low resistivity values (blue) are shown at the cliff face area at the beginning of each cliffside resistivity profile. The blue zones may indicate wet and/or clay-filled conductive areas of the cliff face which would constitute a high mass movement potential. Notice also other large resistive areas (orange to red zones) are located in the vicinity of the cliff side resistivity lines. These areas are more likely tomographic

artifacts caused by the interpolation of the smoothness constraints of the inversion model.

From a geophysical point of view, the main value of the 2006 3-D tomogram is that it shows a preliminary success of the 3-D resistivity inversion with extreme topography of the overall Pointe du Hoc area. However the tomogram provides only a rough indication of the subsurface resistivity information that is required for a detailed cliff stability assessment. As a result I do not consider the 3-D tomogram as a primary data set for the cliff stability assessment; nevertheless, 2-D resistivity tomograms still provide useful detailed information about the subsurface resistivity distribution within vertical planes beneath the data acquisition profiles. The validity of individual 2-D inversions is not affected by the line spacing between the various profiles that constitute a 3-D survey. Figure 5.4 shows an assembly view of all 2-D resistivity inversion profiles acquired in 2006. In general the top side resistivity tomograms show only a few blue areas, which suggest a moderate to low mass movement hazard. Above ~5–10 m, the small-scale blue and red zones of resistivity values are likely caused by loose electrode and ground couplings and cultural noise of steel, concrete, tunnels, and bunkers. Below ~5–10 m depth, the resistivity imaging suggests zones of dry silty clay layer underlain by fracture intact rock masses of limestone and sandstone. The highest mass movement potential is likely found on the cliffside profiles where clusters of blue resistivity zones are evident. Representative examples of 2-D topside resistivity tomograms are shown in Figure 5.5. Figure 5.6 shows representative examples of 2-D cliffside resistivity tomograms.

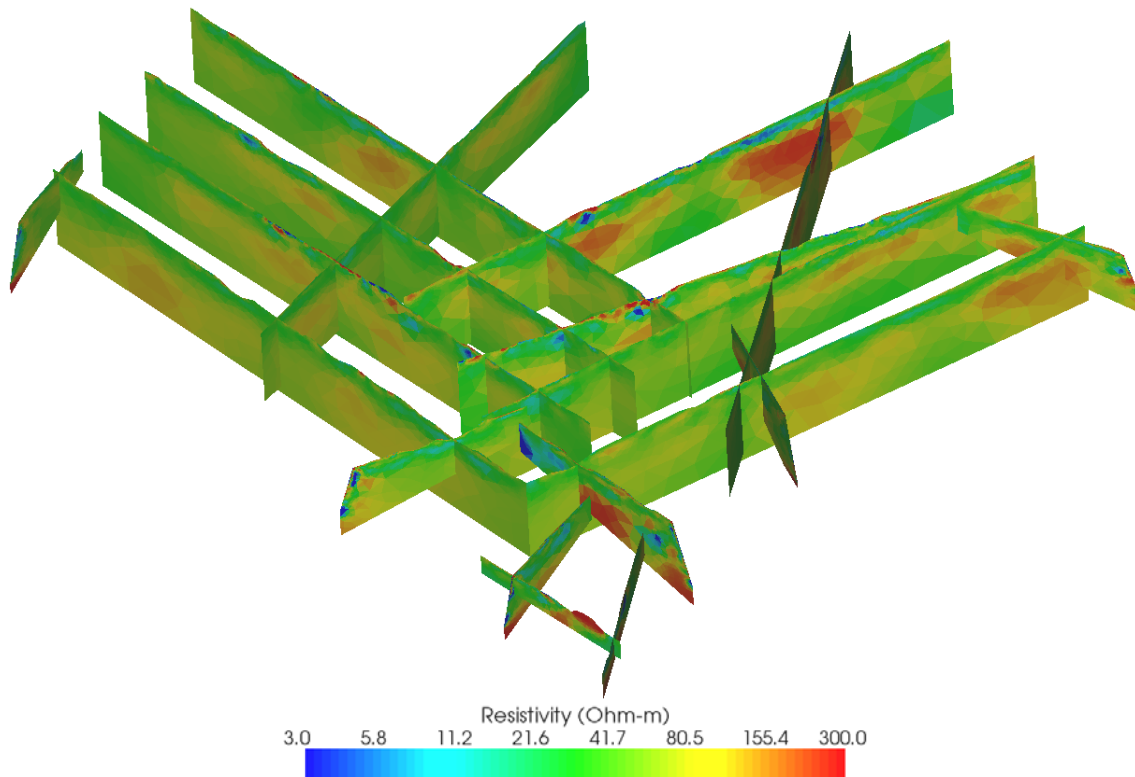


Figure 5.4. Fence diagram showing a perspective assembly of all 2-D subsurface distributions based on complete set of 2-D resistivity lines of the 2006 dataset. Note that the vertical depth of each profile is ~40 m.

INTERPRETATION OF 2008 OP DATA

Bird's-eye views of the 3-D resistivity tomogram that resulted from the 2008 OP geophysical survey are shown in Figure 5.7 (from a northeast perspective) and Figure 5.8 (from a northwest perspective). Figure 5.9 shows a top view of the 2008 OP tomogram along with the resistivity lines, both superimposed on an aerial photo of the site. As shown by the logarithmic color scales, the range of resistivity values extends from $\log_{10} \rho = 1.00$ ($\rho = 10 \text{ } \Omega\text{m}$, shown in blue) to $\log_{10} \rho = 2.3$ ($\rho = 200 \text{ } \Omega\text{m}$, shown in red). The blue colors correspond to relatively conductive Earth materials while the red colors refer to relatively resistive Earth materials. The total resistivity range of the tomogram, from 10–200 Ωm , is relatively modest. The intermediate resistivity value, shown in the green colors, is roughly $\log_{10} \rho = 1.65$ ($\rho \sim 45 \text{ } \Omega\text{m}$) which, according to

Figure 3.7, is intermediate between the bulk resistivity of clay ($<20 \Omega\text{m}$) and that of limestone ($>100 \Omega\text{m}$). Recall that the red colors are to be interpreted as zones containing mainly open, dry fractures and constitute a moderate mass movement hazard. The blue colors are to be interpreted as zones with largely wet, clay-filled fractures and constitute a high mass movement hazard. The green colors are interpreted as unfractured zones with a low mass movement hazard.

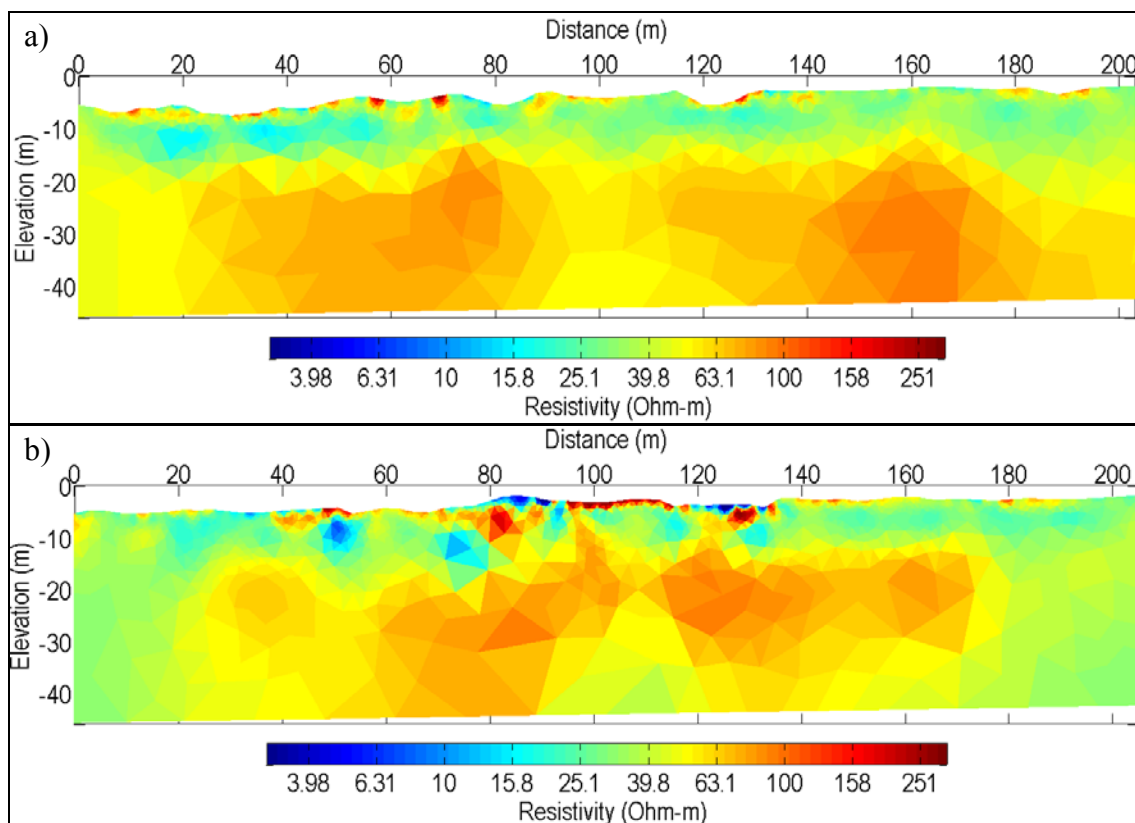


Figure 5.5. 2-D resistivity inversion profiles of some topside lines of 2006 dataset; (a) TOP-2, and (b) TOP-5. Note a layer of dry silty clay (light blue to green) underlain by fracture limestone and sandstone layers (yellow to orange) on the TOP-2 profile. On the TOP-5 profile is a good example of cultural noises such as concrete bunker and steel at distance 80–100 m and 120–140 m above ~10 m elevation. Below 10 m elevation is a layer of intact rock mass of sandstone and limestone.

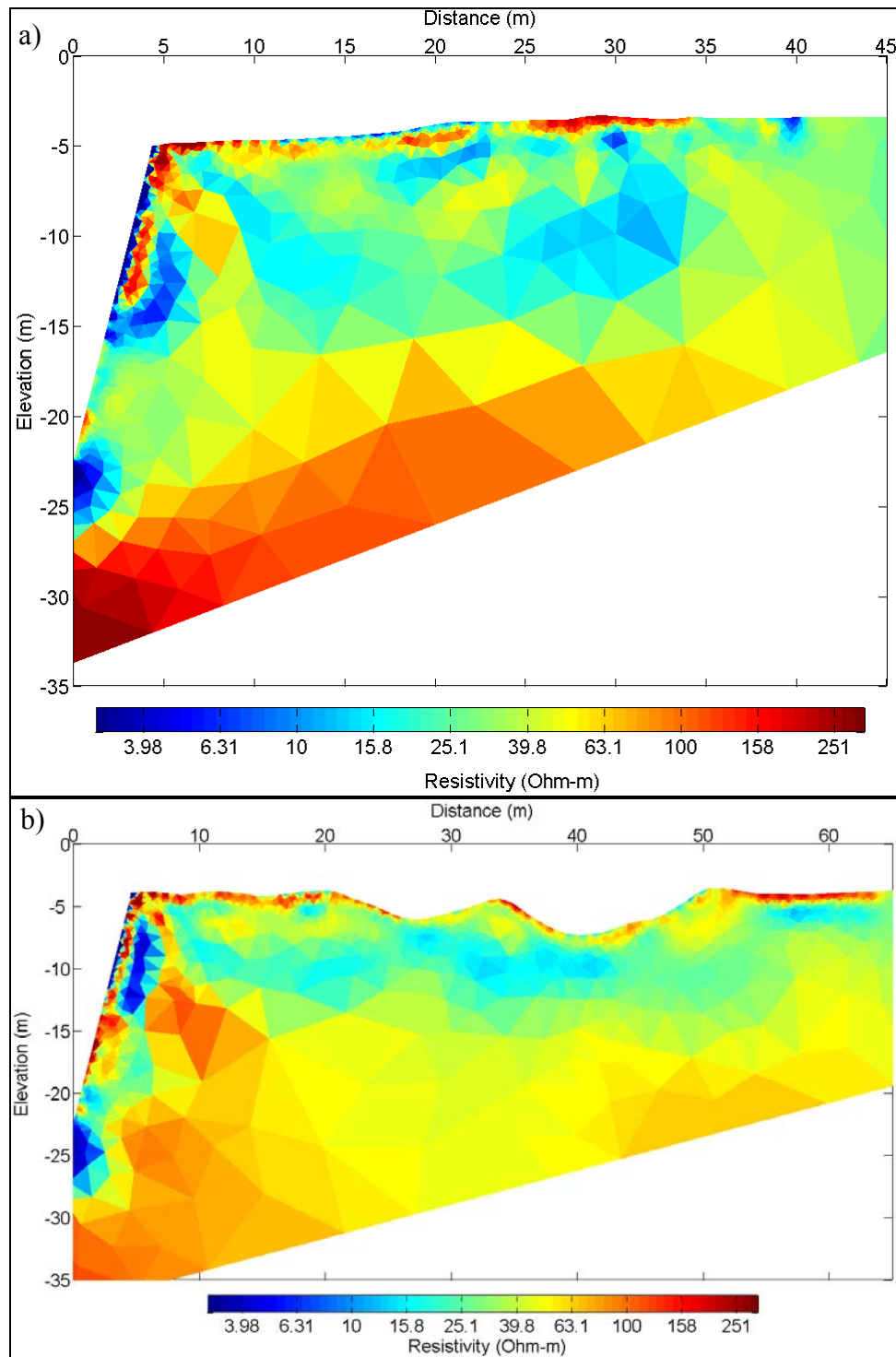


Figure 5.6. Cliffside 2-D resistivity inversion profiles of 2006 dataset. (a) CLF-1 and (b) CLF-5 showing conductive blue zones of possibly wet, clay-filled mass movement zones on the cliff face.

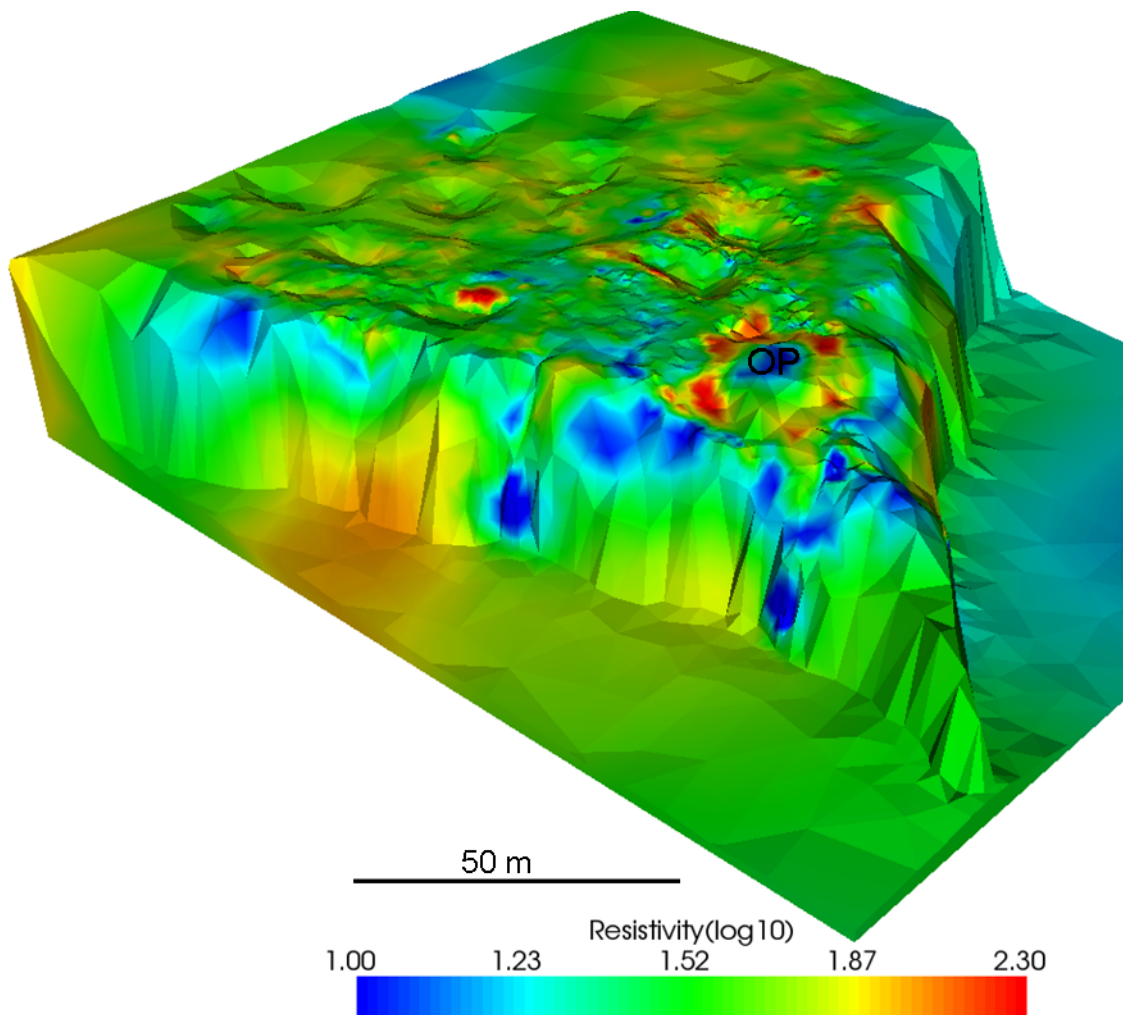


Figure 5.7. The 3-D resistivity tomogram produced from the 2008 OP dataset, viewed from the northeast. The rms error of the inversion result is $\sim 20\%$.

The main features shown in the 2008 OP resistivity tomogram can be identified as follows. First, there are small-scale irregular variations in resistivity scattered across the entire site. These near-surface resistivity variations could be caused either by variations in electrode-ground coupling, variations in soil moisture, or by the presence of cultural clutter, such as buried reinforced concrete. Most of the surficial anomalies are in yellow to red colors, which indicates that they are due to resistive near-surface structure. Poor electrode coupling would yield such a resistive signal, as would patches

of relatively dry and loose soil. Reinforced concrete, on the other hand, would likely appear as a conductive anomaly due to the presence of iron in the reinforcing bars. Therefore, the surficial resistive anomalies are best explained either by poor electrode-ground coupling or as zones of relatively low soil moisture.

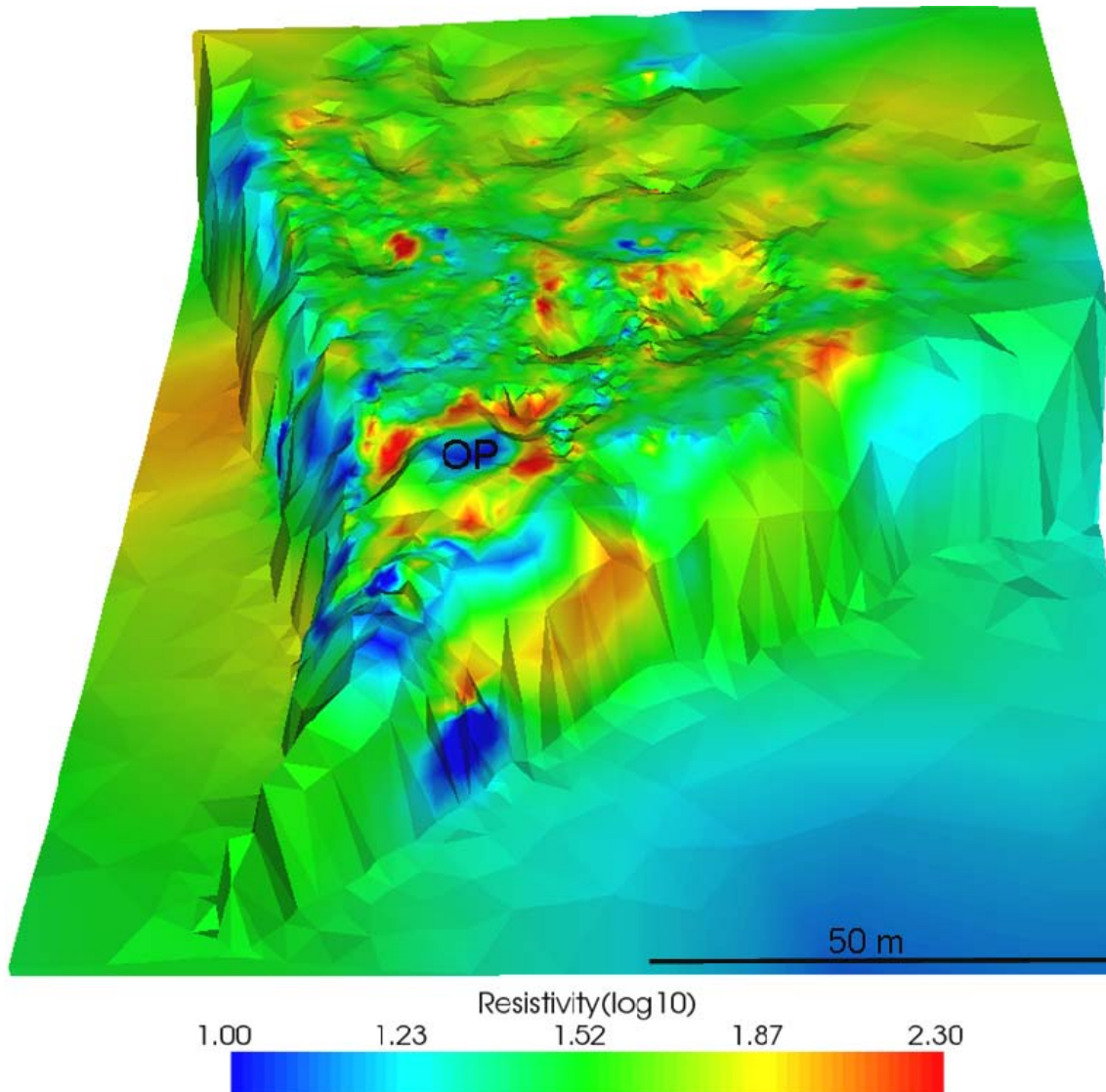


Figure 5.8. The 3-D resistivity tomogram produced from the 2008 OP dataset, viewed from the northwest.

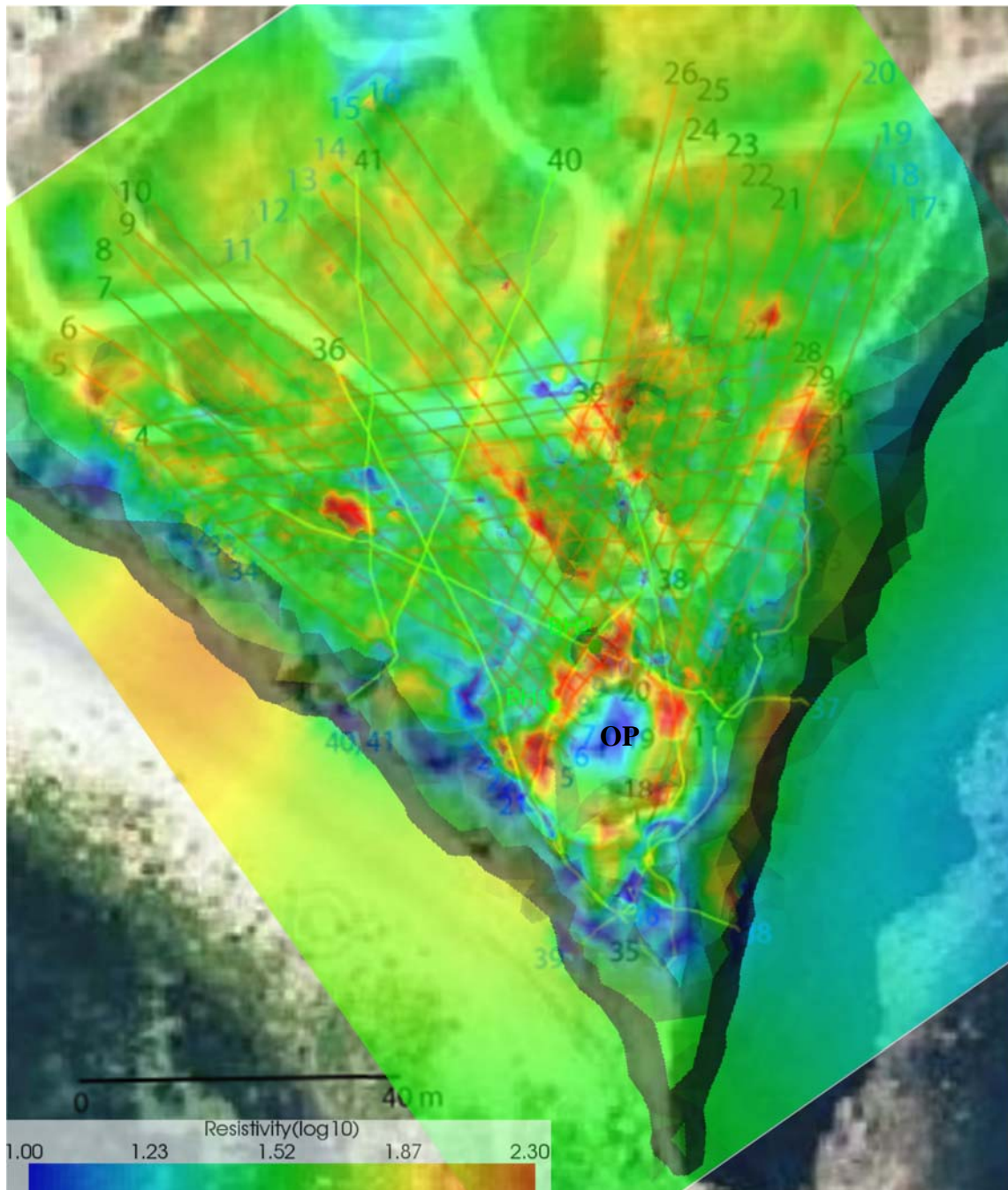


Figure 5.9. Top view of the 2008 OP 3-D resistivity tomogram with resistivity lines on the OP aerial photo.

The signature of the observation post itself is clearly seen in the 2008 OP resistivity tomogram. This building, situated close to the point, appears as the prominent circular anomaly consisting of the conductive (blue) inner core surrounded by the resistive (red) halo (Figure 5.9). The observation post has a complicated shape and was constructed by Wehrmacht engineers using ample reinforced concrete and other steel reinforcements. The surface geophysical expression of this structure takes the shape of the circular anomaly in the tomogram.

Another feature of the OP tomogram is the apparent east–west asymmetry of the resistivity structure offshore from the base of the cliffs (Figure 5.8 and 5.9). The rocky wave–cut terrace to the west of the point (appearing as a blue zone) seems to be more conductive than the gravelly shingle beach to the east of the point (a red zone). This may be an actual effect of subsurface geology, but it should also be mentioned that the west–side data were acquired predominantly at high tide when the sea was close to the base of the cliffs. The east side data were taken mainly at lower tide when the sea was further out. The sea is highly conductive, with resistivity $\rho = 0.3 \Omega\text{m}$. To navigate the electrode locations on the east side, it was required to lower the total station down to the beach at low tide because there is no topside vantage point for the total station. There was no need to lower the total station to the beach on the west side since there is a topside location from which the survey instrument could see all the electrodes on the cliffside. Thus, the east–west asymmetry shown in the tomogram is likely caused by the proximity of the sea to the electrode profiles at the time of data acquisition.

On both the east and the west cliff faces, there are some interesting resistivity anomalies in the OP tomogram. On the east cliff face, as shown in Figure 5.7 there is a distinct resistive zone (shown in red) located approximately in the middle of the cliff line and continuing down to the beach. This resistive zone indicates a zone of open, dry fractures and, according to the scheme discussed earlier, is assigned as a moderate stability hazard. While the red zone is certainly an area of concern, an even greater risk to the observation post is posed by the large conductive anomalies (shown in blue) that lie along the east cliff edge and base in Figure 5.7. This anomaly is interpreted as a zone

of wet, clay-filled fractures and is considered to be an area of very high mass movement potential.

On the west face, as shown in Figure 5.8, there is also a very large resistive anomaly immediately beneath the observation post. This anomaly is interpreted as a zone of a moderate stability hazard. The large conductive anomaly that lies near the west-facing cliff base in Figure 5.8 is at greater risk of mass movement hazard as it is a zone of wet, clay-filled fractures. We decided to explore this high-risk anomaly in greater detail. Using the ParaView visualization software, we draped the OP tomogram over the laser scan point cloud combined with textural information from digital photographs. A view of the west-facing cliff is shown in Figure 5.10. Notice that the blue, conductive anomaly is associated with large wave-cut caverns at the base of the cliffs near the point. This image indicates that the rocks inside and above the caverns are wet; either from seawater, groundwater, or both. The wave action is particularly strong at the position of the blue anomaly because incoming waves from the English Channel are refracted, or bent, around the headland and their energy is focused on the cliff base at some distance behind the actual point.

From a geological standpoint, it is not surprising that this region is identified as high-risk for mass movement. Consider the geological processes involved in the formation of a sea stack, as illustrated in Figure 5.11. Notice that the weak area identified in Figure 5.11a corresponds almost exactly to the location of the blue conductive anomaly at Pointe du Hoc. In Figure 5.11b, it is seen that, over time, the “weak area” gets widened and deepened by erosion to form a sea arch. In Figure 5.11c, it is seen that further erosion of the arch leads to the collapse of the roof and the formation of an isolated sea stack. This process has already occurred at Pointe du Hoc as evidenced by the current sea stack at the site. In Figure 5.11d, the formation of a series of sea stacks is indicated along with inland retreat of the headland. This process is occurring today at Pointe du Hoc. The blue conductive zone shown in Figure 5.10 (note also there is a second blue zone on the opposite, east-facing cliff close to the point) marks a region that

eventually will widen and deepen and form a sea arch. When the roof of this sea arch collapses, the observation post may be badly damaged or destroyed.

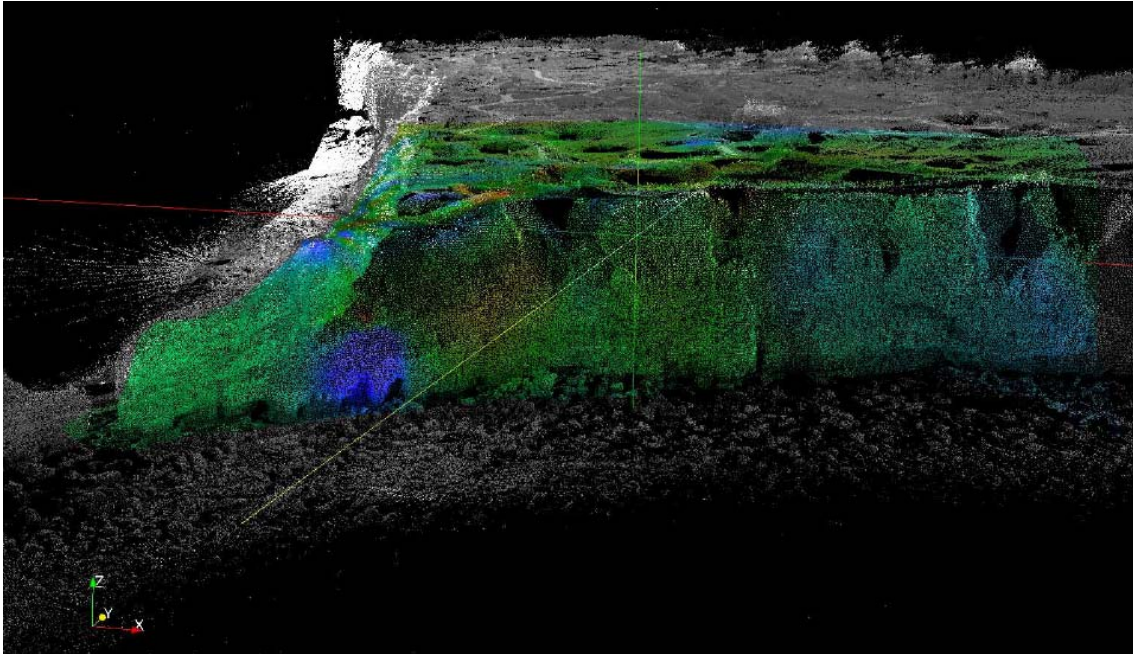


Figure 5.10. The 2008 OP resistivity tomogram combined with terrestrial laser scanning data.

While the formation of a sea stack is a geological process, it does not necessarily occur over long geological time scales. Historical photographs, for example, reveal that the isolated sea stack now at Pointe du Hoc was connected to the mainland during the June 1944 invasion. Sea arches in general are ephemeral structures that typically survive only a few decades before collapsing, often during great storms. The keyhole that is presently forming in the Pointe du Hoc stack (Figure 2.9a) is a very recent erosive feature that was not evident a few years ago; it is expected to rapidly grow and contribute to the ultimate destruction of the point stack.

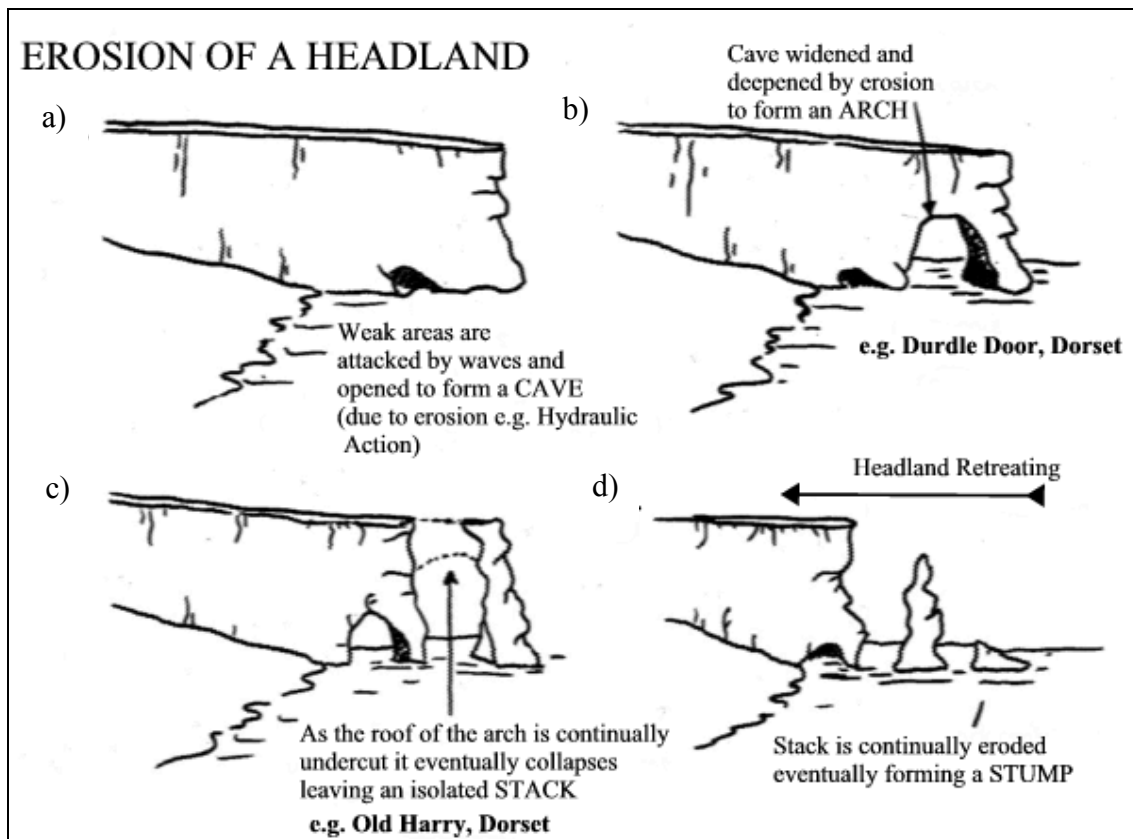


Figure 5.11. Formation of a sea arch and stack. Image downloaded from <http://www.geobytesgcse.blogspot.com>.

Due to the great complexities inherent in coastal erosion processes, and the many variables involved, it is not possible to make a definitive prediction of when the putative sea arch at Pointe du Hoc will form and then collapse. Coastal recession is an episodic geological process that is greatly accentuated by events such as large storms which are inherently unpredictable more than a few days in advance. For evaluation of the erosion risk, coastal engineers largely agree that some elements of stochastic modeling and estimation must be included (Hall et al., 2002). Further discussion on quantitative aspects of coastal geomorphology is beyond the scope of this dissertation.

There is much additional information contained in the 2008 OP tomogram. The bird's-eye views shown in Figures 5.7 and 5.8, and the top view shown in Figure 5.9 reveal only the surface expression of the resistivity distribution. In order to examine the

subsurface geoelectric structure it is convenient to take 2-D section constant-depth slices through the tomogram, which is easily accomplished using the ParaView software. A series of horizontal slices through the OP tomogram at constant topographic elevation z (vertical coordinate) value equals 0, -5, -10, -15, -20, and -25 m is shown in Figure 5.12. The resistivity distribution within each slice reveals important geological information at the corresponding depth. Note that the topographic elevation z of the overall Pointe du Hoc area is based on the laser scanning topographic points (Figure 4.12) which varies from -30 m on the beach to +2 m on the south end, while the elevation of the OP building area is from \sim -5 m at the cliff edge close to the point to \sim -2 m at the top of the bunker. Other 2-D vertical slices of the 2008 OP tomogram are shown as a series at every 15 m intervals in Figure 5.13. Each vertical slice shows resistivity distribution that reveals important subsurface information.

Examinations of the horizontal slice for elevation -5 m (Figure 5.12b), for example, reveals that the circular resistivity anomaly associated with the OP building extends from the surface (Figure 5.9 and 5.12a) at least this far below the surface. There is a weaker but significant indication of the OP building in the -10 m horizontal slice (Figure 5.12c) while it has essentially disappeared by the -15 m horizontal slice (Figure 5.12d). The lack of a strong OP building signature at elevation lower than -5 m suggest that its foundations are not deeply rooted to the underlying calcarenite/limestone bedrock.

The horizontal slices through the OP tomogram also reveal the presence of a large resistive (colored red) zone on the west side of the site (the right-hand side of the horizontal slices). The large resistive zone persists to all depths and is accompanied by a second large resistive area at elevation below -20 m depth (Figure 5.12f). These red zones are interpreted as areas consisting mainly of open, dry fractures that indicate a moderate mass movement hazard.

In general, the subsurface becomes more resistive (red) with increasing depth. This reflects the fact that the consolidated Mesozoic siliciclastic/carbonate rocks are inherently more resistive than the silty-clay Quaternary cover. Thus, there is a general

tendency for the color scheme to progress from blue to green to red with increasing depth (see Figure 5.12). Notice that, at the -10 m and -15 m horizontal slices in Figure 5.12c and 5.12d, the east side of the site appears in green colors, even though it is composed of Mesozoic rocks. This probably means that the east side is slightly wetter or has slightly greater clay content than the west side, but there is not enough conductive material on the east side to raise significantly the mass movement hazard potential, which would be indicated in our color-coding scheme by the presence of a blue zone.

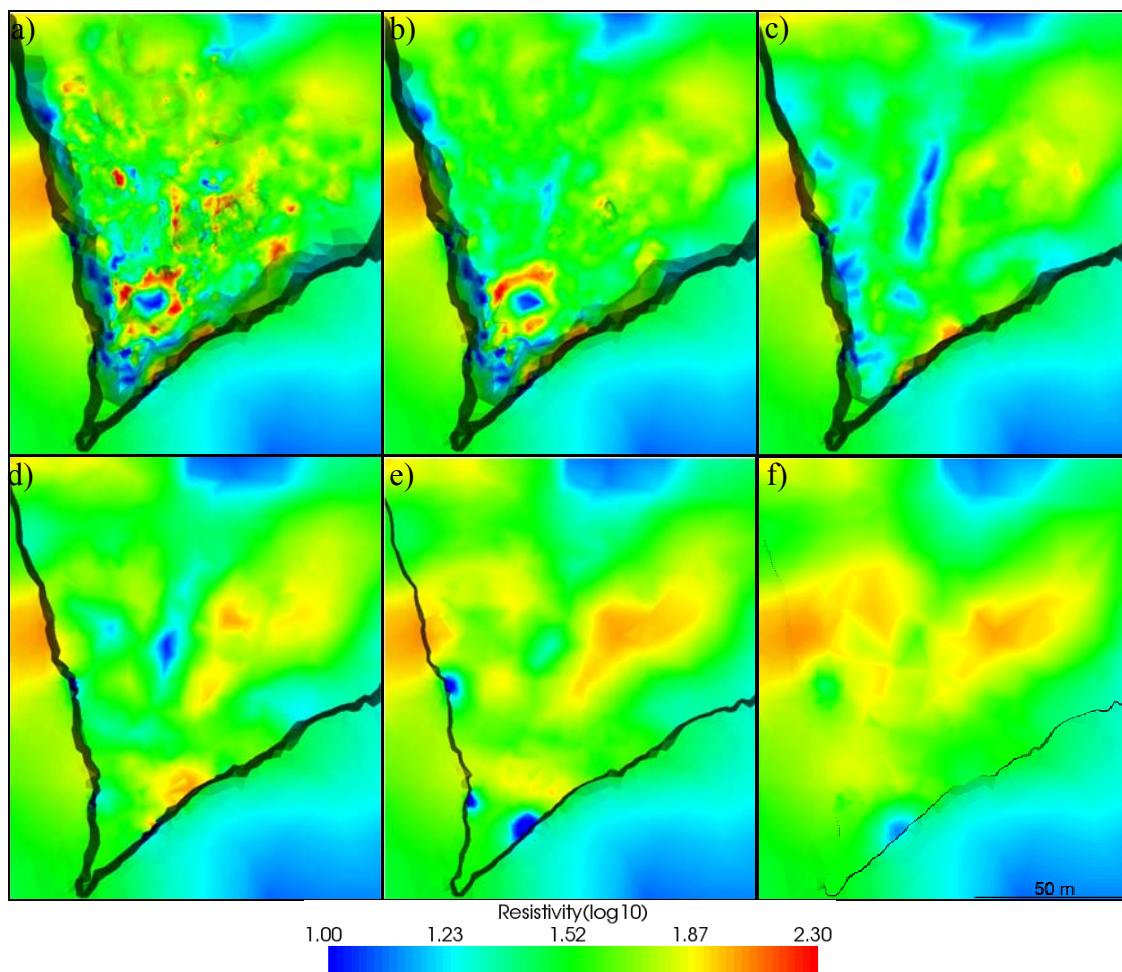


Figure 5.12. Horizontal slices through the 2008 OP 3-D resistivity tomogram. (a) 0 m elevation, (b) -5 m elevation, (c) -10 m elevation, (d) -15 m elevation, (e) -20 m elevation, and (f) -25 m elevation.

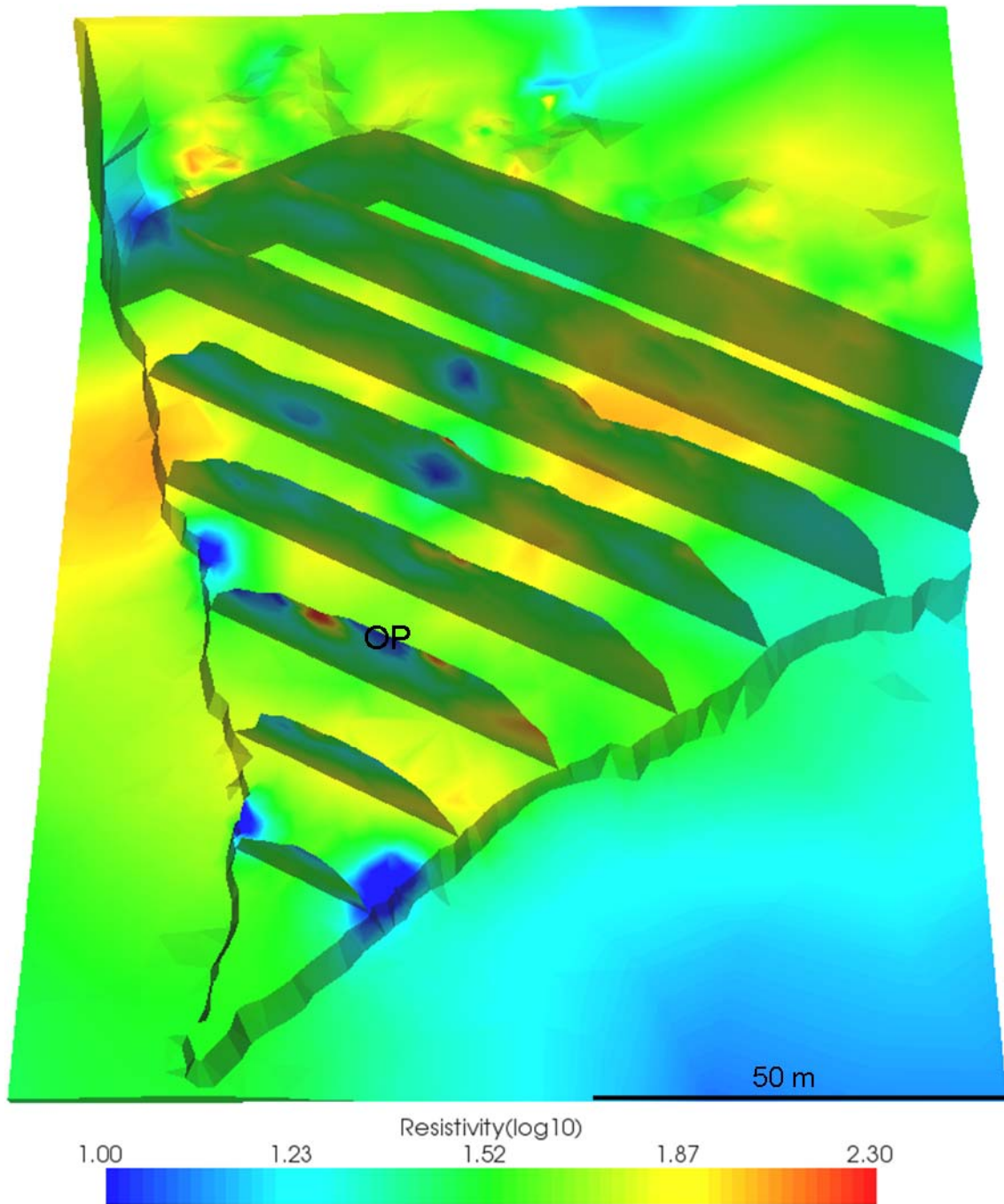


Figure 5.13. Vertical slices through the 2008 OP tomogram. The vertical slices are 15 m interval standing over the horizontal slice of -20 m elevation.

Looking at the various 2008 OP horizontal and vertical slices, there do not appear to be many extensive blue regions of conductive materials, interpreted as wet clay-filled fractures, in the vicinity of the observation post. Such blue zones would indicate a high mass movement hazard. There are several small blue zones at the 10 m depth slice (Figure 5.12c). One is a linear blue zone running roughly north-south in the middle of the site landward of the OP building. This linear blue zone corresponds to the circular blue anomaly appearing on the two vertical slices located south of the OP building (Figure 5.13). The linearity and circularity of this feature however is more suggestive of a subsurface cultural feature such as a steel-reinforced tunnel. Further investigation of this intriguing anomaly should be made but it does not seem to be related to cliff stability. Of more concern are the blue zones on the east-facing cliff edge seen in the -10 m horizontal slice (Figure 5.12c). These are indicative of wet clays in the Quaternary soil cover and they indicate a high soil wedge-failure hazard. On the west-facing cliff edge, the soil appears to be a dry resistive (red) zone, with a corresponding lower wedge-failure potential. Note the conductive (blue) anomalies at the base of east-facing cliff on -20 horizontal slice and on the base of the west-facing cliff extending from -20 m to -25 m horizontal slice. These anomalies are likely associated with the cliff base cavern as explained above.

To summarize the OP tomographic results, the highest mass movement hazard appears to be associated with the marine caverns at the base of the cliff that are positioned at the point of strongest wave attack. These caverns likely occupy the future site of development of a sea arch which will definitely threaten the OP building. There is also a high probability of a soil wedge failure on the east-facing cliff edge close to the OP building. The rest of the topside area shows mainly red resistive features that are indicative of open, dry fractures. The possibility cannot be ruled out of a sudden catastrophic failure along any one of these fractures, due to inherent limitations of resistivity tomography as a monitor of bulk rock strength, but there does not seem to be any localized area of immediate concern. Overall, the topside displays a moderate mass movement potential.

INTERPRETATION OF 2008 RCP DATA

A bird's-eye perspective of the computed 2008 RCP 3-D tomogram is shown in Figure 5.14. Figure 5.15 illustrates the top view of the RCP 3-D tomogram combined with the resistivity line locations, both superimposed on the site aerial photo. The range of resistivities extends from $\log_{10} \rho = 0.70$ ($\rho = 5 \text{ } \Omega\text{m}$, shown in blue) to $\log_{10} \rho = 2.30$ ($\rho = 200 \text{ } \Omega\text{m}$, shown in red). The RCP resistivity tomogram shows small-scale irregular variations in resistivity scattered across the topside surface. Most of the surficial anomalies are in red colors, which indicate that they are best explained either by poor electrode-ground coupling or as zones of relatively low soil moisture. The signature of the RCP building itself is clearly seen in the tomogram as the large red quasi-circular anomaly near the center of the tomogram. The offshore structure in the tomogram appears as a blue region, indicative of the conducting seawater.

As shown in the RCP tomogram (Figure 5.14), there is a very large conductive anomaly (shown in blue) that cuts across the north cliff face of the RCP building. This anomaly is interpreted as a zone of wet, clay-filled fractures. There is smaller blue zone (lighter color) on the cliff face to the south side of the RCP building. In general, the cliff face at the RCP site is quite conductive and represents an area of moderate to high mass movement potential. Figure 2.11a shows that there already have been a couple of recent collapses along the top of the cliff between the OP and RCP buildings. The region around the RCP building might well be the next site of a similar cliff collapse. The next collapse could have potentially damaging consequences for the RCP building.

A series of vertical slices through the RCP tomogram with 15 m interval is shown Figure 5.16. Figure 5.17 shows a series of horizontal slices through the RCP tomogram at constant elevation values of z equals 0, -5, -10, -15, -20, and -25 m. Note that the elevation of the RCP area is based on the laser scanning data, which varies from ~ 1.6 m on the top side to ~ -30 m on the beach. The elevation of the cliff edge closest to the RCP building is ~ -3 m. Both horizontal and vertical slice views of the RCP tomogram reveal that the interior resistivity structure around the RCP building is very resistive at depth, as shown by the large red zone. Any fractures would be open and

dry. Overall, the geoelectrical structure corresponds quite closely to the expected resistivity distribution of a two-layer stratigraphy consisting of Quaternary silty-clays overlaying consolidated Mesozoic rocks. There does not appear to be a significant blue zone of wet, clay-filled fractures beneath the interior of the RCP site. The more conductive zones are found near the cliff edge where both the horizontal and vertical slices show green colors even at greater depth.

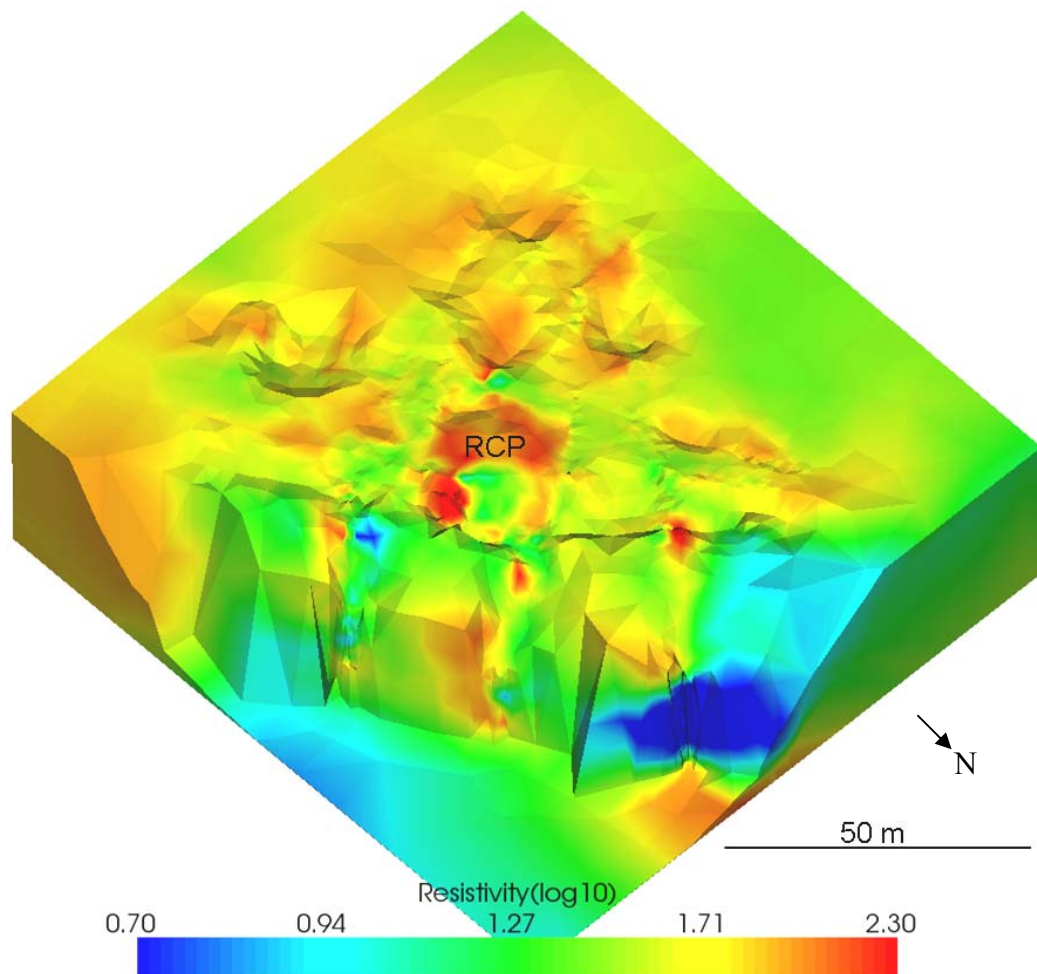


Figure 5.14. The 3-D resistivity tomogram produced from the 2008 RCP dataset. The rms error of the inversion is ~14%.

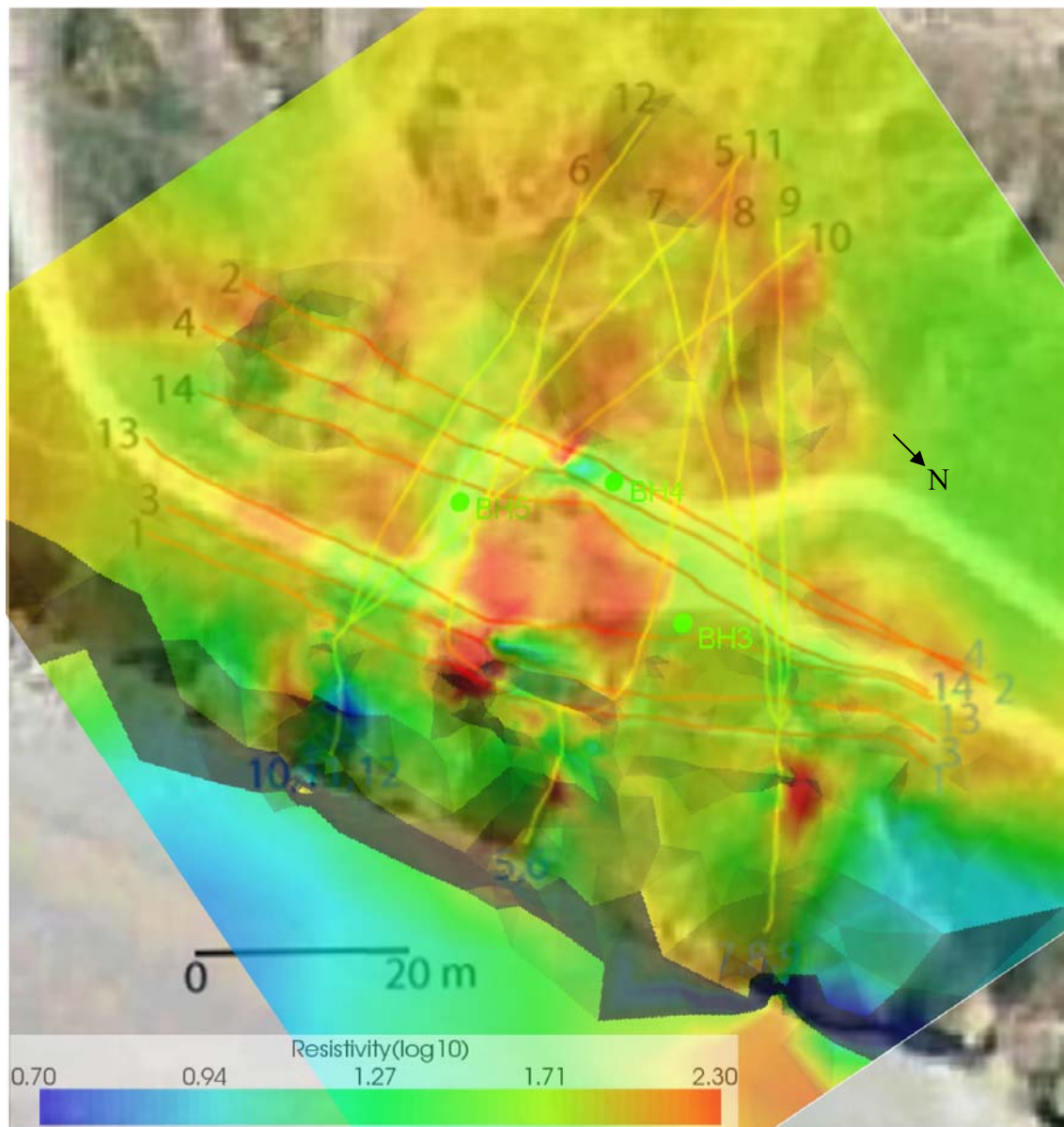


Figure 5.15. Top view of the 2008 RCP 3-D tomogram with resistivity lines on the RCP aerial photo.

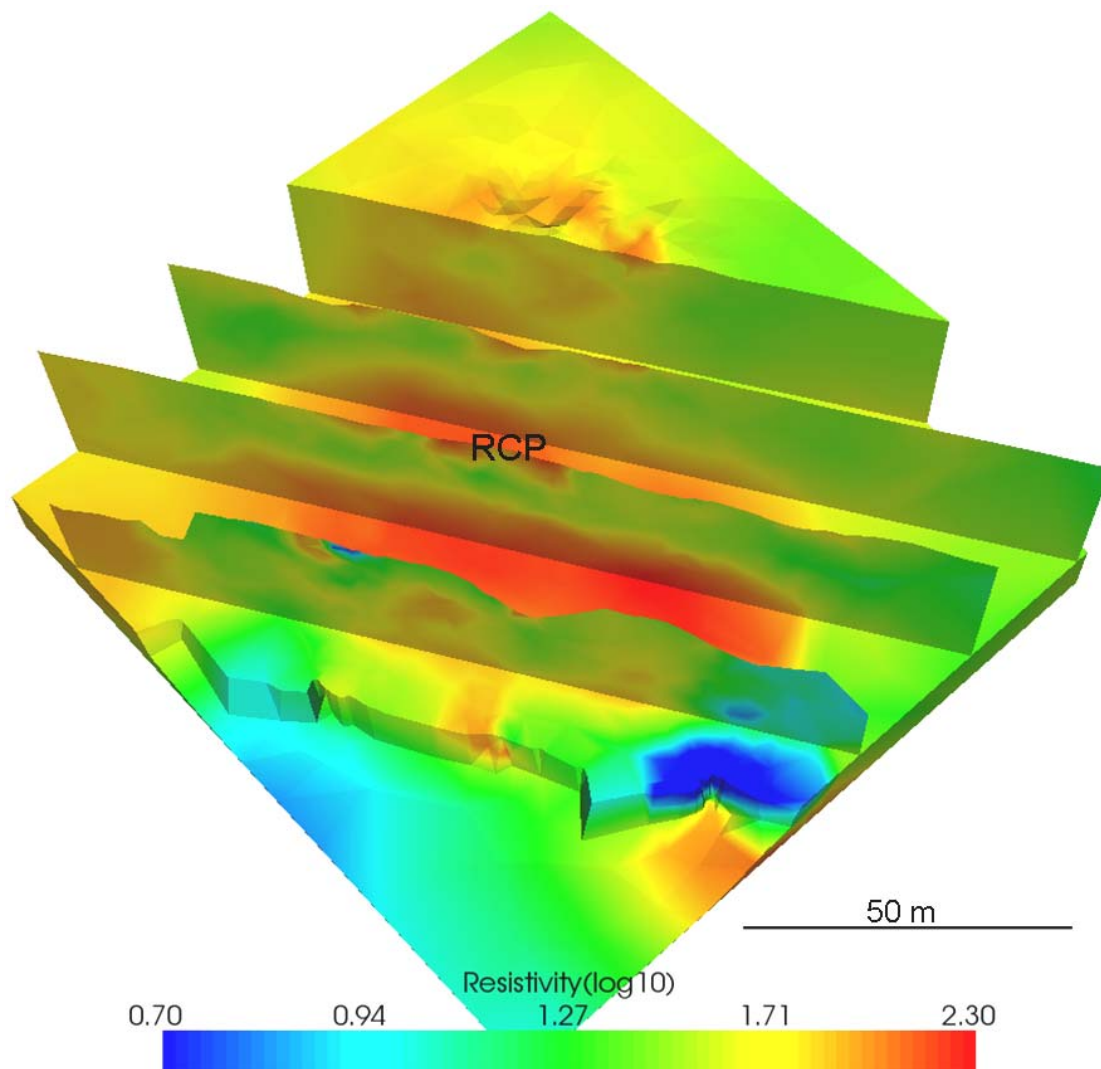


Figure 5.16. Vertical slices through the 2008 RCP tomogram. The vertical slices are 15 m interval standing over the depth slice of -20 m elevation.

To summarize the RCP resistivity tomography results, the mass movement potential at the RCP site is low to moderate. The greatest risk appears to be associated with failures at the cliff face like those shown in Figure 2.11a.

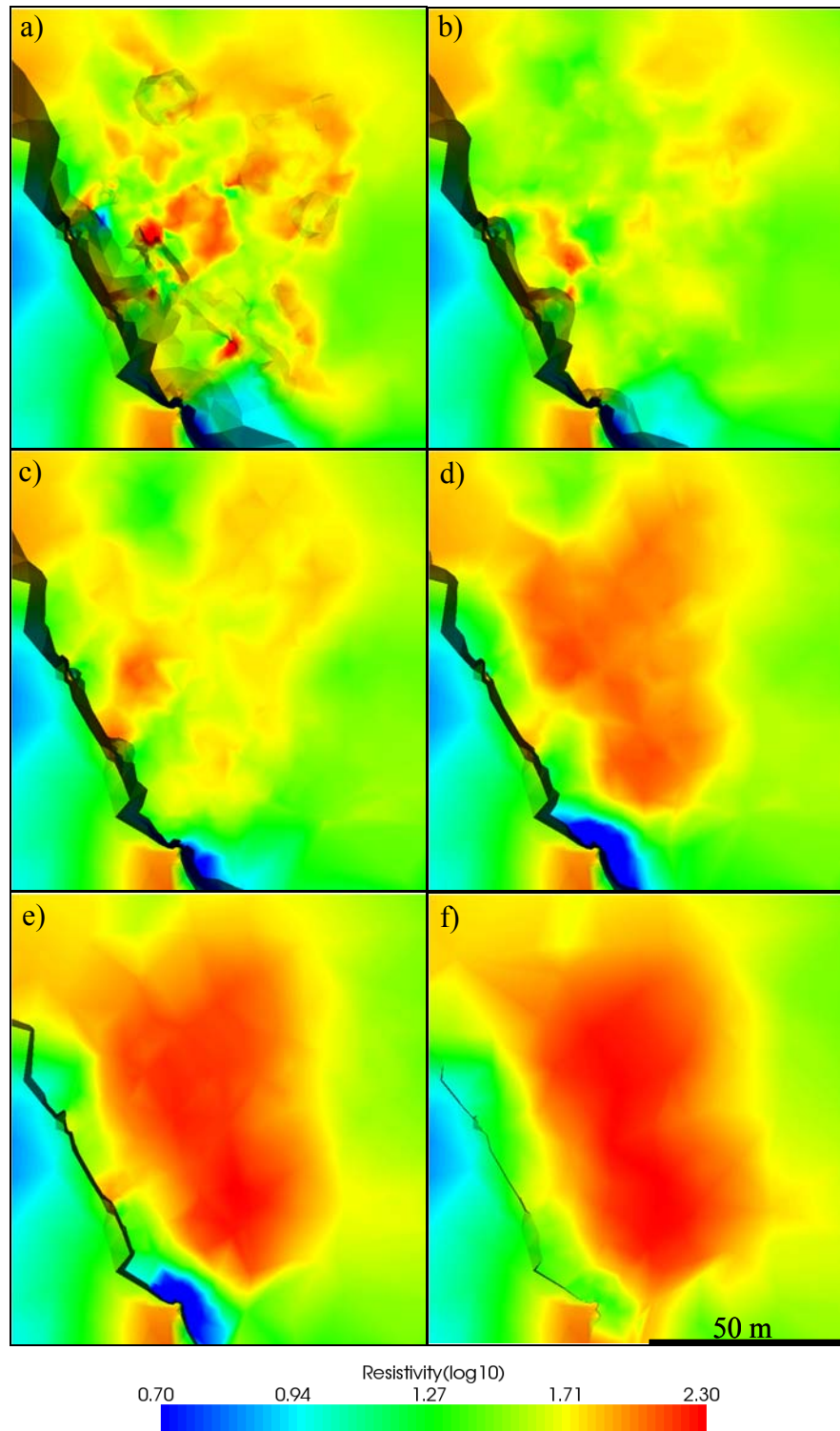


Figure 5.17. Horizontal slices through the 2008 RCP 3-D resistivity tomogram. (a) 0 m elevation, (b) -5 m elevation, (c) -10 m elevation, (d) -15 m elevation, (e) -20 m elevation, and (f) -25 m elevation.

CHAPTER VI

DISCUSSION AND CONCLUSIONS

DISCUSSION

The cliff stability assessment at Pointe du Hoc, for the purposes of cultural resources preservation, is a challenging and complex Earth sciences problem that requires an interdisciplinary approach. A resistivity tomographic solution has been developed, based on rigorous and state-of-the-art geophysical forward modeling and inversion. Within the inherent limitations of the methodology, the subsurface resistivity distribution $\rho(\mathbf{r})$ to the target depths of ~20–25 m beneath the site has been determined, especially beneath the two major at-risk buildings (Observation Post and Rudder's Command Post) which lie close to the cliff's edge. The resistivity tomography is informed by complementary Texas A&M efforts in terrestrial laser scanning and geotechnical site characterization.

Geophysics plays a prominent role in the evaluation of cliff stability since electrical resistivity is related to important bulk physical properties such as porosity, water content, clay content, lithology, and fracture density. These quantities are important factors that control the bulk strength of rock formations and hence the mass movement potential. The complex stratigraphy at Pointe du Hoc, including the clay-silt soils, calcarenites, hard sandstones, bioclastic limestones and marls, in addition to the extreme topography and dense cultural clutter, renders electrical geophysics and the interpretation of resistivity tomograms very challenging. The relationship between carbonate porosity and resistivity is particularly difficult to constrain since it depends strongly on the pore-scale and vug-scale geometry, both of which are largely unknown in the absence of detailed petrophysical analyses. Nevertheless, electrical geophysics offers a unique opportunity to obtain non-invasive and inexpensive subsurface data that are relevant to the overall study goals.

At Pointe du Hoc, the field acquisition of data is divided into two phases; the 2006 reconnaissance and the 2008 high resolution phases. At the reconnaissance data acquisition stage, to enable an overall site survey, 18 resistivity lines were obtained within the one month field work time constraints. An AGI SUPER STING™ R8 IP multi-electrode resistivity system was used to acquire data consisting of 56-electrode resistivity lines with line extensions of 14 electrodes or more when using the roll-along technique. The data were acquired in hybrid Schlumberger/dipole-dipole electrode configurations, an optimal combination providing both deep penetration and good lateral resolution. Ten resistivity profiles with 3-m electrode spacing were acquired on the topside of the site; two profiles with 1-m electrode spacing were acquired at the Observation Post building area; and six profiles with 1-m electrode spacing were draped over the cliff edge with significant portions extending onto the near-vertical cliff face. Electrode positioning using a total-station technique at this stage was crude without obtaining positions of the electrodes directly straight on the cliff face. It was assumed that the slope of the cliff face was constant 4:1 and that the electrodes were planted along the same azimuth as the topside portion of the profile and at 1.0 m uniform tape-measure distance from each other. This assumption however led to systematic error for data analysis since the electrode positions were somewhat mislocated. Since the spacing between 2-D resistivity lines of the 2006 dataset is too coarse for the size of the survey area, the 3-D dataset resulted in a 3-D resistivity tomogram that provides poor horizontal resolution information of the detailed subsurface resistivity of the site especially near the critical at-risk buildings. Nevertheless the 2006 dataset was very useful for a rapid overall site assessment.

The 2008 high-resolution phase utilized the resistivity tomographic reconstruction based on fairly standard geophysical methodology. A total station was used with an improved technique to establish a temporary control network which enabled accurate navigation of the electrode positions and elevations. The AGI SUPER STING™ R8 IP multi-electrode resistivity system was used again to acquire the data in Schlumberger/dipole-dipole electrode configurations. The survey was designed with 2-

m electrode spacing on lines each consisting of 42 electrodes. Within the time constraints of the field work, 24 days, two designed survey grids were acquired including cliffside profiles for improved resolution of the deeper geological strata close to cliff's edge. The survey grid at the Observation Post area included 37 resistivity lines, while the survey at Rudder's Command Post included 14 lines. The cliffside data, which provide unique constraints rarely available to geophysicists, were acquired using a safe, releasable rappel system which was overseen by a skilled professional rock climber. This has pushed the frontiers of geophysical data acquisition and has resulted in one of the best resistivity data sets of its kind in the world.

Mass Movements

Mass movement is a geological process that transports Earth materials down slopes under the force of gravity (Chernicoff and Whitney, 2002). As a natural geohazard, mass movement threatens human life and property, which at Pointe du Hoc includes tourists and important cultural resources. As a result of the danger faced by a possible cliff collapse, the Observation Post has been closed to visitors for several years.

Based on careful geological study of the landscape including slope compositions, layering, water content, drainage, slope angles, borehole data, and evidence for past mass-movement events such as landslide scars and slide debris, engineering geologists can build up a mass-movement hazard map at a give site. In practice, geophysics is rarely used as an integral part of the overall hazard assessment. One reason for this is that most engineering geologists are not specifically trained in geophysics, which is a demanding technology to master. Another reason is that high-resolution 3-D geophysical techniques are still under active research and development. A third reason is that the relationship at a given site between bulk electrical resistivity and rock strength requires detailed observations, involves complex physics, and generally is poorly understood in a theoretical sense.

Geotechnical engineers see geophysics as a way to pre-screen a wide volume of rock in order to detect hot spots or areas of concern that might impact engineering

structures that have been developed. Geophysics is used to identify areas that need to be examined in closer details, as the detailed site assessment is made by geotechnical engineers. Geophysics forms part of the useful information that have to be considered for designing engineering structures to improve the site stability assessment by geotechnical engineers.

Geophysical subsurface imaging has made great strides in recent years toward overcoming the barriers to its routine use by geotechnical engineers. Resistivity tomography is a particularly good example. Improvements have been made in instrumentation, data analysis, and interpretation. Multi-electrode resistivity systems such as the SUPER STING™ are becoming widely used in engineering projects and environmental site characterization due to their ease of use, reliable performance, large and expandable electrode arrays, and flexible computer-controlled data acquisition protocols. Modeling and regularized inversion of resistivity data based on 3-D finite element schemes that can handle extreme topography and large computational meshes are now providing reliable high-resolution subsurface images that have been successfully ground-truthed in many situations. With the new equipment and data analysis tools, plus simultaneous advances in laboratory measurements of electrical properties of rocks, geophysicists are continuously improving their resistivity tomogram interpretation skills. Visualization software such as ParaView has enabled geophysicists to display subsurface information from a variety of perspectives and to combine geophysical data with more familiar data types such as laser scanning and digital photography.

Limitations of Resistivity Tomography

The largest knowledge gap in the use of geophysics for natural geohazard interpretation of resistivity tomograms is the conversion of resistivity to bulk rock strength. However, there are a number of other basic limitations of resistivity tomography that should be mentioned. The most fundamental limitation, which applies to all geophysical methods, is that any dataset that we can practically acquire is

inadequate to perform perfectly the task of subsurface physical property reconstruction. The reasons are multifold: (a) Earth is infinitely complex but we have only a finite number of measurements to describe it; (b) geophysical data are never recorded with ideal fidelity; (c) geophysical data are sparsely sampled; (d) a given data set can be explained by more than one subsurface distribution of physical properties; (e) forward modeling and inversion algorithms accumulate numerical errors; (f) resistivity imaging in geomaterials is not perfectly captured by the governing equations.

Owing to the limitations outlined above, it is clear that resistivity tomography is not an ideal technology that provides iron-clad solutions. Careful data acquisition, attention to possible causes of error, and good experimental design can ensure that the best possible dataset is achieved within the available time and budget constraints. Skill, expertise, intuition, and experience of the geophysicist, in addition to the judicious incorporation of auxiliary data from other sources, are required in order to make the best assessment of a given dataset. The geophysicist must carefully select the trade-off between data misfit and regularization, for example, since this decision can greatly affect important details of the reconstructed image. The geophysicist must also decide how much weight to assign to different types of auxiliary data.

The Pointe du Hoc resistivity tomography is nevertheless an exemplary geophysical dataset. In 2008 a high-resolution grid around the Observation Post, the most critical at-risk building, was acquired which included cliffside data, accurate electrode navigation, and terrain information from laser scanning. The dataset at Rudder's Command Post, the second at-risk building, has the same high data quality but has less spatial resolution since fewer time resources were available to complete the geophysical survey. In this dissertation an interpretation of the resistivity tomograms has been provided and an opinion on the mass movement potential of the cliff has been offered.

There are several possibilities that could be explored to conduct additional geophysical study of the stability of the Pointe du Hoc cliffs. The resistivity datasets are quite comprehensive so that acquisition of additional resistivity profiles is not an

immediate priority. Instead, the existing resistivity data could be complemented with other surface geophysical data such as high-resolution seismic reflection and refraction surveys. Seismic reflection data provide images of subsurface contrasts in acoustic impedance, which is the product of density and seismic velocity. The latter is a mechanical property that is related to the bulk and shear moduli; which are both good indicators of rock strength. The imaging capability of high-resolution seismic reflection methods can also provide a better handle on the stratigraphic layering, depth of soil cover, etc. Seismic refraction, with its subsurface signal transmission characteristics, can provide important information on fracture density and other lateral changes in subsurface structure. Seismic and resistivity data may be inverted jointly to obtain a subsurface physical property map that is mutually consistent with both data types. It would also be beneficial to perform geophysical logging of the geotechnical borings. This will provide in situ estimations of physical properties such as electrical resistivity, porosity, density, water content, and fracture density. It should be recognized that geophysical logging is an invasive technology that provides data only at discrete locations.

CONCLUSIONS

3-D resistivity tomography data at Pointe du Hoc have been successfully acquired in the presence of extreme topography and dense cultural clutter. The cliff stability in the areas around the two major at-risk buildings has been analyzed. A hazard assessment scheme has been designed in which regions of high resistivity are interpreted as zones of open, dry fractures with a moderate mass movement potential. Regions of low resistivity are zones of wet, clay-filled fractures with a high mass movement potential.

The results of the Observation Post tomography indicate that the highest mass movement hazard appears to be associated with the marine caverns at the base of the cliff that are positioned at the point of strongest wave attack. These caverns likely occupy the future site of development of a sea arch which will definitely threaten the Observation Post building. There is also a high probability of a soil wedge failure on the

east-facing cliff edge close to the OP building. Such a failure could damage or destroy the building. The rest of the topside area shows mainly resistive features that are indicative of open, dry fractures. The possibility of a sudden catastrophic failure along any one of these fractures, due to inherent limitations of resistivity tomography as a monitor of bulk rock strength, cannot be ruled out. The mass movement potential at the Rudder's Command Post area is low to moderate. The greatest risk is associated with soil wedge failures at the top of the cliffs.

The resistivity geophysical data add great value to the natural geohazard assessment at Pointe du Hoc and constitute an integral component of an interdisciplinary approach to the problem of cultural resource preservation at the site. Geophysics is a non-invasive and relatively inexpensive technology that provides unique constraints which are unobtainable using traditional engineering geology methods for site characterization. However, the technology is difficult to master and the inherent limitations must be carefully understood to ensure a reliable geotechnical interpretation.

REFERENCES

- Anthony, E. J., 2002, Long-term marine bedload segregation, and sandy versus gravelly Holocene shorelines in the eastern English Channel: *Marine Geology*, **187**, 221–234.
- Antoine, P., J. Catt, J. P. Lautridou, and J. Sommé, 2003, The loess and coversands of northern France and southern England: *Journal of Quaternary Science*, **18**, 309–318.
- Archie, G. E., 1942, The electrical resistivity log as an aid in determining some reservoir characteristics: *Transactions of the American Institute of Mining and Metallurgical Engineers*, **146**, 54–67.
- Asquith, G. B., 1995, Determining carbonate pore types from petrophysical logs, *in* P.H. Pause and M. P. Candelaria, eds., *Carbonate Facies and Sequence Stratigraphy: Practical Applications of Carbonate Models*, Midland, TX Permian Basin Section–SEPM: Permian Basin Graduate Center Publication, 69–80.
- Bates, M. R., D. H. Keen, and J. P. Lautridou, 2003, Pleistocene marine and periglacial deposits of the English Channel: *Journal of Quaternary Science*, **18**, 319–337.
- Bichler, A., P. Bobrowsky, M. Best, M. Douma, J. Hunter, T. Calvert, and R. Burns, 2004, Three-dimensional mapping of a landslide using a multi-geophysical approach: the Quesnel Forks landslide: *Landslides*, **1**, 29–40.
- Bogoslovsky, V., and A. Ogilvy, 1977, Geophysical methods for the investigation of Landslides: *Geophysics*, **42**, 562–571.
- Briaud, J. L., R. Abdelmalak, and B. Smith, 2007, Pointe du Hoc Stabilization Study: Geotechnical Report: Geotechnical Testing, Failure Analysis, Remedial Measures: Texas A&M University, College Station.
- Briaud, J. L., H. R. Nouri, and C. Darby, 2008, Pointe du Hoc Stabilization Study: Geotechnical Report: Texas A&M University, College Station.
- Brossard, J., and A. Duperret, 2004, Coastal chalk cliff erosion: experimental investigation on the role of marine factors, *in* R.N. Mortimore and A. Duperret, eds., *Coastal Chalk Cliff Instability*, Geological Society Engineering Geology Special Publication, v.20: Geological Society of London, 109–120.
- Bruno, F., and F. Marillier, 2000, Test of high-resolution seismic reflection and other geophysical techniques on the Boup landslide in the Swiss Alps: *Surveys in Geophysics*, **21**, 333–348.

- Chernicoff, S. and D. Whitney, 2002, *Geology*: Houghton Mifflin.
- Constable, S. C., R. L. Parker, and C. G. Constable, 1987, Occam's inversion: a practical algorithm for generating smooth models from electromagnetic sounding data: *Geophysics*, **52**, 289–300.
- Dahlin, T., 1996, 2D resistivity surveying for environmental and engineering applications: *First Break*, **14**, 275–283.
- Daniels, F., and R. A. Alberty, 1966, *Physical Chemistry*: Wiley.
- Dornbusch, U., D. A. Robinson, C. A. Moses, and R. B. G. Williams, 2008, Temporal and spatial variations of chalk cliff retreat in East Sussex, 1873 to 2001: *Marine Geology*, **249**, 271–282.
- Drahor, M. G., G. Gokturkler, M. A. Berge, and T. O. Kurtulmus, 2006, Application of electrical resistivity tomography technique for investigation of landslides: a case from Turkey: *Environmental Geology*, **50**, 147–155.
- Dugué, O., 2003, The Pliocene to early Pleistocene marine to fluvial succession of the Sueil de Contentin basins (Armorican massif, Normandy, France): *Journal of Quaternary Science*, **18**, 215–226.
- Duperret, A., A. Genter, R. N. Mortimore, B. Delacourt, and D. M. Pomerai, 2002, Coastal rock cliff erosion by collapse at Puy, France: the role of impervious marl seams within chalk of NW Europe: *Journal of Coastal Research*, **18**, 52–61.
- Duperret, A., A. Genter, A. Martinez, and R. N. Mortimore, 2004, Coastal chalk cliff instability in NW France: role of lithology, fracture pattern and rainfall, *in* R.N. Mortimore and A. Duperret, eds., *Coastal Chalk Cliff Instability*, Geological Society Engineering Geology Special Publication, v.20: Geological Society of London, 33–56.
- Duperret, A., S. Taibi, R. N. Mortimore, and M. Diagneault, 2005, Effect of groundwater and sea weathering cycles on the strength of chalk rock from unstable coastal cliffs of NW France: *Engineering Geology*, **78**, 321–343.
- Emery, K. O., and G. G. Kuhn, 1982, Sea cliffs: their processes, profiles, and classification: *Geological Society of American Bulletin*, **93**, 644–654.
- Focke, J. W., and D. Munn, 1987, Cementation exponents in Middle Eastern carbonate reservoirs: *Society of Petroleum Engineers Formation Evaluation*, **2**, 155–167.

- Gallipoli, M., V. Lapenna, P. Lorenzo, M. Mucciarelli, A. Perrone, S. Piscitelli, and F. Sdao, 2000, Comparison of geological and geophysical prospecting techniques in the study of a landslide in southern Italy: *European Journal of Environmental and Engineering Geophysics*, **4**, 117–128.
- Godio, A., C. Strobbia, and G. D. Bacco, 2006, Geophysical characterization of a rockslide in an alpine region: *Engineering Geology*, **83**, 273–286.
- Günther, T., C. Rücker, and K. Spitzer, 2006, Three-dimensional modeling and inversion of dc resistivity data incorporating topography—II Inversion: *Geophysical Journal International*, **166**, 506–517.
- Hall, J. W., I. C. Meadowcroft, E. M. Lee, P. H. A. J. M. van Gelder, 2002, Stochastic simulation of episodic soft coastal cliff erosion: *Coastal Engineering*, **46**, 159–174.
- Hampton, M. A., G. B. Griggs, T. B. Edil, D. E. Guy, J. T. Kelly, P. D. Komar, D. M. Mickelson, and H. M. Shipman, 2004, Processes that govern the formation and evolution of coastal cliffs, *in* M. A. Hampton and G. B. Griggs, eds., *Formation, Evolution, and Stability of Coastal Cliffs-Status and Trends*, U.S. Department of the Interior: U.S. Geological Survey.
- Jongmans, D., and S. Garambois, 2007, Geophysical investigation of landslides: a review, *Bulletin of Geological Society of France*, **2**, 101–112.
- Hakim, J., 1995, *A History of US: War, Peace and all that Jazz 1918-1945*: Oxford University Press.
- Kaufmann, H. W., and J. E. Kaufmann, 2003, *Fortress Third Reich: German Fortifications and Defense Systems in World War II*: Da Capo Press.
- Keller, G. V., and F. C. Frischknecht, 1966, *Electrical Methods in Geophysical Prospecting*, Pergamon Press.
- Lake, S. D., and G. D. Karner, 1987, The structure and evolution of the Wessex Basin, southern England: an example of inversion tectonics: *Tectonophysics*, **137**, 347–378.
- Leucci, G., 2007, Geophysical investigations to study the physical–mechanical characteristics of the rock in a coastal environment: the Cliff of Roca (Lecce, Italy): *Journal of Geophysics and Engineering*, **4**, 462–475.

- Loke, M. H., and R. D. Barker, 1996a, Rapid least-squares inversion of apparent resistivity pseudosections by a quasi-Newton method: *Geophysical Prospecting*, **44**, 131–152.
- Loke, M. H., and R. D. Barker, 1996b, Practical techniques for 3D resistivity surveys and data inversion: *Geophysical Prospecting*, **44**, 499–523.
- Loke, M. H., 2004, Tutorial: 2-D and 3-D electric imaging surveys, <http://www.georentals.co.uk/Lokenote.pdf>, accessed 20 June 2008.
- Lucia, F. J., 1983, Petrophysical parameters estimated from visual descriptions of carbonate rocks: a field classification of carbonate pore space: *Journal of Petroleum Technology*, **9**, 629–637.
- Lucia, F. J., 1995, Rock-fabric/petrophysical classification of carbonate pore space for reservoir characterization: *American Association of Petroleum Geologists Bulletin*, **79**, 1275–1300.
- McCann, D. M., and A. Forster, 1990, Reconnaissance geophysical methods in landslide investigations: *Engineering Geology*, **29**, 59–78.
- Mauritsch, H. J., W. Seiberl, R. Arndt, A. Romer, K. Schneiderbauer, and G. P. Sendlhofer, 2000, Geophysical investigations of large landslides in the Carnic Region of southern Austria: *Engineering Geology*, **56**, 373–388.
- Meric, O., S. Garambois, D. Jongmans, M. Wathelet, J. L. Chatelain, and J. M. Vengeon, 2005, Application of geophysical methods for the investigation of the large gravitational mass movement of Séchilienne, France: *Canadian Geotechnical Journal*, **42**, 1105–1115.
- Mortimore, R. N. and A. Dupperet, A., 2004, Coastal Chalk Cliff Instability, *Geological Society Engineering Geology Special Publication*, v.20: Geological Society of London.
- Mortimore, R. N., J. Lawrence, D. Pope, A. Dupperet, and A. Genter, 2004, Coastal cliff geohazards in weak rock: the UK chalk cliffs of Sussex, *in* R.N. Mortimore and A. Dupperet, eds., *Coastal Chalk Cliff Instability*, *Geological Society Engineering Geology Special Publication*, v.20: Geological Society of London, 3–31.
- Neuman, S. P., 2005, Trends, prospects and challenges in quantifying flow and transport through fractured rocks: *Hydrogeology Journal*, **13**, 124–147.

- Park, S. K., and G. P. Van, 1991, Inversion of pole–pole data for 3–D resistivity structure beneath arrays of electrodes: *Geophysics*, **56**, 951–960.
- Perrone A., A. Iannuzzi, V. Lapenna, P. Lorenzo, S. Piscitelli, V. Rizzo, and F. Sdao, 2004, High–resolution electrical imaging of the Varco d’Izzo earthflow (southern Italy): *Journal of Applied Geophysics*, **56**, 17–29.
- Riout, M., O. Dugué, R. Jan du Chêne, C. Ponsot, G. Fily, J. M. Moron, and P. R. Vail, 1991, Outcrop sequence stratigraphy of the Anglo–Paris basin, middle to upper Jurassic (Normandy, Maine, Dorset): *Belletín des Center de Recherches exploration-Production Elf-Aquitaine*, **15**, 101–194.
- Ritzi, R. W. and R. H. Andsolek, 1992, Relation between anisotropic transmissivity and azimuthal resistivity surveys in shallow, fractured, carbonate flow systems: *Ground Water*, **30**, 774–780.
- Rücker, C., T. Günther, and K. Spitzer, 2006, Three–dimensional modelling and inversion of dc resistivity data incorporating topography–I. Modelling: *Geophysical Journal International*, **166**, 495–505.
- Savouret, E., 2007, *Geographique : approche et reflexions a partir de l’etude environnementale et societale des impacts littoraux induits du débarquement de Normandie du 6 juin 1944*: These Doctorale, Universite de Caen/Basse Normandie.
- Sen, P. N., W. E. Kenyon, H. Takezaki, and M. J. Petricola, 1997, Formation factor of carbonate rocks with microporosity: model calculations: *Journal of Petroleum Science and Engineering*, **17**, 345–352.
- Sharma, P. V., 1997, *Environmental and Engineering Geophysics*: Cambridge University Press.
- Shewchuk, J. R., 2002, Delaunay refinement algorithms for triangular mesh generation, *Computational Geometry: Theory and Applications*, **22**, 21–74.
- Singha, K., and S. M. Gorelick, 2005, Saline tracer visualized with three–dimensional electrical resistivity tomography: field–scale spatial moment analysis: *Water Resources Research*, **41**, W05023, doi:10.1029/2004WR003460,
- Skinner, D., and G. Heinson, 2004, A comparison of electrical and electromagnetic methods for the detection of hydraulic pathways in a fractured rock aquifer, Clare Valley, South Australia: *Hydrogeology Journal*, **12**, 576–590.

- Summers, B., 2006, Petrophysical investigation of porosity distribution in the Geneva dolomite member of the Grand Tower formation in Marion county, Illinois: Ph.D. dissertation, Northern Illinois University, DeKalb.
- Suzuki, K., and S. Higashi, 2001, Groundwater flow after heavy rain in landslide–slope area from 2D inversion of resistivity monitoring data: *Geophysics*, **66**, 733–743.
- Telford, W. M., L. P. Geldart, and R. E. Sheriff, 1990, *Applied Geophysics*: Cambridge University Press.
- Ward, S. H., 1990, Resistivity and induced polarization methods, *in* S. H. Ward, ed., *Geotechnical and Environmental Geophysics*, v. 1: SEG, 147–89.
- Warden, B., R. Burt, F. Arinto, A. Mixon, and J. Daulton, 2007, *Pointe du Hoc Stabilization Study: Historical Study Final Report*: Center for Heritage Conservation, Texas A&M University, College Station.
- Waxman, M. H. and L. J. M. Smits, 1968, Electrical conductivities in oil–bearing shaly sands: *Society of Petroleum Engineers Journal*, **8**, 107–122.
- Yang, X., 1999, *Stochastic inversion of 3D ERT data*, Ph.D. thesis: the University of Arizona, Tucson.
- Zonge, K., J. Wynn, and S. Urquhart, 2005, Resistivity, induced polarization and complex resistivity, *in* D.K. Butler, eds., *Near–surface Geophysics*: SEG , 265–300.

APPENDIX A

2-D INVERSION CONFIGURATION FILE AND PARAMETERS

2-D inversion configuration file

```

DATAFILE=OP1 .ohm
DIMENSION=2
TOPOGRAPHY=1
SURFACESMOOTH=1
PRIMDX=0 .01
PARADX=0 .1
PARA2DQUALITY=33 .3
PRIM2DQUALITY=33 .4
ROBUSTDATA=1
LAMBDA=50
INPUTERRLEVEL=5
LOWERBOUND=2
UPPERBOUND=300

```

Description of Inversion Parameters

Available on <http://resistivity.net>

```

#
# Global settings
#
DATAFILE=projectfile # defines the project filename (required)
DIMENSION=3 # defines the dimension of the problem (2 for 2d or 3 for 3d)
TOPOGRAPHY=0 # defines if topography is present (0 or 1)
TOPOPOINTS= # defines file which has additional coordinates for topography (x y z)
TOPOPOLY= # defines file which has additional polygons for topography (x0 y0 z0)
TIMESTEPS= # defines file which has the names of additional datafiles used in timestep
inversion
PARAGEOMETRY= # defines polygon file for parametric geometry with extern script
or program
REFRAKTOR= # defines file with information about refractor
CYLINDER=0 # defines cylindric geometry (0 or 1)
ELECTRODNODES=1 # defines that electrodes are represented as nodes
SPACECONFIG=0 # defines geometric factor (0 for half space, 1 for full space, 2 for
mirrored half space)
UNDERWATER=0 # defines underwater survey, sets SPACECONFIG=2

```

```

#
# Data settings
#
INPUTOHM=0 # input data is in Ohm
OVERRIDEERROR=0 # overrides given errors with INPUTERRLEVEL and
INPUTERRVOLTAGE (0 or 1)
INPUTERRLEVEL=3 # sets input error level (in percent) if no error given
INPUTERRVOLTAGE=100e-6 # sets input voltage error (V) if no error given
FILTERVALS=0 # defines filter values (experimental)

#
# Inversion settings
#
RHOSTART=0 # resistivity of start model (0 = median of the data)
# can also be model specification file
MAXITER=20 # maximum number of iteration steps
SINGVALUE=-1 # potential value at electrodes, for sensitivity (internal)
LAMBDA=20 # regularization parameter
LAMBDAOPT=0 # optimize lambda by using l-curve (0 or 1)
LAMBDADECREASE=1 # decrease lambda with each iteration
CONSTRAINT=1 # order 0, 1, 2 (experimental)
ZPOWER=0 # weight for vertical gradients
BLOCKYMODEL=0 # iteratively reweighted model (L1)
ROBUSTDATA=0 # iteratively reweighted data (L1)
LOWERBOUND=0.0 # lower resistivity bound (logarithmic barrier)
UPPERBOUND=0.0 # upper resistivity bound (0.0 = deactivated)
SENSMATUPDATE=0 # update sensitivity matrix with each iteration step (internal)
SENSMATDROPTOL=0 # only for very large problems (internal)
SENSMATMAXMEM=800 # only for very large problems (internal)

#
# Mesh settings
#
PARAMAXCELLSIZE=0 # maximum cell size volume (m3) (DIMENSION=3); area
(m2) (DIMENSION=2) for para mesh
PRIMMAXCELLSIZE=0 # maximum cell size volume (m3) (DIMENSION=3); area
(m2) (DIMENSION=2) for prim mesh
PARADEPTH=0 # maximum depth of parameter domain in meter (0 = automatic)
PARABOUNDARY=5 # boundary around electrodes in parameter domain (percent)
SPLINEBOUNDARY=0 # spline circle boundary instead of piecewise linear
interpolation (experimental)
EQUIDISTBOUNDARY=0 # equidistant refined space between electrodes
BOUNDARY=500 # size of boundary area around parameter domain
MESHGEN=tetgen # 3d mesh generator

```

```

TETGENTOLERANCE=1e-12 # tetgen tolerance limit
TETGENPRESERVEBOUNDARY=0 # tetgen should suppress splitting of boundary
facets or segments
PARADX=0.0 # refinement for para grid (values 0.5 will be forced to 0.5)
PRIMDX=0.1 # refinement for prim grid (for 2d relative electrode spacing)
PARA2DQUALITY=33.0 # parameter grid (from 20 (bad) to 33.4 (good))
PRIM2DQUALITY=33.4 # primary grid (from 20 (bad) to 33.4 (good))
PARA3DQUALITY=1.5 # parameter grid (from 1.1 (good) to 2 (bad))
PRIM3DQUALITY=1.2 # primary grid (from 1.1 (good) to 2 (bad))
SURFACEQUALITY=30 # quality of topographical surface grid (from 20 (bad) to 33.4
(good))
SURFACEMAXTRISIZE=0.0 # maximal triangle area of parametric surface grid
SURFACESMOOTH=0 # improve quality of topographical surface grid
ICDROPTOL=0.0 # if number of nodes 200k drop tolerance is set for ICCG solver
LINSOLVER=1 # sets linear solver, 0 for homebrew PCG (very slow), 1 for TAUCS
(direct, ICCG), 2 for LDL (direct with AMD)
SECMESHREFINE=1 # use with caution (experimental)
SECP2MESH=0 # quadratic shapefunction for secmesh (experimental)
PRIMP2MESH=0 # use primary p2 mesh (experimental)

#
# Directory settings
#
MESHBASENAME=mesh # basename for mesh files
DIRMESHS=mesh # directory name for mesh files
DIRPOT=primaryPot # directory name for primary and interpolated potentials
DIRPRIMPOT=potentials # subdirectory name for primary potentials
DIRINTERPOLPOT=interpolated # subdirectory name for interpolated potentials
DIRFEM=femM # directory name for finite element solutions
DIRSENS=sensM # directory name for sensitivity matrix
OLDPRIMMESHSTYLE=0 # for internal use only

```

APPENDIX B**3-D INVERSION CONFIGURATION FILE**2006 inv.cfg file

```
DATAFILE=pdh_laser.ohm
DIMENSION=3
TOPOGRAPHY=1
TOPOPOLY=polypoint_new.txt
TOPOPOINTS=pdh_topopoint.xyz
PARA3DQUALITY=1.3
SURFACEQUALITY=30
PARABOUNDARY=20
SENSMATMAXMEM=10000
SENSMATDROPTOL=1e-5
LOWERBOUND=1
UPPERBOUND=500
PARADEPTH=50
LAMBDA=50
CONSTRAINT=6
LINSOLVER=2
ROBUSTDATA=1
OLDPRIMMESHSTYLE=1
SURFACESMOOTH=1
PRIMDX=0.2
PRIM2MESH=1
PRIM3DQUALITY=1.4
```

2008 OP inv.cfg file

```
DATAFILE=pdh08-3d-0c.ohm
DIMENSION=3
TOPOGRAPHY=1
TOPOPOLY=polybeach.txt
TOPOPOINTS=topopoint_new_a.txt
PARA3DQUALITY=1.3
SURFACEQUALITY=30
PARABOUNDARY=20
SENSMATMAXMEM=10000
SENSMATDROPTOL=1e-5
LOWERBOUND=1
UPPERBOUND=300
LAMBDA=50
LINSOLVER=2
CONSTRAINT=6
PARADEPTH=50
ROBUSTDATA=1
```

```
OLDPRIMMESHSTYLE=1  
SURFACESMOOTH=1  
PRIMDX=0.2  
PRIMP2MESH=1  
PRIM3DQUALITY=1.4
```

2008 RCP inv.cfg file

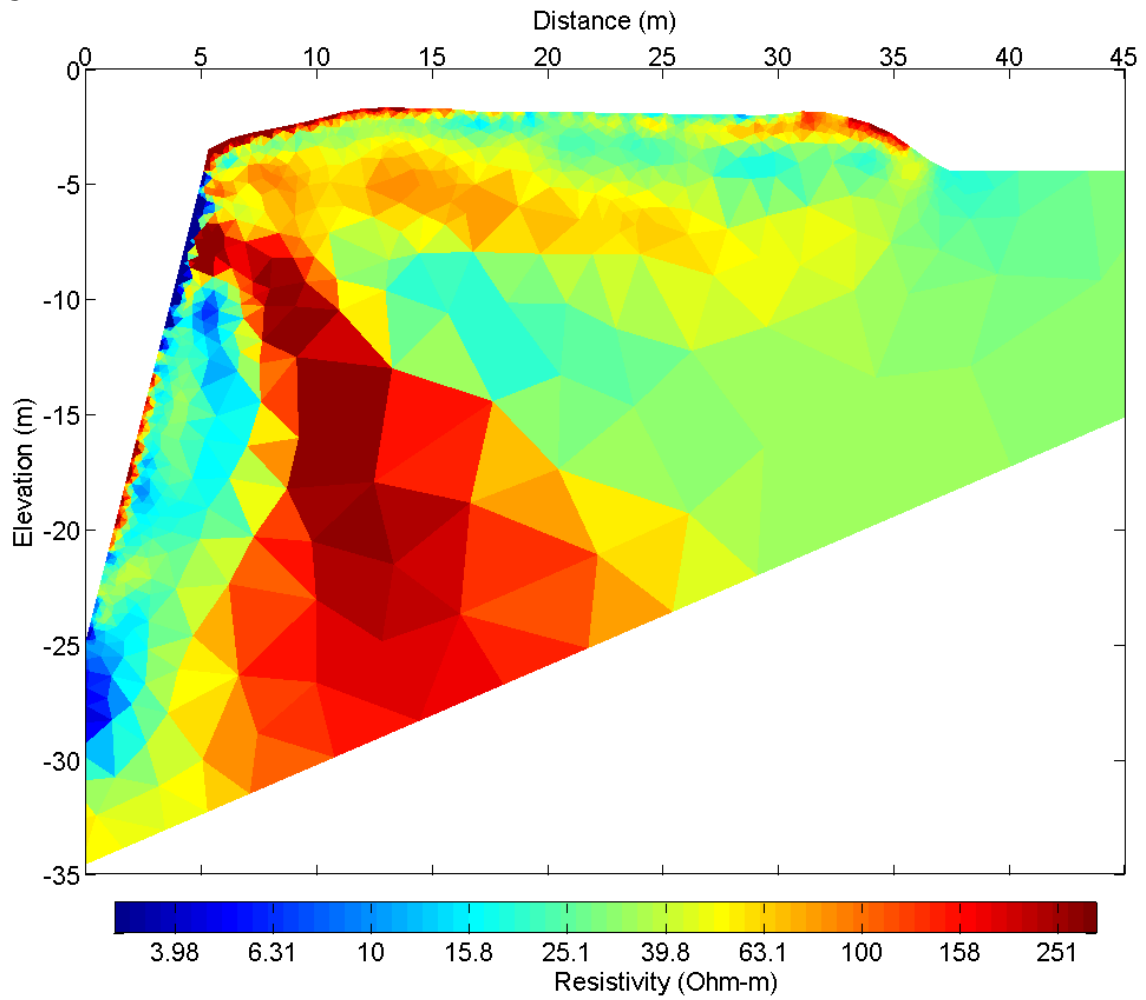
```
DATAFILE=rcp_0_new.ohm  
DIMENSION=3  
TOPOGRAPHY=1  
TOPOPOINTS=rcp-topopoint3.xyz  
PARA3DQUALITY=1.3  
SURFACEQUALITY=30  
PARABOUNDARY=20  
SENSMATMAXMEM=10000  
SENSMATDROPTOL=1e-5  
LOWERBOUND=1  
UPPERBOUND=300  
LAMBDA=50  
LINSOLVER=2  
CONSTRAINT=6  
PARADEPTH=50  
ROBUSTDATA=1  
OLDPRIMMESHSTYLE=1  
SURFACESMOOTH=1  
PRIMDX=0.2  
PRIMP2MESH=1  
PRIM3DQUALITY=1.4
```

Note that Description of Inversion Parameters can be found in APPENDIX A

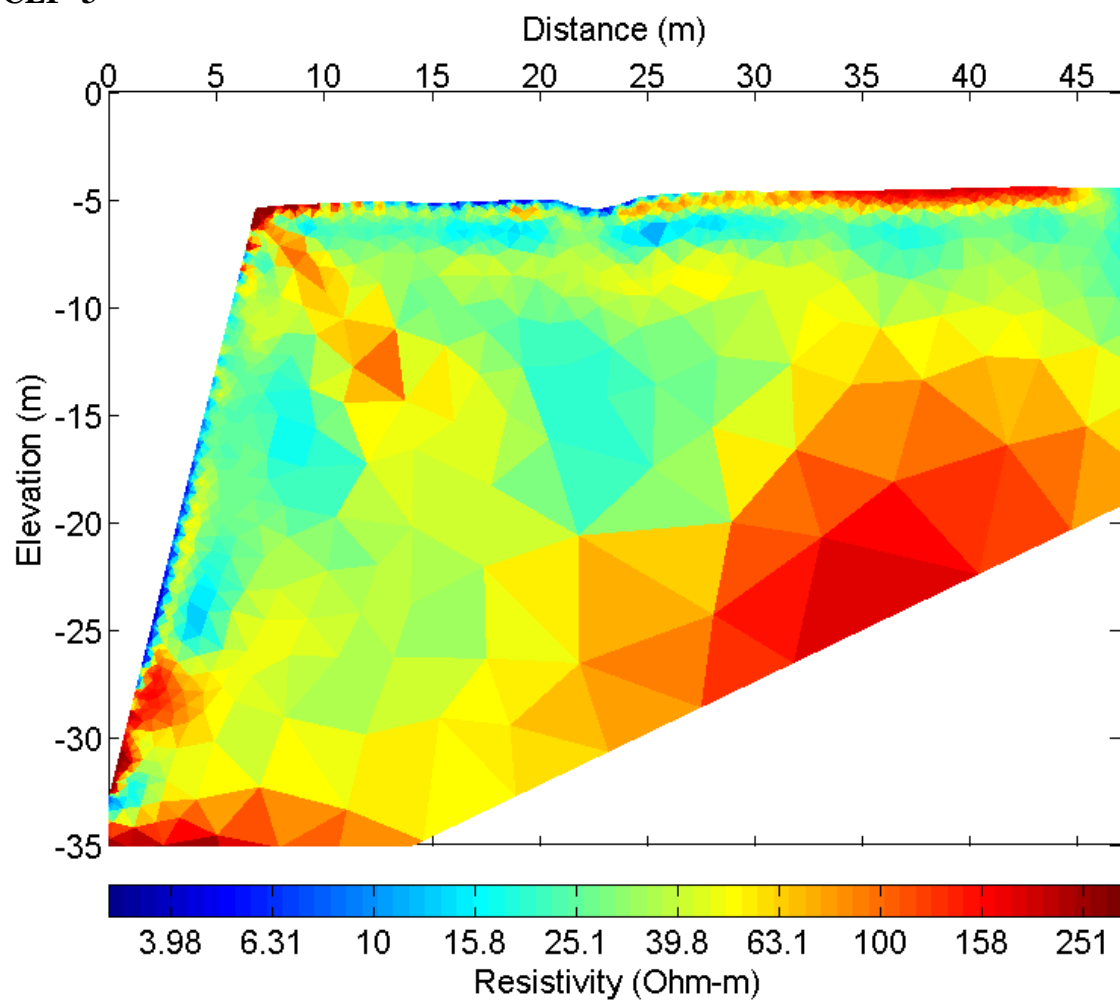
APPENDIX C

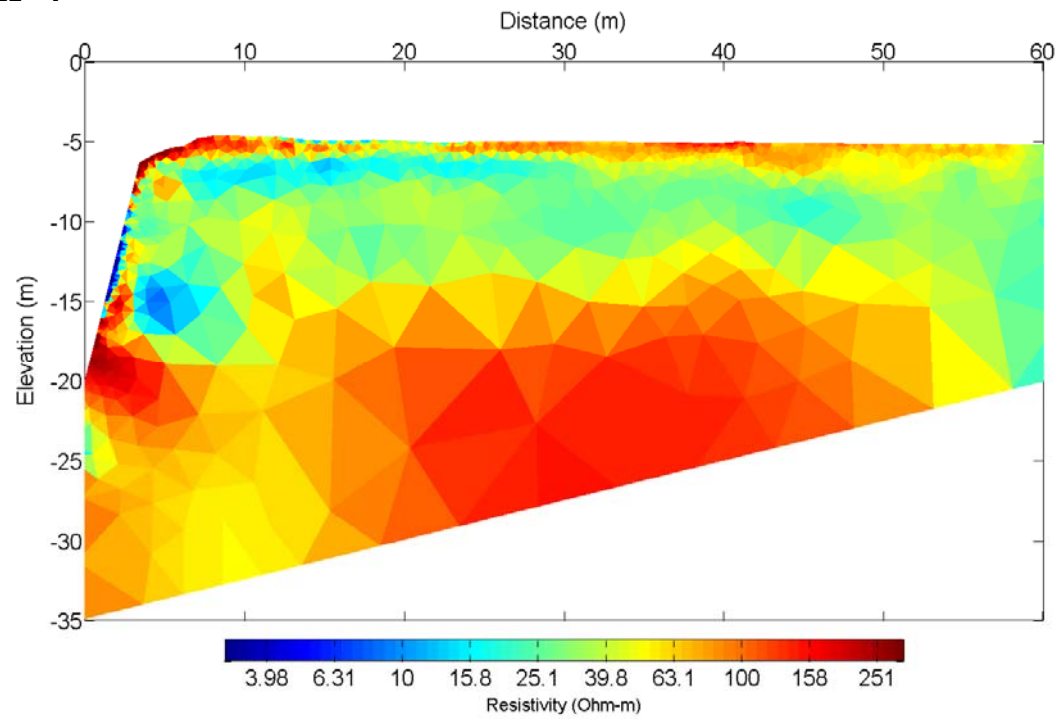
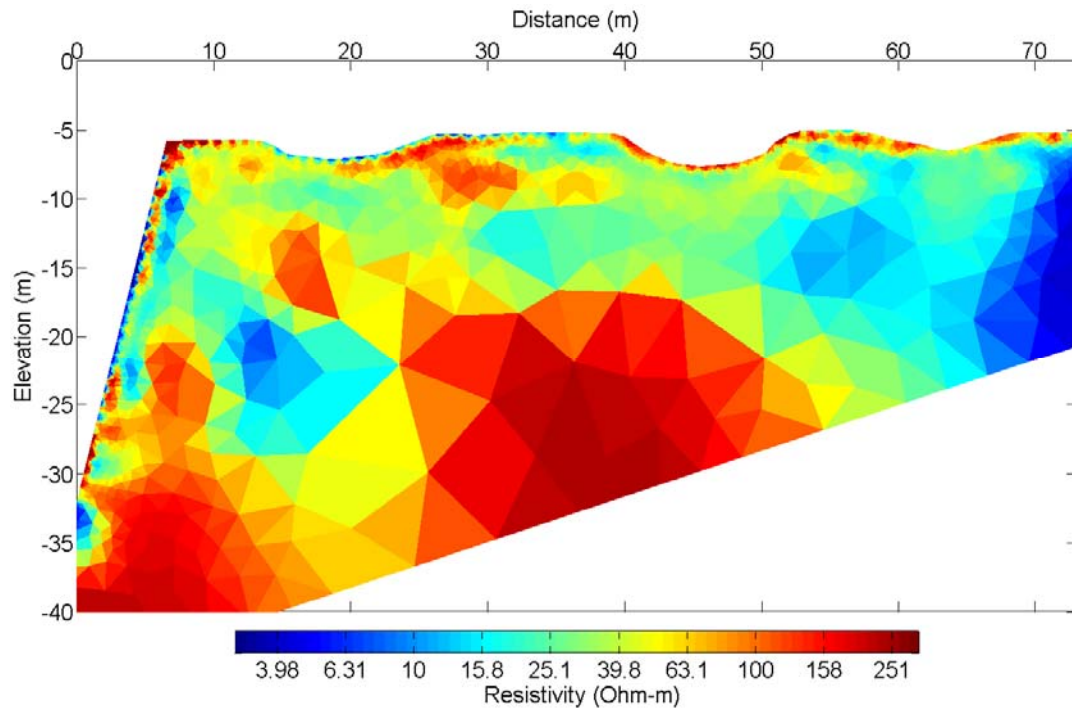
2006 2-D INVERSION TOMOGRAMS

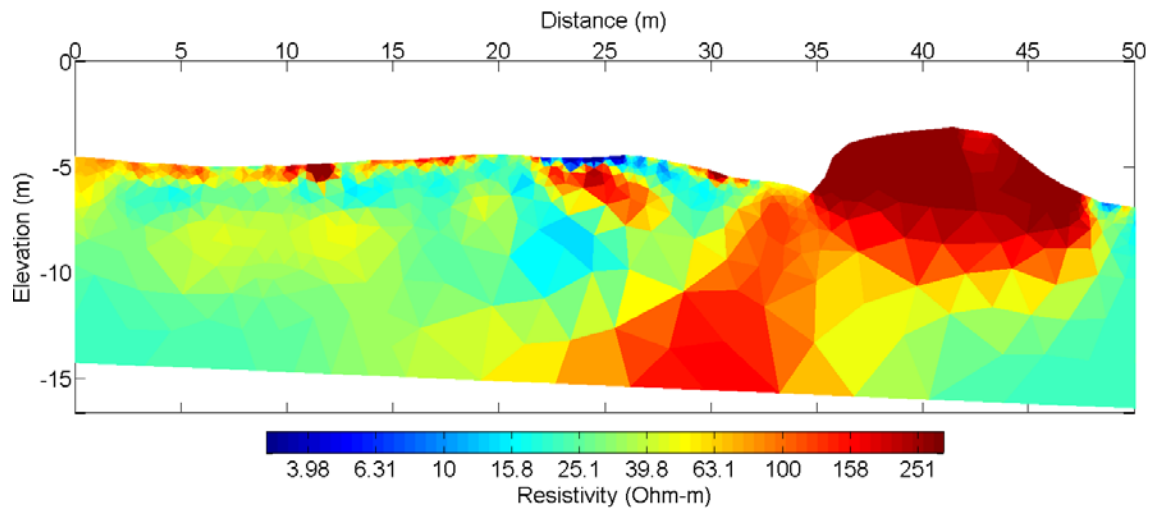
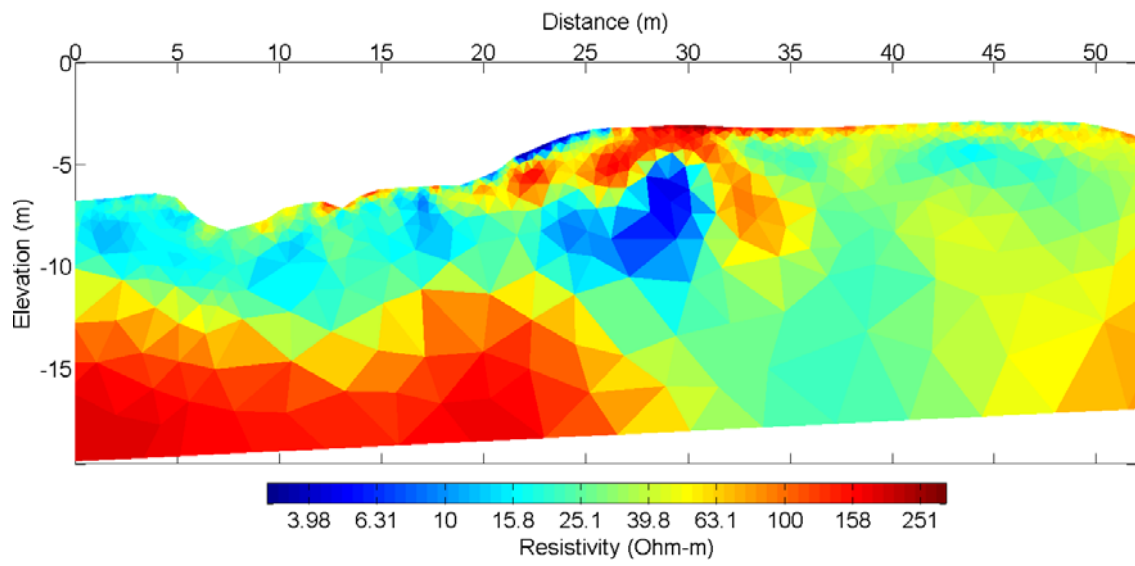
CLF-2

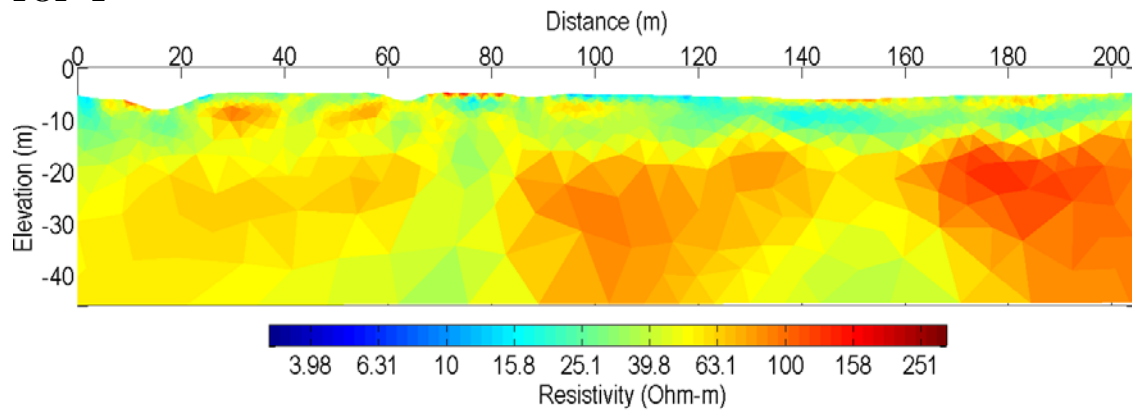
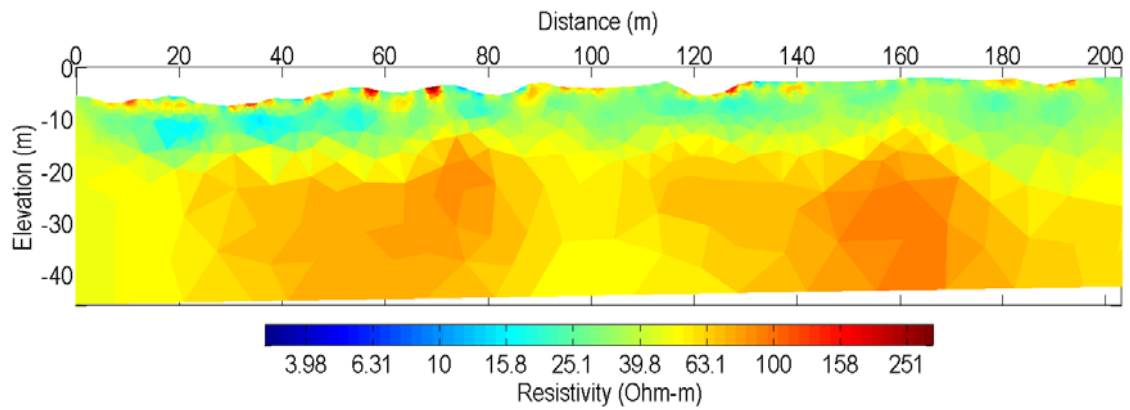
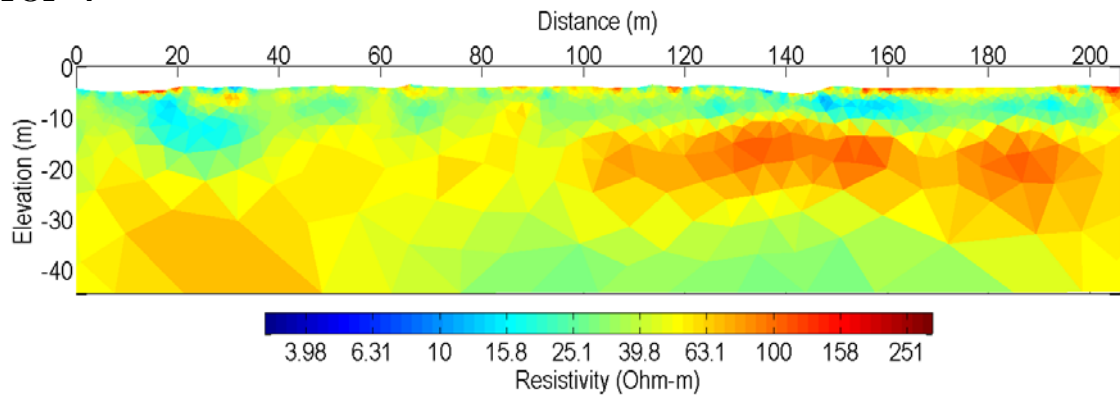


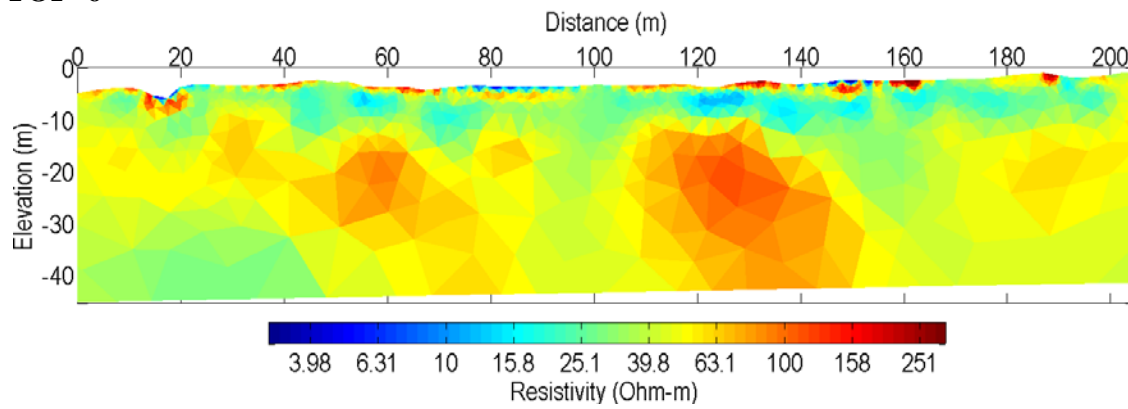
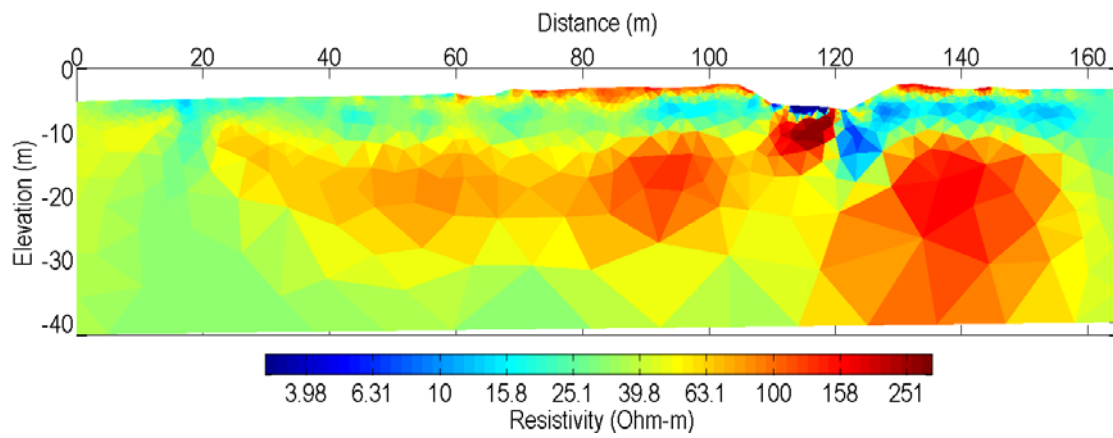
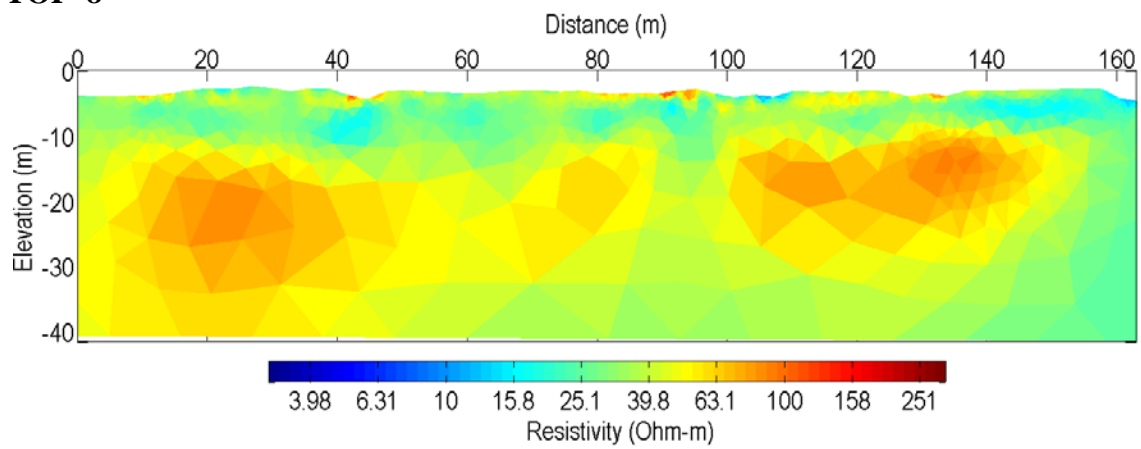
CLF-3

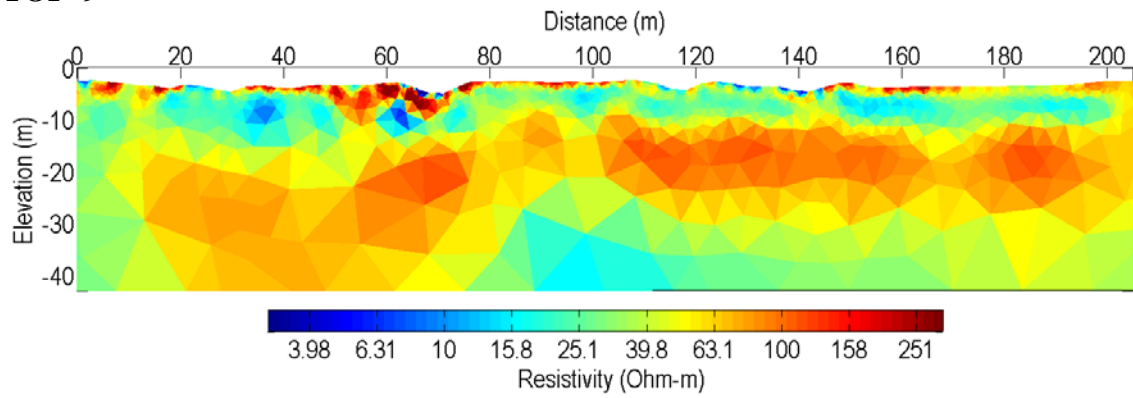
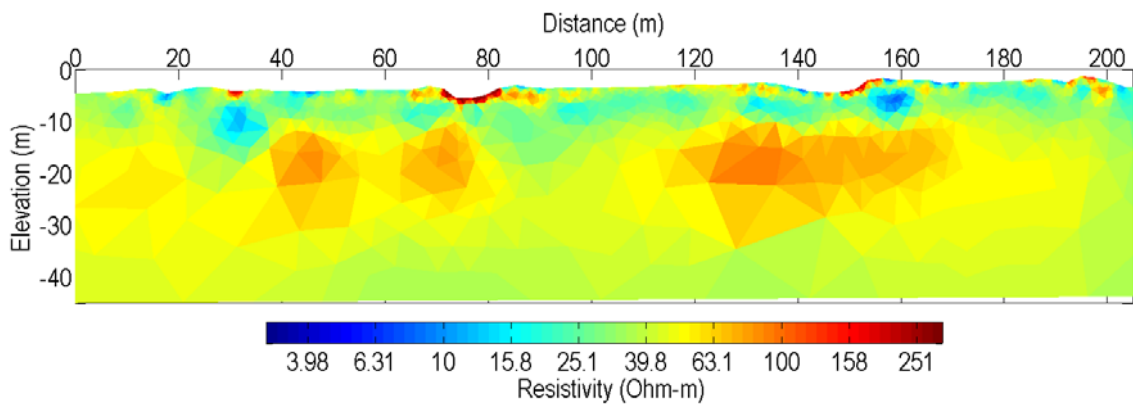


CLF-4**CLF-6**

OBS-1**OBS-2**

TOP-1**TOP-3****TOP-4**

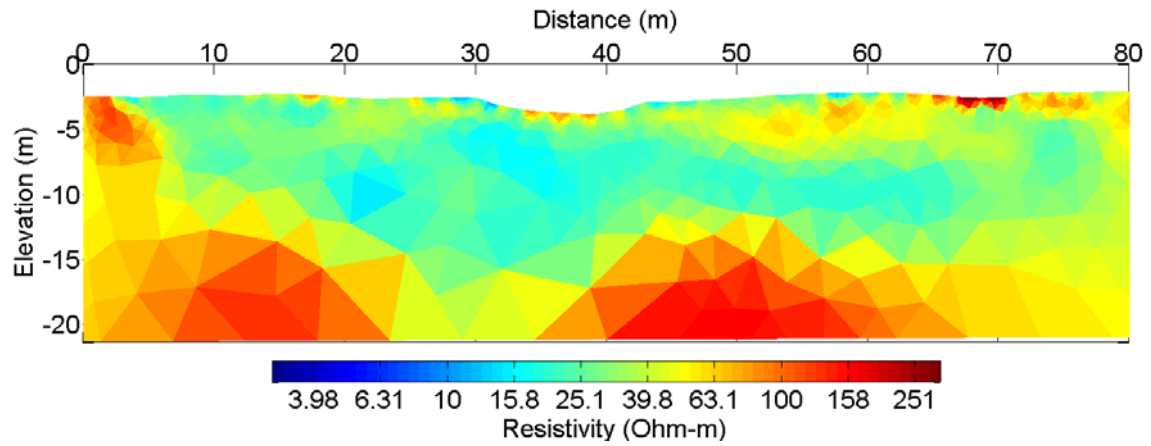
TOP-6**TOP-7****TOP-8**

TOP-9**TOP-10**

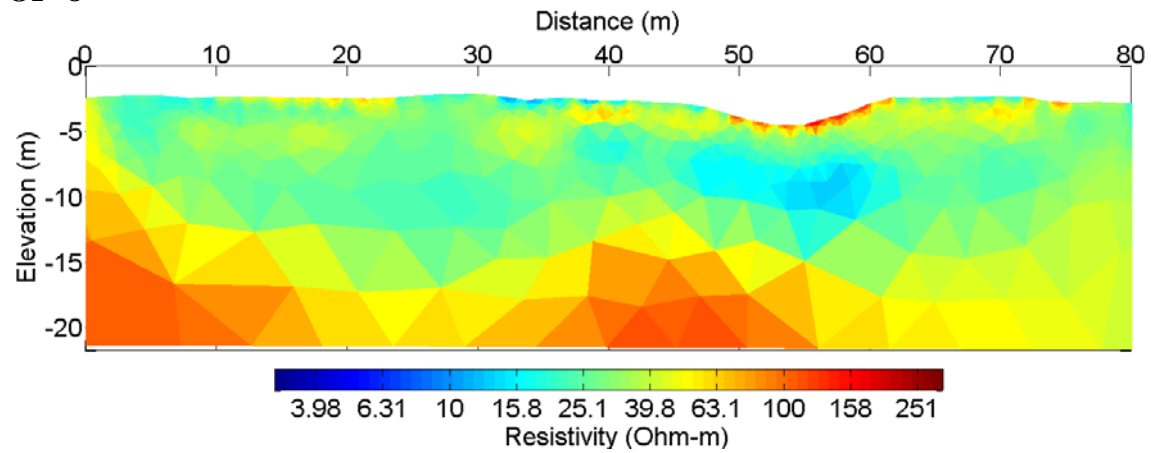
APPENDIX D

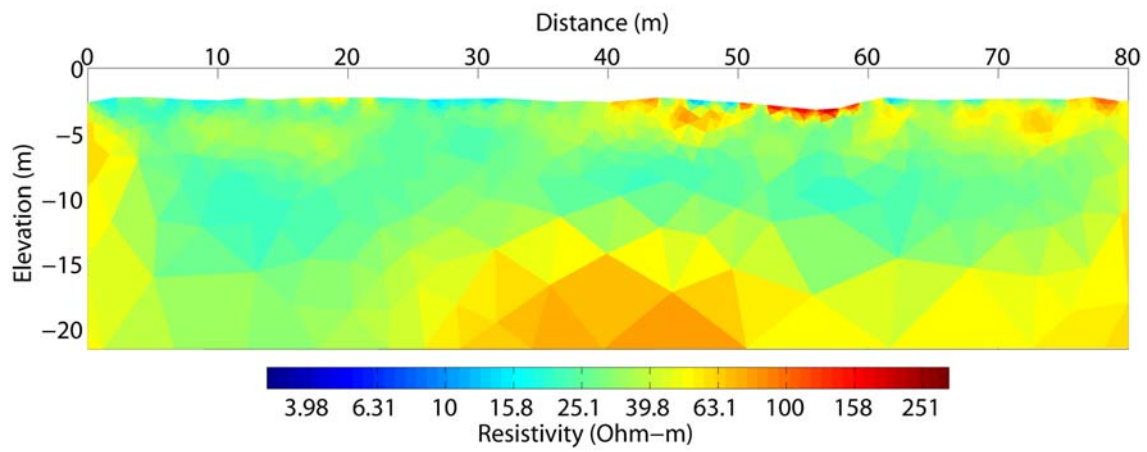
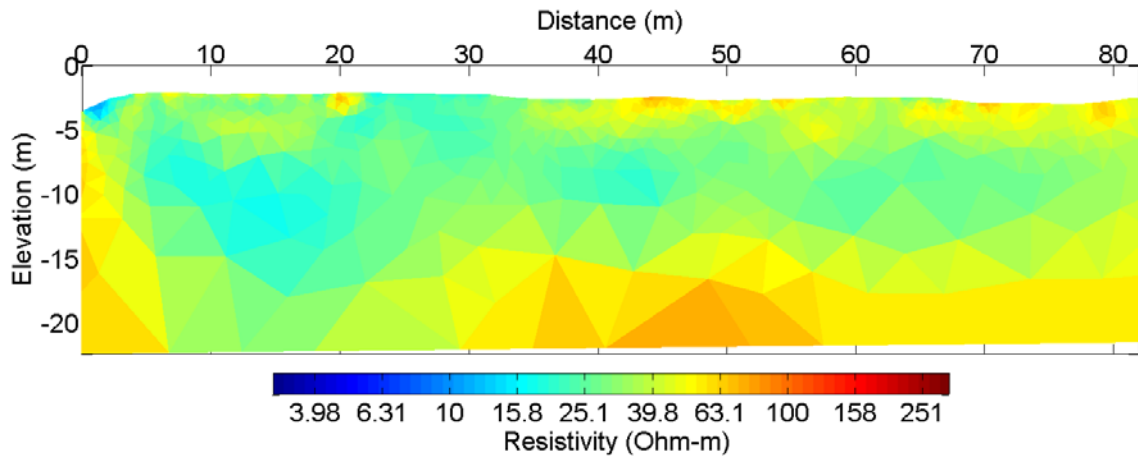
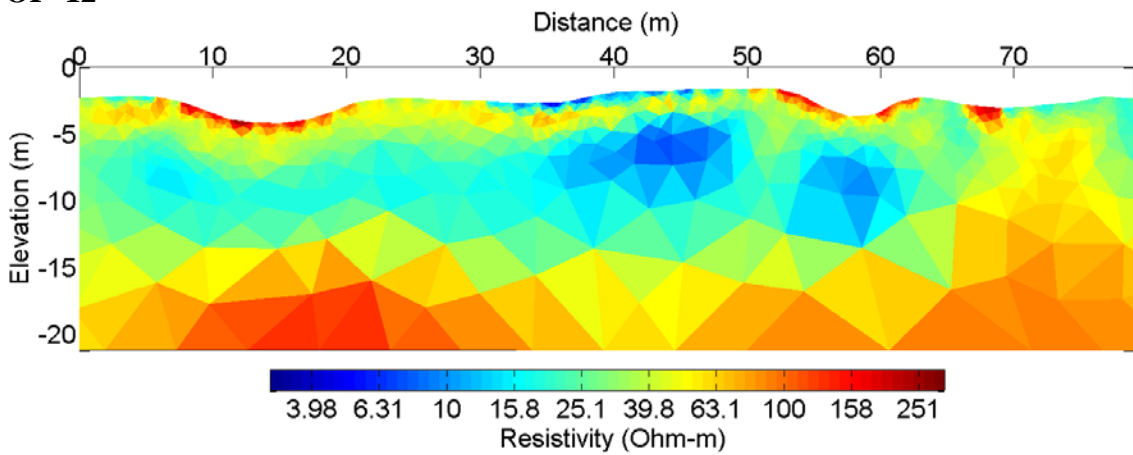
2008 OP AND RCP 2-D INVERSION TOMOGRAMS

OP-6

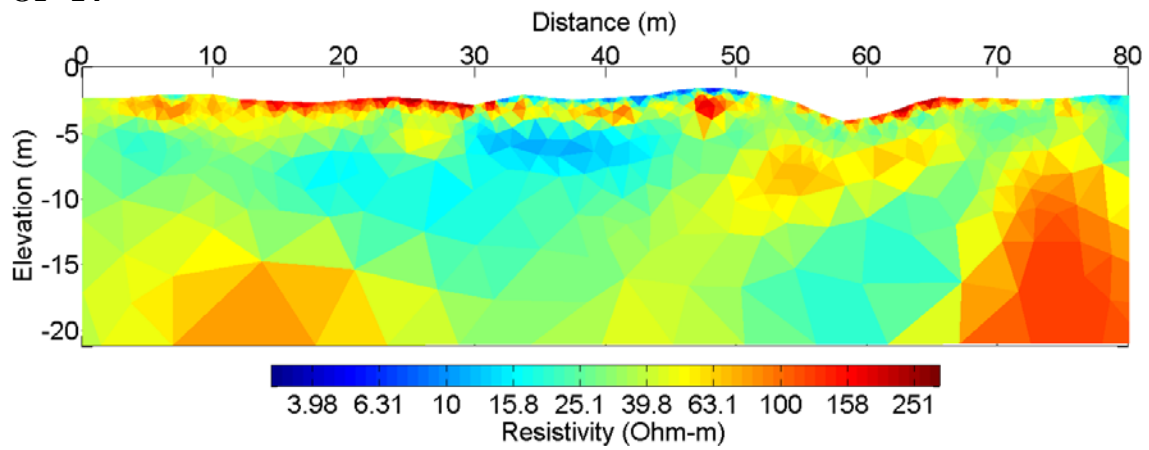


OP-8

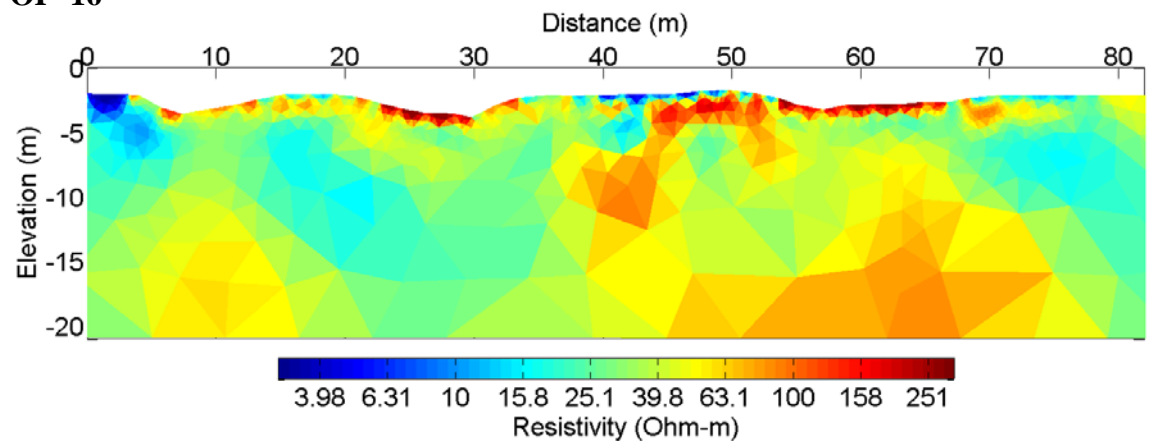


OP-9**OP-10****OP-12**

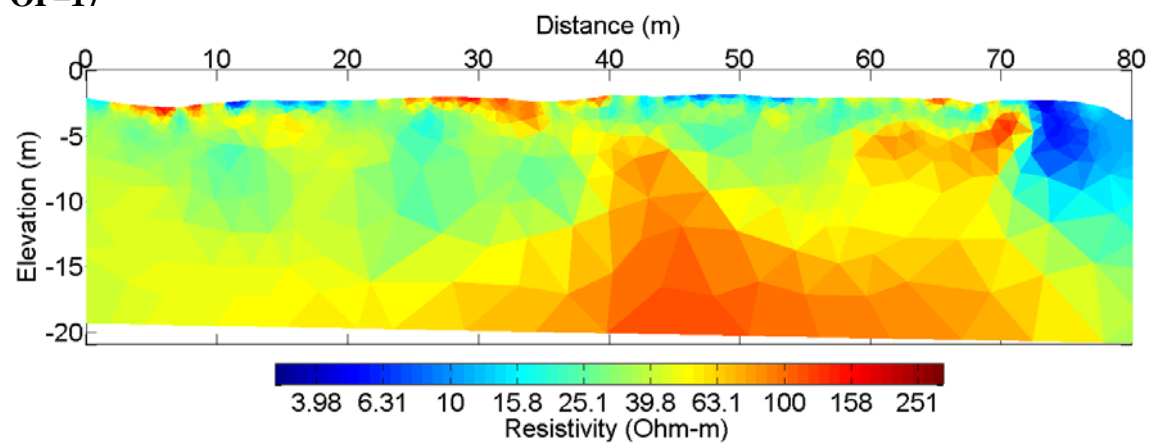
OP-14

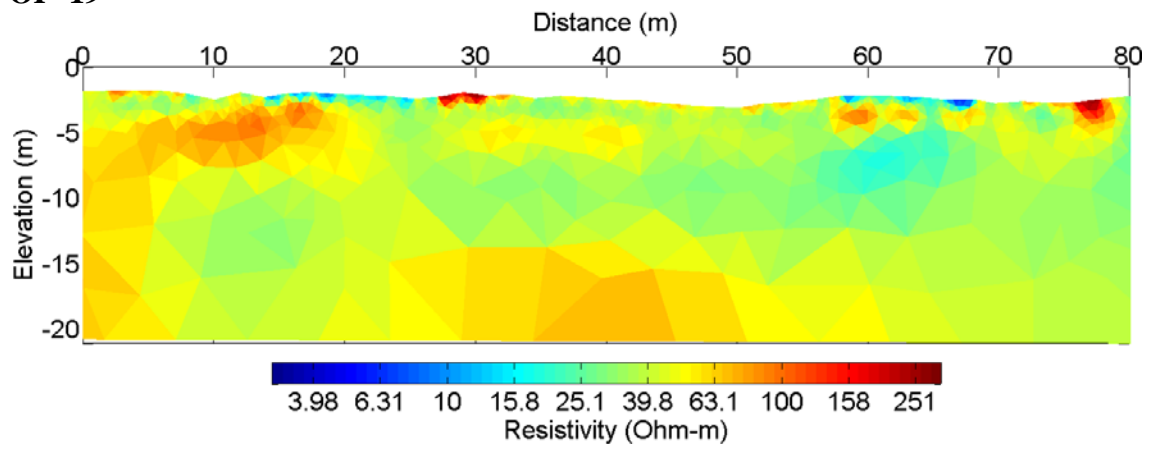
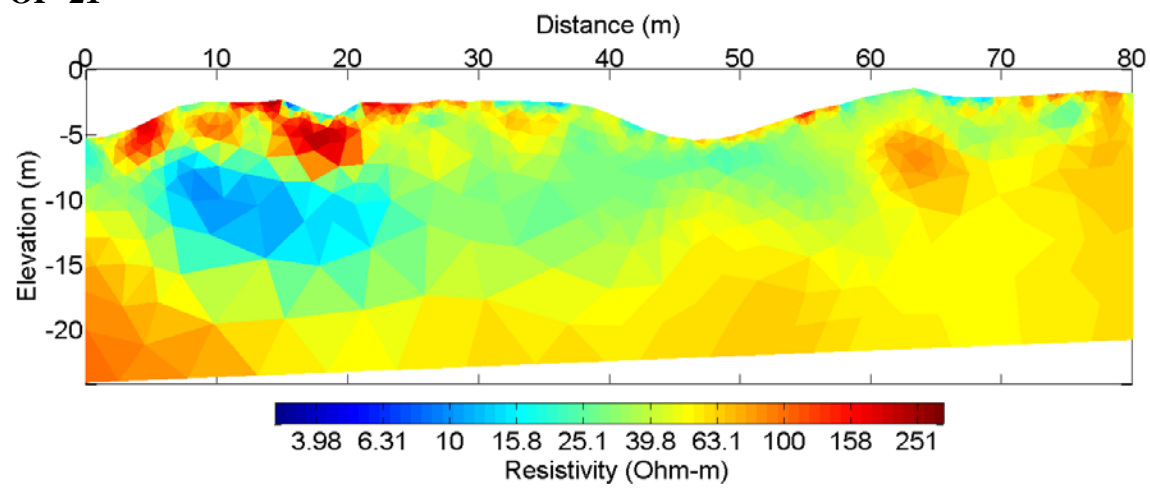
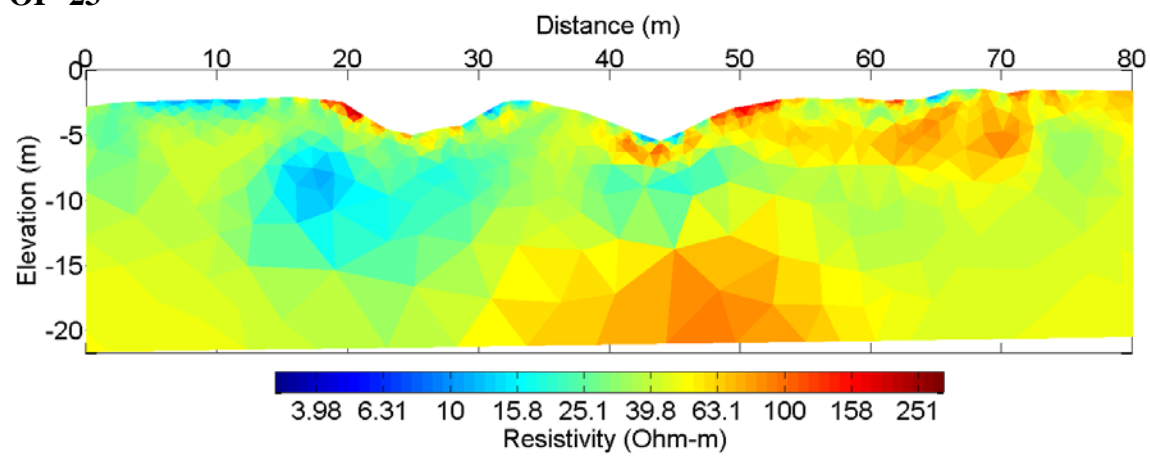


OP-16

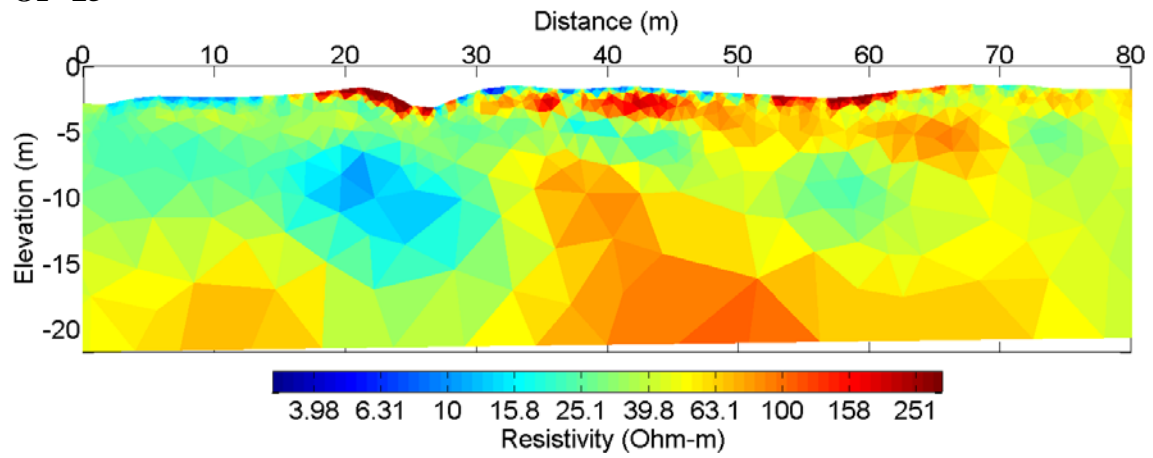


OP-17

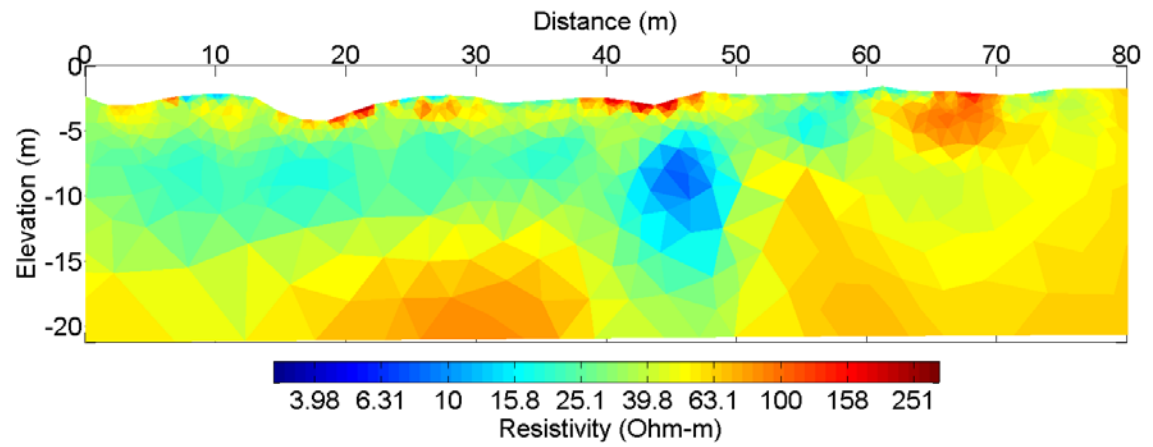


OP-19**OP-21****OP-23**

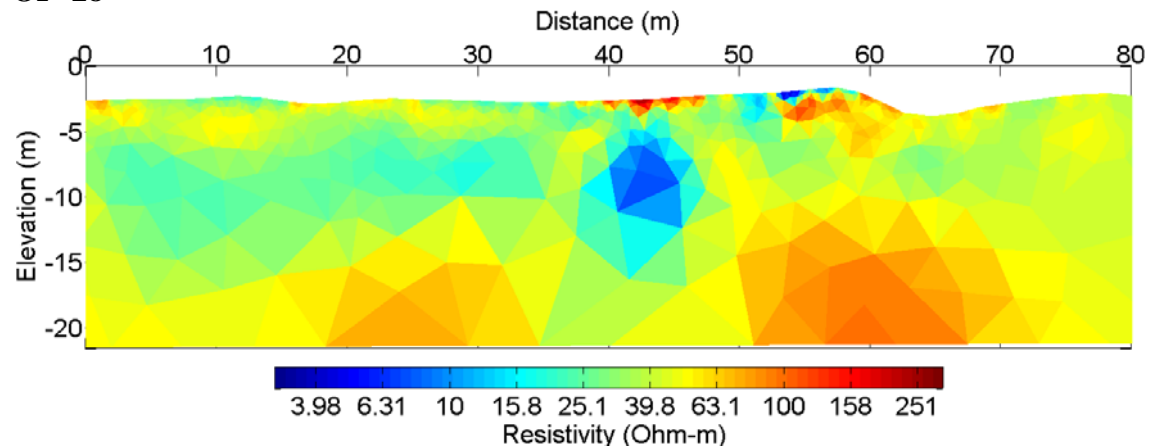
OP-25



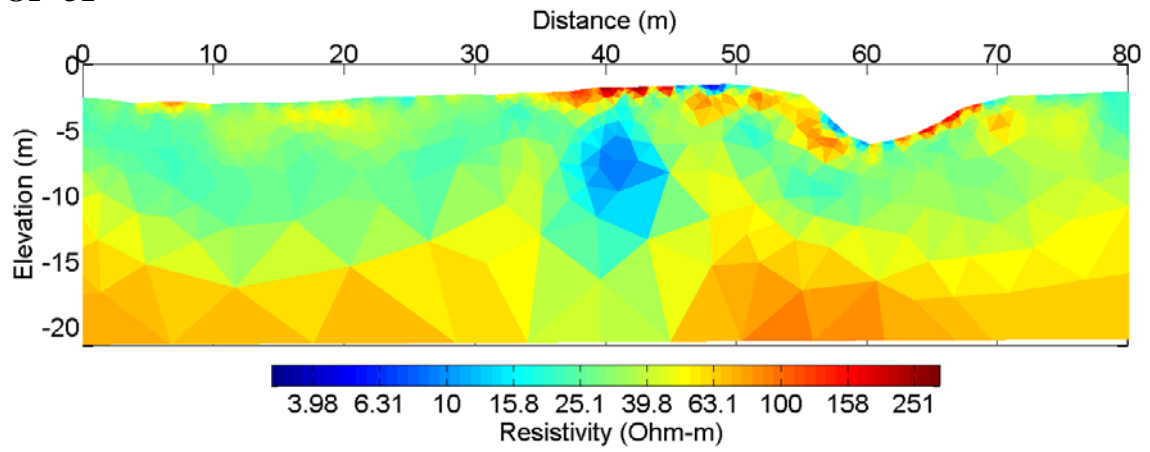
OP-27



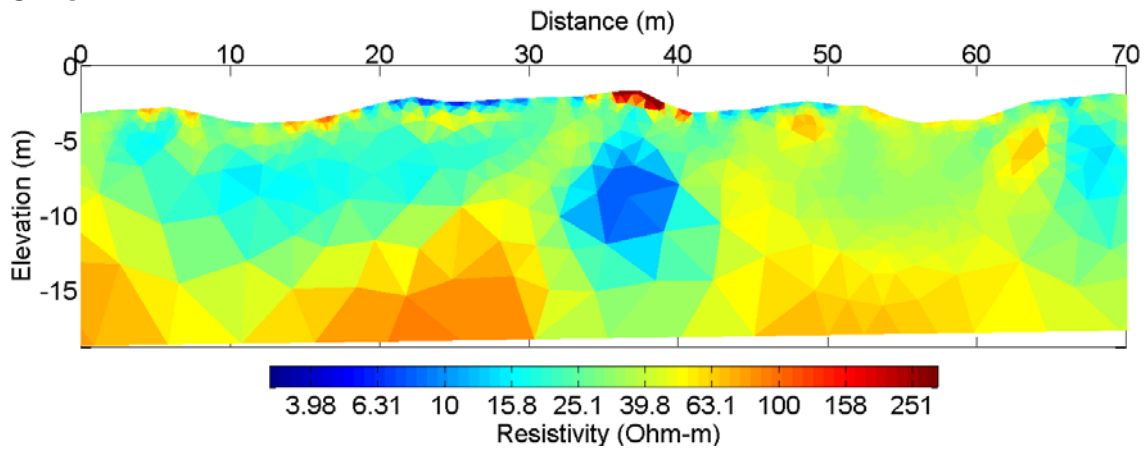
OP-28



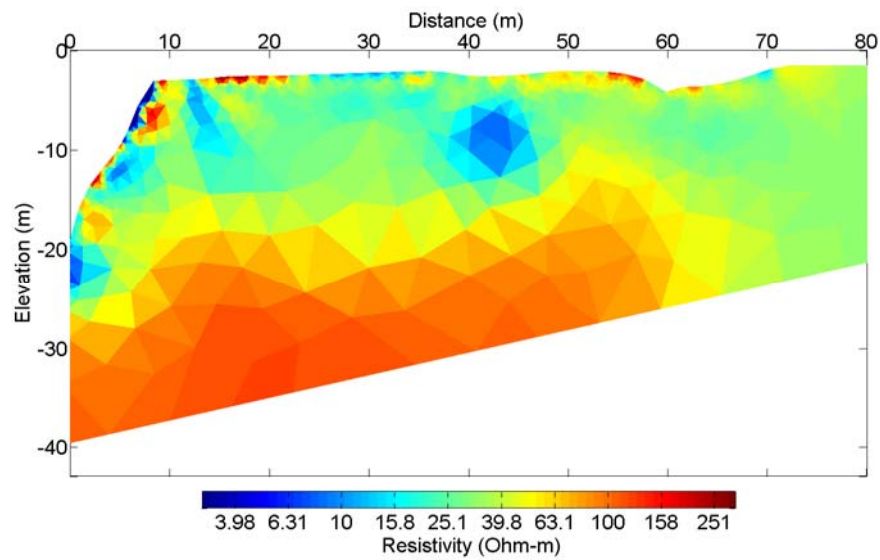
OP-31

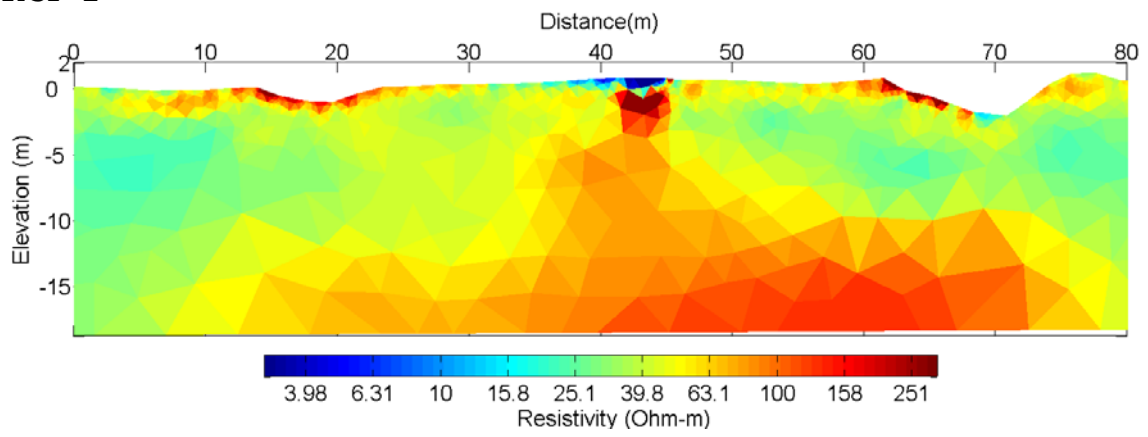
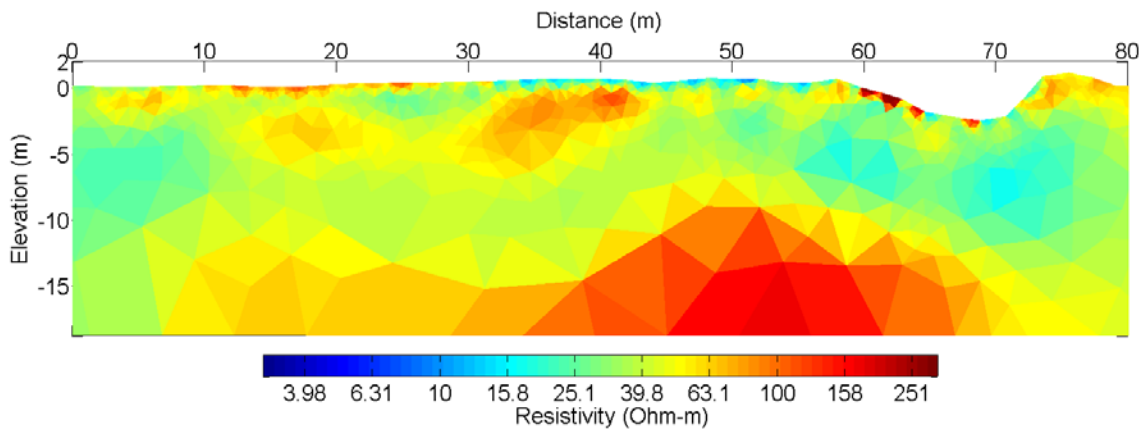


OP-32



OP-40



RCP-2**RCP-4**

VITA

Name: Suwimon Udphuay

Address: Department of Geological Sciences, Faculty of Science, Chiang Mai University, Chiang Mai, 50200, Thailand

Email Address: suwimons@hotmail.com

Education: B.S., Physics, Chiang Mai University, 1997
M.S., Applied Geophysics, Chiang Mai University, 2001
M.S., Geophysics, Boise State University, 2004
Ph.D., Geophysics, Texas A&M University, 2008